Publication Year	2023
Acceptance in OA	2025-02-19T15:56:28Z
Title	Hubble Space Telescope survey of Magellanic Cloud star clusters. Photometry and astrometry of 113 clusters and early results
Authors	Milone, A. P., Cordoni, G., MARINO, Anna, D'Antona, F., Bellini, A., DI CRISCIENZO, Marcella, Dondoglio, E., Lagioia, E. P., Langer, N., Legnardi, M. V., Libralato, M., Baumgardt, H., Bettinelli, M., Cavecchi, Y., de Grijs, R., Deng, L., Hastings, B., Li, C., Mohandasan, A., Renzini, A., Vesperini, E., Wang, C., Ziliotto, T., DI CARLO, Matteo, Costa, G., DELL'AGLI, Flavia, Di Stefano, S., Jang, S., Martorano, M., SIMIONI, Matteo, Tailo, M., VENTURA, Paolo
Publisher's version (DOI)	10.1051/0004-6361/202244798
Handle	http://hdl.handle.net/20.500.12386/36077
Journal	ASTRONOMY & ASTROPHYSICS
Volume	672

A&A 672, A161 (2023)
https://doi.org/10.1051/0004-6361/202244798
© The Authors 2023

Astronomy & Astrophysics

Hubble Space Telescope survey of Magellanic Cloud star clusters

Photometry and astrometry of 113 clusters and early results*

A. P. Milone[1,2], G. Cordoni[1], A. F. Marino[2,3], F. D'Antona[4], A. Bellini[5], M. Di Criscienzo[4], E. Dondoglio[1], E. P. Lagioia[1], N. Langer[6,7], M. V. Legnardi[1], M. Libralato[5], H. Baumgardt[8], M. Bettinelli[1], Y. Cavecchi[9,10], R. de Grijs[11,12], L. Deng[13], B. Hastings[6,7], C. Li[14], A. Mohandasan[1], A. Renzini[2], E. Vesperini[15], C. Wang[6,7], T. Ziliotto[1], M. Carlos[1], G. Costa[1], F. Dell'Agli[4], S. Di Stefano[1], S. Jang[1], M. Martorano[1], M. Simioni[2], M. Tailo[16], and P. Ventura[4]

[1] Dipartimento di Fisica e Astronomia "Galileo Galilei", Univ. di Padova, Vicolo dell'Osservatorio 3, Padova 35122, Italy
e-mail: `antonino.milone@unipd.it`
[2] Istituto Nazionale di Astrofisica – Osservatorio Astronomico di Padova, Vicolo dell'Osservatorio 5, Padova 35122, Italy
[3] Istituto Nazionale di Astrofisica – Osservatorio Astrofisico di Arcetri, Largo Enrico Fermi, 5, Firenze 50125, Italy
[4] INAF – Osservatorio Astronomico di Roma, Via Frascati 33, 00040 Monte Porzio Catone, Roma, Italy
[5] Space Telescope Science Institute, 3800 San Martin Drive, Baltimore, MD 21218, USA
[6] Argelander-Institut für Astronomie, Universität Bonn, Auf dem Hügel 71, 53121 Bonn, Germany
[7] Max-Planck-Institut für Radioastronomie, Auf dem Hügel 69, 53121 Bonn, Germany
[8] School of Mathematics and Physics, The University of Queensland, St. Lucia, QLD 4072, Australia
[9] Instituto de Astronomia, Universidad Nacional Autonoma de Mexico, Circuito exterior, Ciudad de Mexico 04510, Mexico
[10] Departament de Fisica, EEBE, Universitat Politecnica de Catalunya, Av. Eduard Maristany 16, 08019 Barcelona, Spain
[11] School of Mathematical and Physical Sciences, Macquarie University, Balaclava Road, Sydney, NSW 2109, Australia
[12] Research Centre for Astronomy, Astrophysics and Astrophotonics, Macquarie University, Balaclava Road, Sydney, NSW 2109, Australia
[13] Department of Astronomy, China West Normal University, 1 ShiDa Road, 637002 Nanchong, PR China
[14] School of Physics and Astronomy, Sun Yat-sen University, Daxue Road, Zhuhai 519082, PR China
[15] Department of Astronomy, Indiana University, Bloomington, IN 47401, USA
[16] Dipartimento di Fisica e Astronomia Augusto Righi, Università degli Studi di Bologna, Via Gobetti 93/2, 40129 Bologna, Italy

Received 23 August 2022 / Accepted 13 December 2022

ABSTRACT

In the past few years, we have undertaken an extensive investigation of star clusters and their stellar populations in the Large and Small Magellanic Clouds (LMC and SMC) based on archival images collected with the *Hubble* Space Telescope. We present photometry and astrometry of stars in 101 fields observed with the Wide Field Channel of the Advanced Camera for Surveys and the Ultraviolet and Visual Channel and the Near-Infrared Channel of Wide Field Camera 3. These fields comprise 113 star clusters. We provide differential-reddening maps for those clusters with significant reddening variations across the field of view. We illustrate various scientific outcomes that arise from the early inspection of the photometric catalogs. In particular, we provide new insights into the extended main-sequence turnoff (eMSTO) phenomenon: (i) We detected eMSTOs in two clusters, KMHK 361 and NGC 265, which had no previous evidence of multiple populations. This finding corroborates the conclusion that the eMSTO is a widespread phenomenon among clusters younger than ∼2 Gyr. (ii) The homogeneous color-magnitude diagrams (CMDs) of 19 LMC clusters reveal that the distribution of stars along the eMSTO depends on cluster age. (iii) We discovered a new feature along the eMSTO of NGC 1783, which consists of a distinct group of stars on the red side of the eMSTO in CMDs composed of UV filters. Furthermore, we derived the proper motions of stars in the fields of view of clusters with multi-epoch images. Proper motions allowed us to separate the bulk of bright field stars from cluster members and investigate the internal kinematics of stellar populations in various LMC and SMC fields. As an example, we analyze the field around NGC 346 to disentangle the motions of its stellar populations, including NGC 364 and BS 90, young and pre-main-sequence stars in the star-forming region associated with NGC 346, and young and old field stellar populations of the SMC. Based on these results and the fields around five additional clusters, we find that young SMC stars exhibit elongated proper-motion distributions that point toward the LMC, thus providing new evidence for a kinematic connection between the LMC and SMC.

Key words. Magellanic Clouds – globular clusters: general – open clusters and associations: general – techniques: photometric – stars: kinematics and dynamics

---

[*] Data are only available at the CDS via anonymous ftp to `cdsarc.cds.unistra.fr` (`130.79.128.5`) or via `https://cdsarc.cds.unistra.fr/viz-bin/cat/J/A+A/672/A161`

1. Introduction

In the past few decades, our group has extensively used the *Hubble* Space Telescope (HST) archive to study star clusters in both Magellanic Clouds (e.g., Milone et al. 2009, 2020, and references therein). The exquisite stellar photometry and astrometry provided by HST, together with the most advanced techniques for the analysis of astronomical images (e.g., Anderson et al. 2008; Sabbi et al. 2016; Bellini et al. 2017), has provided significant advances in our understanding of Magellanic Cloud star clusters and their stellar populations.

Inspired by the discovery that the color-magnitude diagram (CMD) of the Large Magellanic Cloud (LMC) cluster NGC 1806 is not consistent with a single isochrone (Mackey & Broby 2007), we started a series of papers to investigate the so-called extended main-sequence turnoff (eMSTO) phenomenon in clusters with ages from about 1 to 2.3 Gyr. The main results include the discovery that the eMSTO is a common feature of Magellanic Cloud clusters (Milone et al. 2009), the early discoveries of a split main sequence (MS) in young Magellanic Cloud clusters (Milone et al. 2013, 2015, 2016, 2017), and the characterization of the multiple populations in young and intermediate-age LMC and Small Magellanic Cloud (SMC) clusters (Milone et al. 2018). We provided the first direct evidence, based on high-resolution spectra, that the blue and red MSs are made up of stellar populations with different rotation rates (Marino et al. 2018a) and that the color and magnitude of an eMSTO star depend on stellar rotation (Dupree et al. 2017; Marino et al. 2018a). The high-precision photometry resulting from this project has been instrumental in shedding light on the physical mechanisms that are responsible for generating multiple populations in young clusters and has been used both by our team and by other groups to constrain the effect of rotation and stellar mergers on the eMSTO and the split MS (e.g., Bastian & de Mink 2009; D'Antona et al. 2015, 2017; Wang et al. 2022; Cordoni et al. 2022) and the contribution of variable stars on the eMSTO (Salinas et al. 2018). Although our main purpose consisted in investigating the eMSTO phenomenon, the resulting photometric and astrometric catalogs have been used for various investigations of stellar astrophysics, including multiple stellar populations in Magellanic Cloud globular clusters (GCs; Lagioia et al. 2019a,b; Milone et al. 2020; Dondoglio et al. 2021), photometric binaries (Milone et al. 2009, 2013), Be stars (Milone et al. 2018; Hastings et al. 2021), and extinction (De Marchi et al. 2020).

Driven by these results, we decided to homogeneously analyze all archival images collected with the Ultraviolet and Visual Channel (UVIS) and the Near Infrared Channel (NIR) of Wide Field Camera 3 (WFC3) and with the Wide Field Channel of the Advanced Camera for Surveys (WFC/ACS) on board HST. In this work, we present high-precision stellar positions and magnitudes for stars in 101 fields of the Magellanic Clouds, including 113 star clusters.

The paper is organized as follows. Section 2 describes the data set and the methods used for homogeneously reducing the data and presents the CMDs. The methods for correcting the photometry for differential reddening and the differential-reddening maps are discussed in Sect. 3, while Sect. 4 is dedicated to the determination of the cluster centers. Absolute stellar proper motions are derived in Sect. 5. Section 6 provides some scientific cases that arose from the early inspection of our catalogs. Finally, we report in the appendix the serendipitous discovery of one gravitational lens and two stellar clusters.

2. Data and data analysis

The data set used in this paper comprises images collected through the UVIS/WFC3 and NIR/WFC3, and WFC/ACS on board HST. The images include 84 known star clusters in the LMC and 29 clusters in the SMC. These clusters span wide intervals of age and stellar density, from sparse star-forming regions to old and dense GCs. The main properties of the available exposures are listed in Table B.1.

Photometry and astrometry are obtained from calibrated, flat-fielded WFC3/NIR (_flt) exposures, while in the case of UVIS/WFC3 and WFC/ACS data we used the calibrated, flat-fielded exposures corrected for the effects of the poor charge-transfer efficiency (CTE) of the detectors (_flc, Anderson & Bedin 2010). Stars are measured by means of distinct approaches that work best in different brightness regimes, as discussed in the following subsections.

2.1. First-pass photometry

We accounted for spatial variations of the point-spread function (PSF) by using the grids of library PSFs provided by Jay Anderson for each filter and camera. The PSFs can change from one exposure to another due to focus variations produced by the breathing of HST, small guiding inaccuracies, and residual CTE. To derive the optimal PSF, we perturbed the library PSFs by using a version of the Anderson et al. (2006) computer program adapted to UVIS/WFC3 and WFC/ACS (see also Bellini et al. 2013). In a nutshell, we divided each image into a grid containing $n \times n$ cells, with n ranging from 1 to 5. Bright, isolated, and unsaturated stars within each cell are fitted by the library PSF model, and the residuals of the fit are iteratively used to improve the PSF model itself. We calculated the appropriate PSF model of each star based on its location in the detector by linearly interpolating the four nearest PSFs of the grid (Anderson & King 2000). The number of cells in the grid has been fixed with the aim of obtaining the best quality-fit parameters for bright stars and depends on the number of available reference stars used to constrain the PSF perturbation in the cell.

These PSFs are then used to measure the magnitudes and positions of unsaturated stars in each image. Saturated stars in the UVIS/WFC3 and WFC/ACS images are measured using the methods by Gilliland (2004) and Gilliland et al. (2010). These authors noted that the total number of electrons of saturated stars in the UVIS/WFC3 and WFC/ACS detectors is conserved and this information is preserved in the _flt images with gain = 2. Hence, we measured each saturated star in an aperture of 5-pixel radius and added the contiguous saturated pixels that had bled outside this radius (see Anderson et al. 2008, for details).

All catalogs derived from each filter and camera have been tied to the same photometric zero point, corresponding to the zero point of the deepest exposure in the filter that we used as a reference frame to construct the photometric master frame. To do this, we used the bright, unsaturated stars that are well-fitted by the PSF to calculate the difference between the magnitudes in the master frame and in each exposure. We used the mean of these magnitude differences to transform stars measured in each exposure into this reference frame.

Stellar positions are corrected for geometric distortion by using the solutions provided by Anderson & King (2006) for WFC/ACS and Bellini & Bedin (2009) and Bellini et al. (2011) for UVIS/WFC3. The coordinates of stars in all images of each cluster are transformed into a common reference system based on *Gaia* Early Data Release 3 (eDR3) catalogs

(Gaia Collaboration 2021), in such a way that the abscissa and the ordinate are aligned with the west and north directions, respectively. We first de-projected the right ascension and declination into the plane tangential to the center of the main cluster in the field. We assumed for these coordinates a scale factor of 0.04 arcsec per pixel. We first used bright, unsaturated stars that are well-fitted by the PSF to derive the six-parameter linear transformations used to convert the coordinates of all stars in each exposure into this reference frame. Then, we derived the 3σ-clipped average stellar positions to derive a new astrometric catalog, which we used as a master frame to improve the transformations.

2.2. Multi-pass photometry

The main outcomes from first-pass photometry, including PSF models, coordinate transformations, photometric zero points, stellar magnitudes, and positions, are used to simultaneously identify and measure all point-like sources in all exposures. To do this, we used the FORTRAN computer program KS2 developed by Jay Anderson (e.g., Sabbi et al. 2016; Bellini et al. 2017; Nardiello et al. 2018), which is the evolution of "kitchen sink", originally written to reduce WFC/ACS images (Anderson et al. 2008). KS2 exploits various iterations to find and measure stars. It first identifies the brightest and most isolated stars, calculates their fluxes and positions, and subtracts them from the image. In the subsequent iterations, it finds, measures, and subtracts stars that are gradually fainter and closer to neighbor stars. We used the stellar positions and magnitudes derived from first-pass photometry to generate appropriate masks for bright stars, including saturated ones. These masks optimize the detection and measurement of faint sources that are close to bright stars. They also minimize the detection of spurious sources that are typically associated with diffraction spikes and other structures of the stellar profile.

This program adopts three distinct methods for measuring stars, each providing optimal photometry for different ranges of stellar luminosity and density. Method I is optimal for relatively bright stars. It provides accurate measurements of all stars that generate distinct peaks within their local 5×5-pixel raster after neighbor stars are subtracted. Each star is measured by using the PSF model corresponding to its position, while the sky level is estimated from the annulus between 4 and 8 pixels from the center of the star.

Method II provides the best photometry for faint stars, which do have not enough flux to provide robust fits with the PSF. After subtracting neighbor stars, KS2 performs the aperture photometry of the star in the 5×5 pixel raster. Each pixel is properly weighted to ensure low weight to those pixels contaminated by nearby stars. The sky is calculated as in Method I.

Method III provides the best photometry in very crowded regions and for faint stars when a large number of exposures are available. It works as Method II, but aperture photometry is calculated over a circle with a radius of 0.75 pixels and the local sky in the annulus between 2 and 4 pixels from the position measured during the finding stage.

Stellar fluxes and positions are measured in each exposure separately and then are properly averaged together to derive our best determinations of magnitudes and positions.

Figure 1 compares the CMDs of stars in the field of view of Lindsay 1 obtained from the three methods. We have chosen this GC as an example because of the deep $F275W$ and $F814W$ photometry available, which comprises 16 and 7 exposures in $F275W$ and $F814W$, with total integration times of 27 341 s and 2206 s, respectively. A visual comparison of the top panels reveals that methods II and III are optimal for faint stars as they provide well-defined MSs. The latter method provides slightly better photometry for stars at the bottom of the MS alone, whereas Method II provides the best photometry for the remaining faint MS stars as highlighted in the middle panels, where we show the zoomed CMDs for MS stars with instrumental $-6 < F275W < -4$ mag[1]. Clearly, the MS plotted in the central panel is much narrower and better defined than that shown in the left and right panels. On the contrary, Method I provides the best photometry for stars with bright instrumental magnitudes as demonstrated by the narrow red-giant branch (*) and

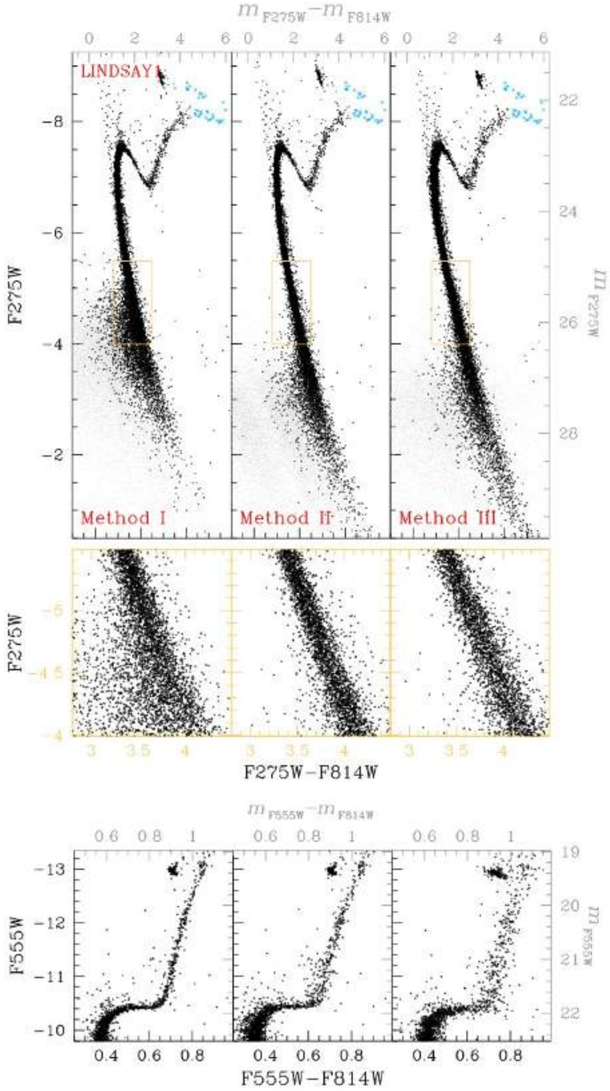

Fig. 1. Comparison of the instrumental $F275W$ vs. $F275W-F814W$ CMDs of stars in the field of view of the star cluster Lindsay 1 as derived from Method I (*top-left*), Method II (*top-middle*) and Method III (*top-right*). Well-measured stars are colored black, while stars with poor photometry are plotted with light gray dots. Azure crosses mark stars where the $F814W$ magnitude is derived from saturated images. *Middle panels*: are zoomed-in views of the top-panel CMD around the MS. *Bottom panels*: compare the region of the instrumental $F555W$ vs. $F555W-F814W$ CMDs populated by bright stars with $F555W < -9.75$ mag. Calibrated magnitudes and colors are indicated by the top and right axes.

---

[1] Instrumental magnitudes are defined as the $-2.5\log_{10}$ of the detected photo-electrons.

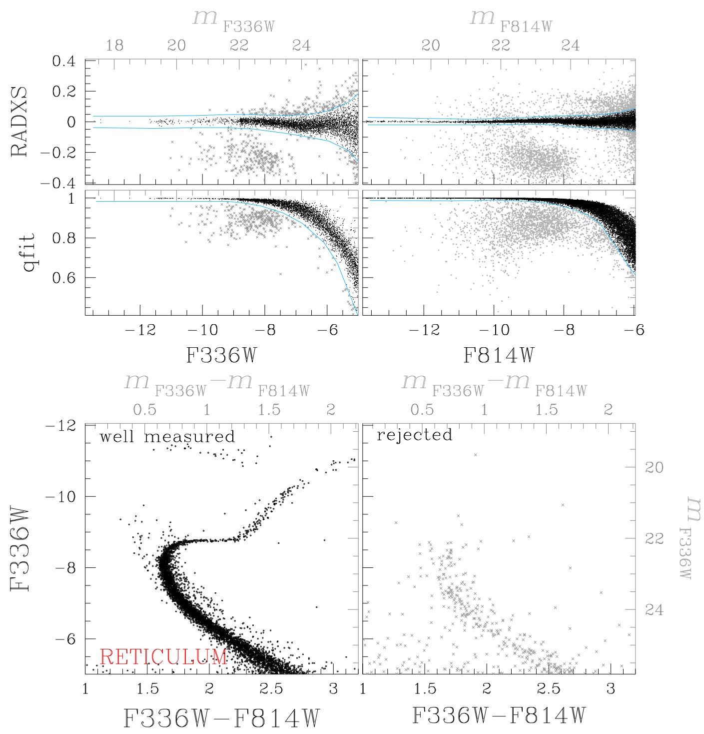

Fig. 2. Procedure to select stars with high-quality photometry and astrometry. *Top panels*: *RADXS* and *qfit* parameters derived from *F*336*W* (*left*) and *F*814*W* (*right*) photometries of stars in the field of view of Reticulum. The azure lines separate well-measured stars (black dots) from poorly measured sources (gray crosses). *Bottom panels*: instrumental *F*336*W* vs. *F*336*W*−*F*814*W* CMD for stars that pass the selection criteria in both filters (*left*) and for the remaining stars (*right*).

sub-giant branch (SGB) sequences in the bottom-left *F*555*W* versus *F*555*W*−*F*814*W* CMDs. For each field, we derived three distinct catalogs from Methods I, II, and III. The science results shown in this paper, which are all focused on bright stars, are based on the photometry derived from Method I.

2.3. Photometry calibration

Photometry of each filter and camera has been calibrated to the Vega mag system by computing the aperture correction to the PSF-fit-derived magnitudes and applying to the corrected instrumental magnitude a photometric zero-point. To calculate the aperture corrections, we used unsaturated and isolated stars only.

We measured aperture magnitudes within circular regions of ∼0.4 and 0.5 arcsec radius for UVIS/WFC3 and WFC/ACS, respectively. To do this, we used the drizzled and CTE-corrected (_drc,) images, which are normalized to 1 s exposure time. Aperture photometry has been calibrated by adding to these instrumental magnitudes the corresponding aperture corrections and the zero points (Bohlin 2016; Deustua et al. 2017). Finally, we calculated the 3σ-clipped average of the difference between instrumental PSF magnitudes and calibrated aperture magnitudes for the stars in common. The resulting average values are then added to all the stars to derive calibrated magnitudes.

2.4. Quality parameters

The computer program KS2 computes for each star various parameters that can be used as diagnostics of the photometric and astrometric quality. For each filter it provides three main quantities: First, the *RADXS* parameter is a shape parameter that indicates the amount of flux that exceeds the predictions from the best-fitting PSF (Bedin et al. 2008). It is defined as $RADXS = (\sum_{i,j} \mathrm{pix}_{i,j} - \mathrm{PSF}_{i,j})/10^{-\mathrm{mag}/2.5}$ where the sum is calculated within an annulus between 1.0 and 2.5 pixels from the center of the star and is normalized to the star's total flux. This quantity is negative when the object is sharper than the PSF (e.g., cosmic rays and PSF artifacts) and it is positive when the object is broader than the PSF (e.g., galaxies). The perfect PSF fit corresponds to $RADXS = 0$.

The second is the quality-fit parameter, $qfit$, which is indicative of the goodness of the PSF fit. It is defined as $qfit = \frac{\sum_{i,j} \mathrm{pix}_{i,j}\mathrm{PSF}_{i,j}}{\sqrt{\sum_{i,j} \mathrm{pix}^2_{i,j}\mathrm{PSF}^2_{i,j}}}$, and it is calculated in a 5×5 pixel area centered on the star, and $\mathrm{pix}_{i,j}$ and $\mathrm{PSF}_{i,j}$ are the values of the pixel and the best-fitting PSF model, respectively, estimated in the pixel (i, j). It ranges from unit, in the case of a perfect fit, to zero. The final quantity is the root mean scatter of the magnitude determinations, rms.

As an example, in the top-left panels of Fig. 2 we plot the *RADXS* and $qfit$ parameters derived from *F*336*W* photometry of the star cluster Reticulum as a function of the *F*336*W* instrumental magnitude. Top-right panels show the analogous figures but for the *F*814*W* filter. The bulk of well-measured point-like sources are separated from sources that are poorly fitted by the PSF model. The bottom panels compare the CMD of stars that pass the selection criteria in both filters and the CMD of stars that have been rejected in at least one filter. Although the magnitude rms is another diagnostic of photometric quality, we prefer not to use it to select the sample of stars with high-quality measurements to avoid excluding variable stars.

2.5. The color-magnitude diagrams

In the four panels of Fig. 3 we show the m_{F336W} versus $m_{F336W} - m_{F814W}$ (left) and the m_{F555W} versus $m_{F555W} - m_{F814W}$ (right) Hess diagrams of all the observed fields in the LMC (top) and SMC (bottom). Clearly, these diagrams reveal the complexity of stellar populations in the Magellanic Clouds, from bright and blue MSs composed of young and metal-rich stars to old and metal-poor stellar populations characterized by blue and faint MSs and faint RGBs.

To further illustrate the variety of stellar populations and environments contained in the data set of this paper, we show in Fig. 4 the stacked images and the CMDs of stars in three distinct fields that host stellar populations with different stellar densities, ages, and metallicities. The *F*475*W* image and the CMD of stars in the field around the open cluster NGC 1966 are plotted in the top panels. This region, which has never been studied with HST, hosts a conspicuous population of very young stars that populate the upper MS and the pre-MS. The CMD also reveals old-RGB and red-clump stars that likely belong to foreground and background LMC old stellar populations. Notably, the region hosts various nebula like NGC 1965 and the gas nebula around the Wolf-Rayet star HD-269546 (the brightest star visible in the stacked image, Westerlund & Smith 1964), which are visible here in unprecedented detail. The figures in the middle and bottom panels refer to the regions around the intermediate-age cluster NGC 2121 (age ∼ 3 Gyr) and the dense and old GC NGC 2210 (age ∼ 12 Gyr), respectively.

The CMDs are used to estimate age, distance modulus, $(m-M)_0$, metallicity, [M/H], and reddening, $E(B-V)$, by using isochrones from the Padova database (Marigo et al. 2017). To minimize the contamination of field stars, we excluded from

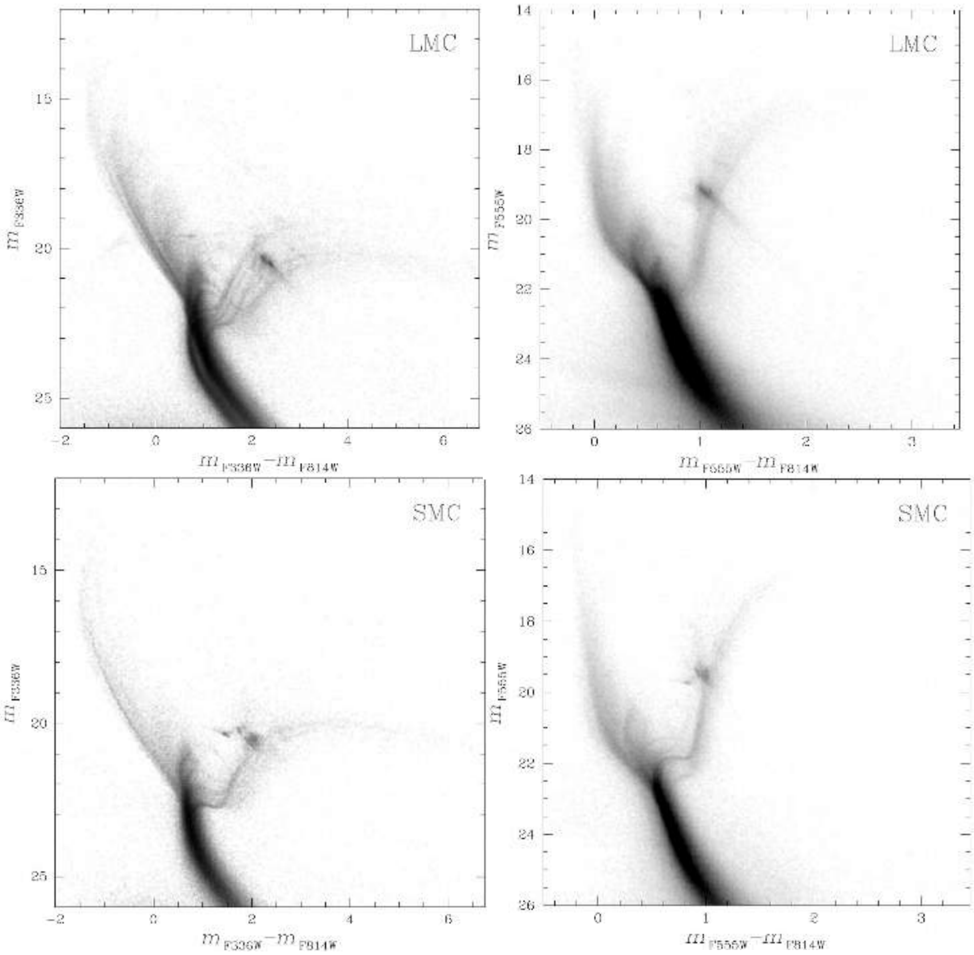

Fig. 3. m_{F336W} vs. $m_{F336W} - m_{F814W}$ (*left panels*) and m_{F555W} vs. $m_{F555W} - m_{F814W}$ (*right panels*) Hess diagrams for all LMC (*top*) and SMC stars (*bottom*).

the analysis the stars at a large distance from the cluster center. Moreover, we statistically subtracted the field stars from the CMD of cluster members by using the method of Gallart et al. (2003), in close analogy with what is done in previous papers from our group (e.g., Marino et al. 2014; Milone et al. 2018). In a nutshell, we defined by eye a region that is centered on the cluster and includes the bulk of cluster stars (hereafter cluster field) and a reference field with the same area, and at a large distance from the cluster center, which is mostly composed of field stars. We associated with each star in the reference field, the star in the cluster field at the smallest distance in the CMD, where the distance is defined as distance = $\sqrt{(k \times \Delta\mathrm{color})^2 + (\Delta\mathrm{magnitude})^2}$, where Δcolor and Δmagnitude are the color and magnitude differences, respectively, and k is a factor that enhances the difference in color with respect to the magnitude difference, which is derived as in Marino et al. (2014, see their Sect. 3.1). These stars are excluded from the comparison with the isochrones. The cluster parameters and the best-fitting isochrones are used in Sect. 3 to estimate differential reddening maps and to investigate the eMSTO phenomenon (Sect. 6). To find the best-fitting isochrone, we used the CMD from the UVIS/WFC3 and/or WFC/ACS photometry providing the widest color baseline, thus maximizing the sensitivity to metallicity. However, when photometry in optical filters is available, we excluded the UV filters $F225W$, $F275W$, $F336W$, and $F343N$ from the analysis to minimize the effect of multiple populations[2]. Indeed, these UV filters are sensitive to the potential effects due to stellar populations with different nitrogen and oxygen abundances, (e.g., Marino et al. 2008; Milone et al. 2020; Dondoglio et al. 2021), which are typical features of GCs older than ~2.3 Gyr, and to stellar populations with different rotation rates (e.g., D'Antona et al. 2015; Milone et al. 2016; Li et al. 2017; Marino et al. 2018a), which are present in all clusters younger than ~2 Gyr.

The observed CMDs are compared with grids of isochrones with different reddening values, distances, metallicities, and ages. The resulting best-fitting parameters are provided in Table B.2 and are estimated as follows.

We first determined the isochrone and the values of reddening and distance modulus that, based on the visual comparison with the CMD, provide the best match with the CMD. Then, we improved the determination of the best-fitting parameters using the following iterative approach. We fixed the values of age, distance, and reddening and better constrained the cluster metallicity by comparing the slopes of the fiducial lines of the observed RGB and the MS of the CMDs, and the slope of the corresponding magnitude intervals of the isochrones.

Then, we assumed the metallicity value corresponding to the minimum difference between the slopes of the observed CMDs and the isochrones to improve the estimates of reddening, age, and distance modulus. To do this, we adopted the criteria of

---

[2] These UV filters encompass various molecular bands that include carbon, nitrogen, and oxygen. Their fluxes are sensitive to the abundances of these elements, which are not constant within clusters with multiple populations. Hence, the CMDs made with UV filters may lead to less accurate determinations of the cluster parameters than optical CMDs.

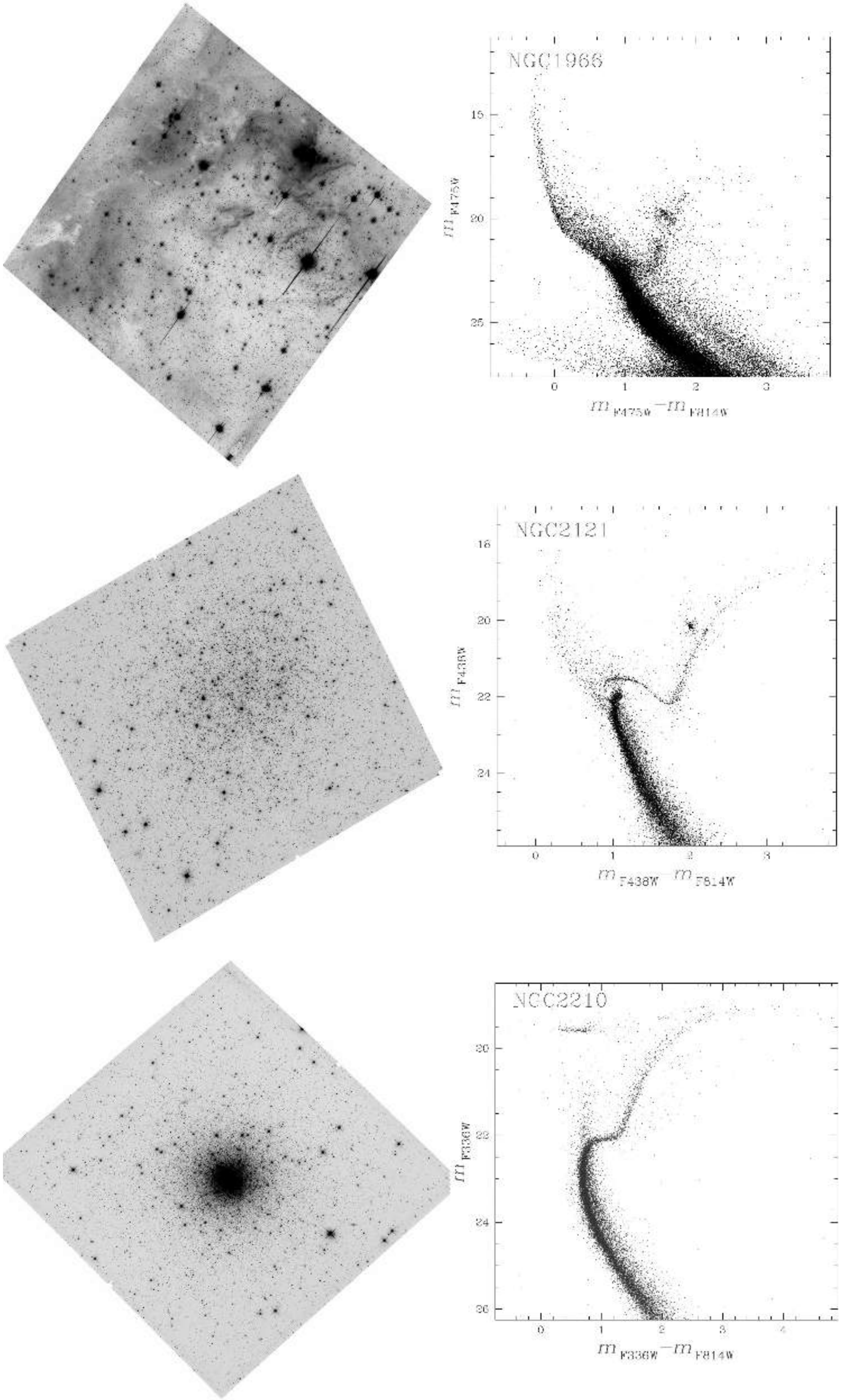

Fig. 4. Stacked images and CMDs of stellar fields with different ages and stellar densities. North is up and east to the right. *Top panels*: $F475W$ image and the m_{F475W} vs. $m_{F475W}-m_{F814W}$ CMD of stars in the star-forming region around the very young cluster NGC 1966. *Middle* and *bottom panels*: illustrate the $F814W$ stacked images and the CMDs of the intermediate-age cluster NGC 2121 (age ~ 3 Gyr) and the old GC NGC 2210 (age ~ 12 Gyr), respectively.

obtaining the best match between the isochrone and the observed CMD, which may change for clusters with different ages.

The best-fitting parameters of clusters older than ~2.3 Gyr were estimated by determining the isochrone that best fits the CMD from the main-sequence turnoff (MSTO) through the SGB (e.g., Dotter et al. 2010). Specifically, we calculated the χ^2 values of the distances in the CMD between the fiducial lines of the MSTO and SGB stars and the isochrone. The best-fitting values of age, reddening, and distance modulus are derived by means of χ^2 minimization. A visual inspection at the CMDs reveals that all clusters between ~10 Myr and ~2.5 Gyr exhibit eMSTOs. Since the eMSTOs challenge their age determinations we provide two age values. We list in Col. 11 of Table B.2 the age of the isochrone that best fits the lower part of the eMSTO. Clearly, this age value would represent the oldest cluster stars, if the eMSTO is entirely due to age variation. Alternatively, if the eMSTO is entirely due to rotation, our age estimate would provide an upper limit to cluster age, as the fast-rotating stars populate the lower part of the eMSTO (e.g., Dupree et al. 2017; Marino et al. 2018a,b; Kamann et al. 2020). Hence, we provide in Col. 12 of Table B.2 the age of the isochrone that best fits the upper part of the eMSTO. In the clusters younger than ~10 Myr, where it is challenging to identify the MSTO, our age determination is largely based on evolved stars. In these young clusters and in the clusters with the eMSTO, the age, distance modulus, and reddening were derived by eye.

To quantify the typical precision of the values of metallicity, age, reddening, and distance modulus inferred by the isochrones we applied the following procedure to four couples of clusters with different ages. The photometry of the clusters of each pair comes from data sets with large differences in the number of images and in the total exposure times. Hence, the range of uncertainties on the fitting parameter inferred from each couple of clusters would comprise the parameters' uncertainties of all studied clusters with similar ages.

We first linearly added to the slopes of the fiducial lines of the RGB and MS stars that were used to constrain the metallicity, the corresponding errors. Hence, we derived the best value of [Fe/H] that corresponds to the isochrone that provides the best match with the used slope. We repeated the same procedure but by using the slopes of the MS and RGB fiducials after subtracting the errors. We consider the semi-difference between the maximum and the minimums [M/H] value, Δ[M/H] as a quantity indicative of the precision of our metallicity estimate.

Similarly, we shifted each point of the fiducial line of the MS and the SGB to the bright and blue side of the CMD, perpendicular to the isochrone. We indicate the resulting line as blueshifted fiducial. The shift is applied in such a way that 68.27% of the stars on the blue side of the original fiducial line are located on the red side of the blueshifted fiducial. We applied a similar procedure to derive a redshifted fiducial line. Hence, we repeated four times the procedure described above to estimate the values of age, reddening, and distance modulus but by assuming the various combinations of the largest and minimum values of [M/H] and the blueshifted and redshifted fiducials. We consider the semi-differences between the maximum values of age (Δage), distance modulus, ($\Delta(m-M)_0$), and reddening ($\Delta E(B-V)$), as a proxy of the precision of the estimates of the corresponding quantities.

The results are listed in Table B.3 for the pairs of clusters of old GCs NGC 2005 and NGC 1939 (ages of ~13 Gyr), intermediate-age clusters Kron 3 and Kron 1 (ages of ~6–7 Gyr). We also investigated the ~2 Gyr old clusters NGC 1846 and Hodge 7 and the young clusters NGC 1866 and BSDL 1650 (ages of ~300 Myr).

3. Differential reddening

To derive high-resolution reddening maps, we applied to our data set the method originally developed by Milone et al. (2012) to correct the ACS/WFC $F606W$ and $F814W$ magnitudes of Galactic GCs for differential reddening (see also Bellini et al. 2017; Jang et al. 2022). The main difference of the adopted procedure is that the catalogs of several GCs comprise photometry in more than two bands. The main steps of our iterative method, which is illustrated in Fig. 5 for NGC 416, can be summarized as follows: First, we built the m_{F814W} versus $m_X - m_{F814W}$ diagrams, where $X = F275W, F336W, F343N, F438W, F555W$, and $F814W$. Each diagram has been used to gather information on differential reddening from a sample of reference stars. Reference stars are selected in the CMD region where the reddening direction defines a wide angle with the cluster fiducial line in such a way that we can easily disentangle the effect on stellar colors and magnitudes due to differential reddening from the shift due to photometric uncertainties. As an example, panel a of Fig. 5 highlights in black the selected reference stars of NGC 416 in the m_{F814W} versus $m_{F336W} - m_{F814W}$ CMD.

We then first derived the reddening direction corresponding to each star as $\theta = \arctan\frac{A_X}{A_X - A_{F814W}}$, where A_X and A_{F814W} are the absorption coefficients in the X and $F814W$ bands, respectively. To derive them, we identified the point on the best-fitting isochrone with the same m_X magnitude as the reference star and calculate the m_X and m_{F814W} magnitude differences with the corresponding point of the isochrone with $E(B-V) = 0$ mag. This procedure allows us to account for the dependence of reddening direction from the total amount of reddening and from its spectral type. As an example, panel a of Fig. 5 shows the reddening direction associated with the reference star indicated by the red cross.

Next, we translated the CMD into a new reference frame where the origin corresponds to the reference stars as illustrated in panels a and b of Fig. 5. This CMD is rotated counterclockwise by an angle θ so that the abscissa and the ordinate of the new reference frame are parallel and orthogonal, respectively, to the reddening direction.

We then generated the fiducial line of MS, SGB, and RGB stars, which we plot as a continuous red line in panel b. To do this, we divided the sample of MS stars into "ordinate" intervals. For each bin, we calculated the median abscissa associated with the median ordinate of the stars in the bin. The fiducial line has been derived by linearly interpolating these median points. We next calculated the distance of the reference star from the fiducial line along the reddening direction, $\Delta X'$ as shown in panel b for a reference star of NGC 416[3].

Finally, we calculated the projection of $\Delta X'$ along the $m_X - m_{F814W}$ color direction, $\Delta\,(m_X - m_{F814W})$ and plotted this

---

[3] The differential reddening is responsible for shifting the stars along the reddening line. The amount of such a shift, which is proportional to the amount of reddening along the line of sight, depends on the star's position in the field of view. As a consequence, the stars in the different regions of the field are systematically shifted toward larger or lower values of X' with respect to the cluster fiducial line depending on whether they are affected by a larger or smaller amount of reddening with respect to the median cluster reddening (see Fig. 5 for an example). On the contrary, photometric errors are responsible for a random scatter along the fiducial line, but such a scatter is essentially not dependent on the reddening direction and the position of the star in the field of view.

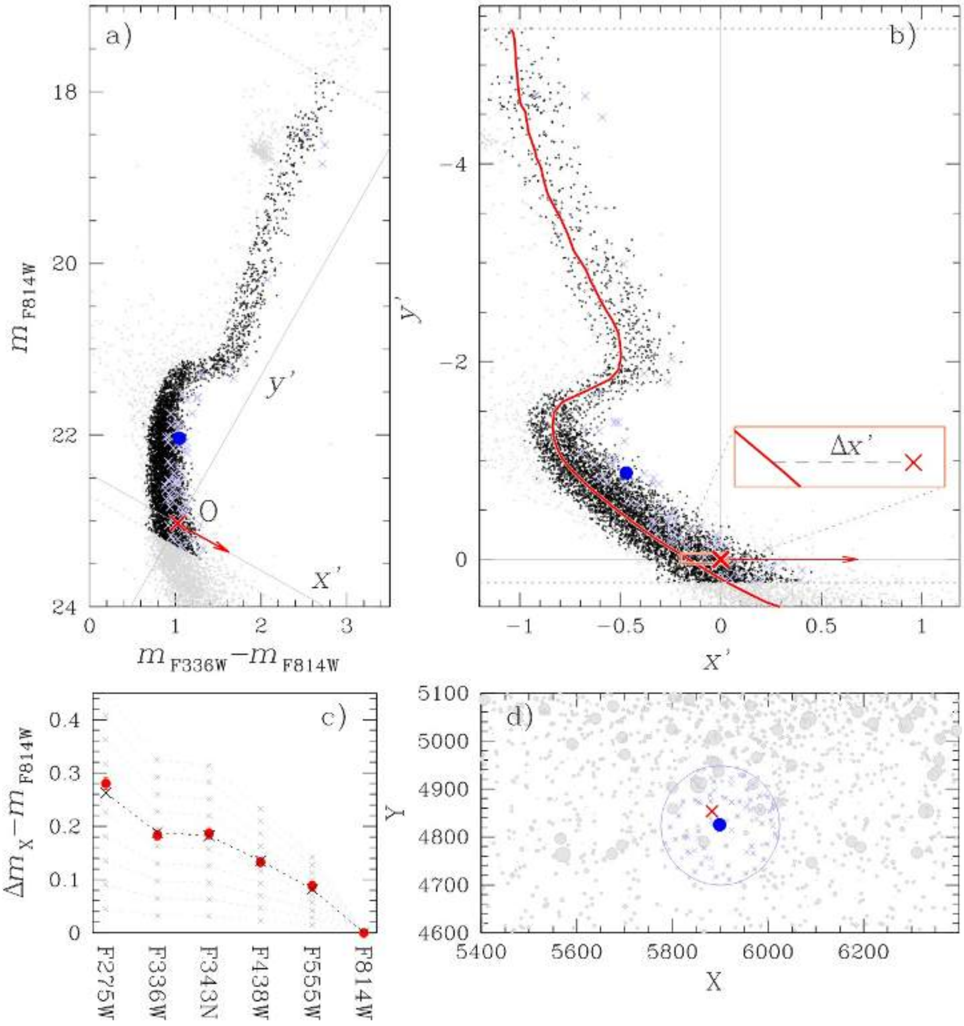

Fig. 5. Illustration of the procedure for estimating the amount of differential reddening associated with the target star, represented with the large blue dot. *Panel a* shows the m_{F814W} vs. $m_{F336W}-m_{F814W}$ CMD of all the stars. Reference stars, are located between the two dotted gray lines and are colored black, whereas the neighboring reference stars are marked with light blue crosses. The gray continuous lines are the abscissa and the ordinate of the rotated reference frame centered on the reference, which is star marked with the large red cross, while the red arrow indicates the reddening direction. *Panel b* shows the same stars as panel a but in the rotated reference frame. The red continuous line is the fiducial of reference stars, and the inset highlights the relative position between one reference star and the fiducial. *Panel c* shows the values of $\Delta X'$ inferred from different filters (red dots). Gray crosses are the corresponding values derived for $\Delta E(B-V)$ and range from 0.01 to 0.10 mag in steps of 0.01 mag, while the black crosses provide the best fit to the observations and correspond to $\Delta E(B-V) = 0.058$ mag. Finally, the finding chart zoomed in around the target is illustrated in *panel d*. See the text for details.

quantity for the available X filters as shown in panel c of Fig. 5. The observed values of Δ $(m_X - m_{F814W})$ are compared with corresponding quantities derived from the isochrones and corresponding to reddening variations ranging from $\Delta E(B-V) = -0.3$ to 0.3 mag in steps of 0.001 mag. The value of $\Delta E(B-V)$ that provides the minimum χ^2 is assumed as the best differential-reddening estimate associated with the reference star marked with the red cross.

To derive the amount of differential reddening associated with each star in the catalog, we selected a sample of N spatially nearby reference stars (light blue crosses in Fig. 5), as shown in panel d. The best determination of differential reddening is provided by the median of the $\Delta E(B-V)$ values of these N neighbors. We excluded the target star from its own differential reddening determination. We derived various determinations of differential reddening by assuming different values of N, from 35 to 95 in steps of 5 and from 100 to 150 in steps of 10. For each determination, we calculated the pseudo-color distances between the value of X' of the reference stars, corrected for differential reddening, and the fiducial line of Fig. 5. We assumed that our best determination of differential reddening is given by the value of N that provides the minimum value of the rms of these distances. In particular, we used $N = 75$ for NGC 416.

As an example, Fig. 6 shows the reddening map in the direction of NGC 416 and compares the original CMD to the CMD corrected for differential reddening. A collection of reddening maps for six clusters is provided in Fig. 7.

4. Cluster centers

To determine the coordinates of the center of each star cluster, we followed the procedure described in Cordoni et al. (2020a). In a nutshell, we first selected by eye a sample of probable cluster members based on their location in the CMD and smoothed their stellar spatial distribution with a Gaussian kernel of fixed size. The kernel size has been chosen with the criteria of favoring the overall shape of the cluster, instead of the small-scale structures. We derived five contour lines within 50 arcsec from the cluster center and interpolated each of them with an ellipse by using the algorithm by Halir & Flusser (1998). Our best cluster-center determination corresponds to the median value of the centers of the ellipses, while the corresponding uncertainty has been estimated as the dispersion of the center determinations inferred from each ellipse. Due to the low number of stars, it was not possible to apply the method above in 13 poorly populated star clusters, namely BRHT 5b, BSDL 1650, KMK 8827, KMHK 1073, KMHK 8849, OGLE-CL-LMC390, NGC 1749, NGC 290, NGC 1850A, NGC 1858, NGC 1938, and NGC 1966. For these clusters, we provide raw center determination based on the peak of the histogram distributions of the

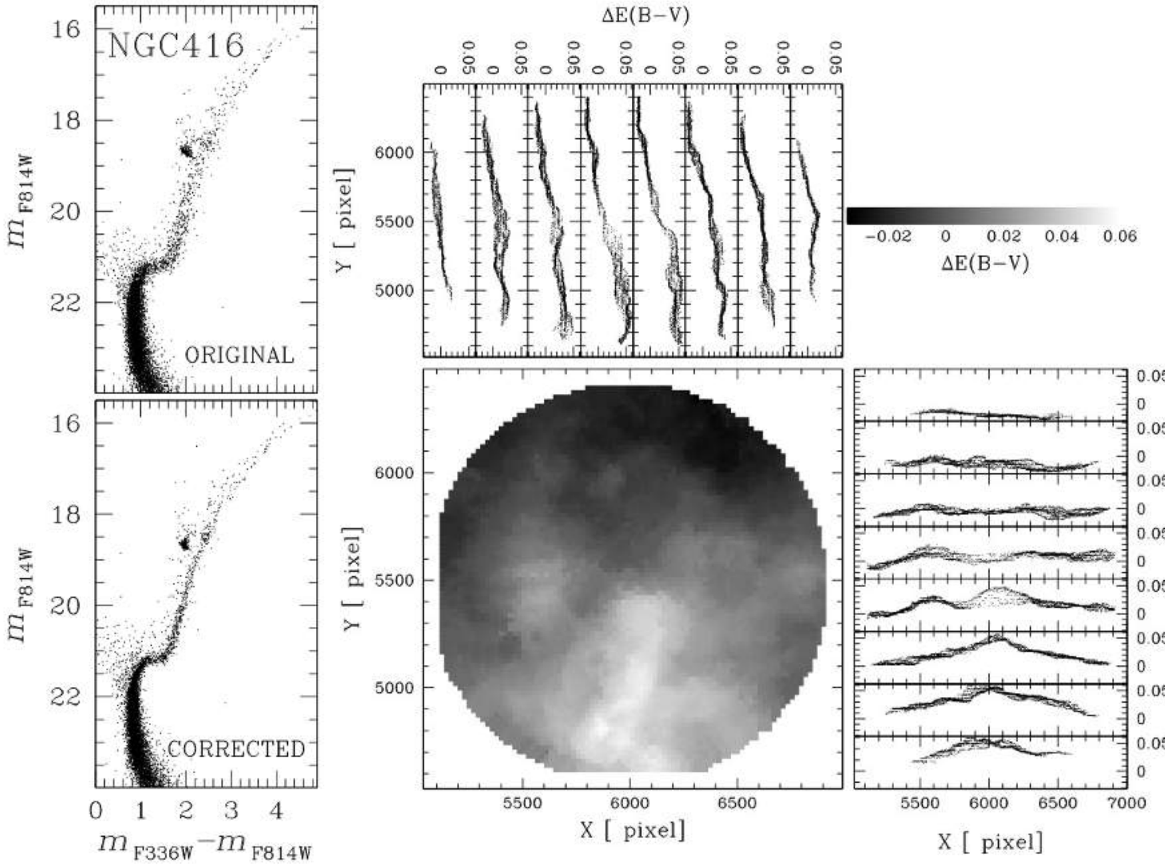

Fig. 6. Results on differential reddening in the direction of NGC 416. *Left*: comparison between the original m_{F814W} vs. $m_{F336W} - m_{F814W}$ CMD of NGC 416 (*top*) and the CMD corrected for differential reddening (*bottom*). *Right*: differential-reddening map in the direction of NGC 416. The levels of gray are proportional to the reddening variation, as indicated in the top right. The panels on the right show $\Delta E(B-V)$ against the abscissa for stars in eight ordinate intervals. Similarly, the panels at the top represent the reddening variation as a function of the ordinate for stars in eight intervals of X. The field is centered around the center of NGC 416 (X, Y = 6019, 5507), and the X and Y axes are parallel to the right ascension and declination direction, respectively. We adopted a scale of 0.04 arcsec per pixel.

coordinates of the probable cluster members. Results are provided in Table B.2.

5. Proper motions

To estimate the absolute proper motions of the studied clusters, we combined information from HST photometry and *Gaia* eDR3 proper motions. Specifically, for each cluster, we selected by eye stars that, based on their positions in all available CMDs, are probable cluster members. Then, we used the *Gaia* eDR3 catalog to select stars with magnitude $G_{BP} < 19.0$ mag, which according to the criteria by Cordoni et al. (2018) have high-quality proper motions. The average proper motion of each cluster has been calculated as the 3-σ clipped average of the proper motions of selected cluster members for which are available both HST photometry and *Gaia* eDR3 high-quality proper motions. We estimated the corresponding uncertainty by following the method of Vasiliev (2019), which accounts for systematic errors.

The main steps of the procedure used to derive the absolute proper motion are illustrated in Fig. 8 for NGC 1806. For this cluster, we have photometry in five photometric bands of UVIS/WFC3 and WFC/ACS. We constructed ten CMDs of stars in the field of view of NGC 1806, including four m_{F814W} versus $m_X - m_{F814W}$ CMDs, where $X = F336W, F343N, F435W$, and $F555W$, three m_{F555W} versus $m_X - m_{F555W}$ CMDs, where $X = F336W, F343N$, and $F435W$, two m_{F435W} versus $m_X - m_{F435W}$ CMDs, where $X = F336W$ and $F343N$, and the m_{F343N} versus $m_{F336W} - m_{F343N}$ CMD. For each CMD, we selected by eye the stars that, based on their colors and magnitudes, are located on the main cluster evolutionary sequences. As an example, the stars that, based on their positions in all CMDs, likely belong to the RGB, asymptotic giant branch, and red clump of NGC 1806 are colored black in the three CMDs of Fig. 8. The colored symbols mark stars with available *Gaia* eDR3 proper motions in both the CMDs and in the proper-motion diagram. The stars that do not belong to the RGB, asymptotic giant branch, and red clump of NGC 1806 in at least one CMD are represented with blue-starred symbols and are not included in the determination of the cluster proper motion. We also excluded the selected stars with proper motions that differ from the average cluster motion by more than three times the proper-motion dispersion (i.e., the stars outside the black circle shown in the bottom-right panel of Fig. 8 represented with aqua-starred symbols). The remaining stars are marked with red open dots.

Results are provided in Table B.1. The left panels of Fig. 9 show the positions of the studied LMC and SMC clusters relative to the SMC center. In the top-left panel, we associate with each cluster the corresponding proper-motion vector, while in the bottom-left panel we show the proper-motion residuals after subtracting to LMC and SMC clusters the average motion of the corresponding Magellanic Cloud from

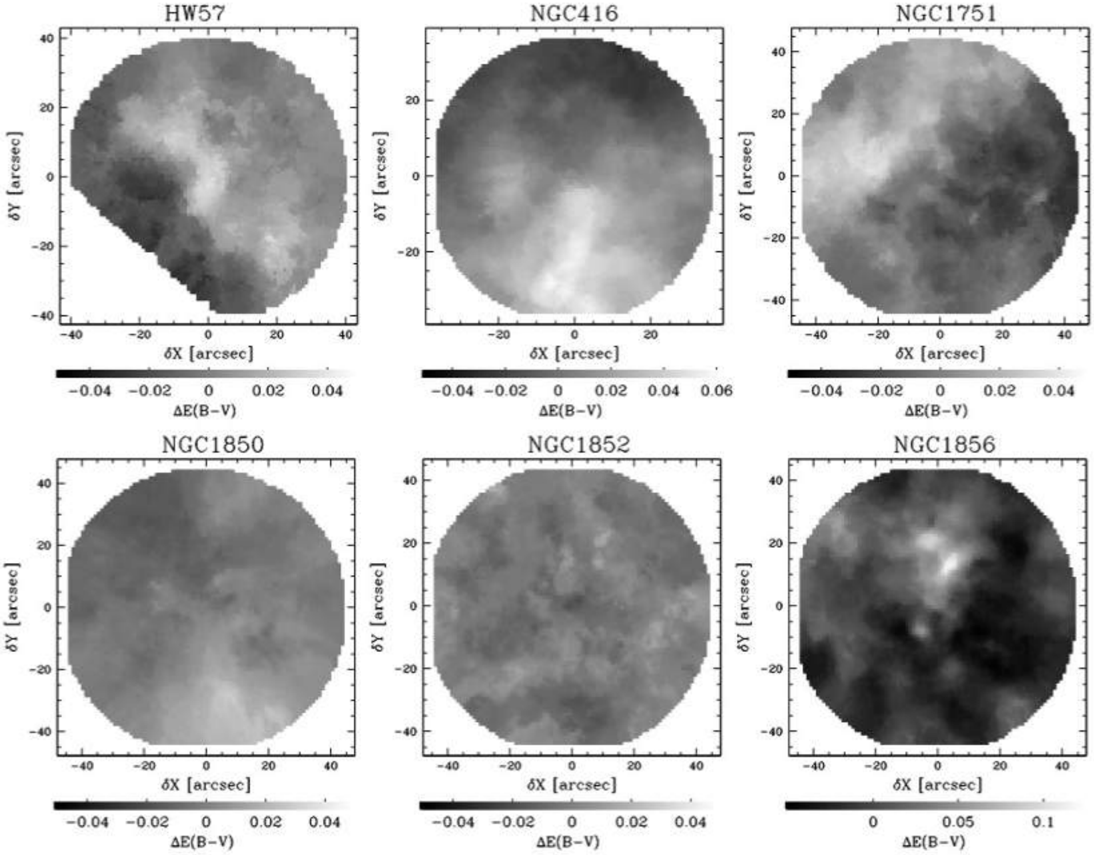

Fig. 7. Differential-reddening maps of the regions in front of HW 57, NGC 416, NGC 1751, NGC 1850, NGC 1852, and NGC 1856.

Gaia Collaboration (2018)[4]. The proper-motion diagram is plotted in the right panel of Fig. 9 and reveals that, based on proper motions, all clusters are consistent with being either LMC or SMC members.

For 13 GCs, we take advantage of having more than one epoch observations with appropriate signal-to-noise ratio and temporal baselines to disentangle the internal kinematics of Magellanic Cloud stars and separate cluster members and field stars by using HST data alone. Detailed information on the HST images available for these clusters are provided in Table B.4. Relative HST motions are then transformed into absolute motions based on *Gaia* eDR3 proper motions.

To derive relative proper motions we applied to our data set the procedure described by Piotto et al. (2012) and described in the following for NGC 1978. In a nutshell, we first identified the distinct groups of images collected at the same epoch through the same filter and camera. We reduced each group of images, separately, as described in Sect. 2, and obtained the corresponding astrometric and photometric catalogs.

The reference frame defined by the first-epoch images collected through the reddest filter is adopted as a master frame. The coordinates of stars in each catalog are transformed into the master frame by means of six-parameter linear transformations (Anderson et al. 2006). To minimize the effect of possible small residual distortions we applied local transformations based on the nearest 70 reference stars. Target stars are never included in the calculation of their own transformations.

The abscissa and the ordinate of each star, expressed in milliarcseconds, are plotted against the epoch, expressed in years, as shown in panels a1–a4 of Fig. 10 for two stars in the field of view of NGC 1978. For simplicity, in this figure, we show the displacements DX and DY, and the time relative to the stellar position and time at the first epoch. These points are finally fitted with a weighted least-squares straight line, whose slope corresponds to the best proper motion estimate.

The selection of the stars used to derive the transformation is a critical step for accurate proper-motion determination. Hence, we selected bright and unsaturated stars that pass the criteria of selection discussed in Sect. 2.4. We derived proper motions relative to a sample of cluster members that have been selected iteratively. As a consequence, the average relative motion of the cluster is set to zero. We first identified probable cluster stars that, based on all available CMDs, lie on the main evolutionary sequences and used them to derive initial proper motion estimates. Then, we iteratively excluded those stars that do not share the same motion as the bulk of cluster members (i.e., stars with proper motions greater than three times the proper-motion dispersion of cluster stars). Panels b and c of Fig. 10 show the probable cluster members that we selected for deriving stellar proper motions in the m_{F814W} versus $m_{F555W} - m_{F814W}$ CMD and in the m_{F814W} versus $DR = \sqrt{DX^2 + DY^2}$ plane, as well as the probable cluster members. Also shown are the remaining stars with

---

[4] Although the investigation of the Magellanic Clouds' rotation is beyond our scope, we note that no clear rotation pattern is evident from the bottom-left panel of Fig. 9. This statement, which is based on a visual inspection of this figure, seems to contrast with the evidence of the LMC rotation pattern shown by van der Marel & Kallivayalil (2014), Helmi et al. (2018). We also note that the right panel of Fig. 9 highlights the relative motions within the SMC following the pattern of the SMC tidal expansion along the bridge and counter-bridge as detected in previous works (e.g., Zivick et al. 2018; Piatti 2021; Dias et al. 2021; Schmidt et al. 2022).

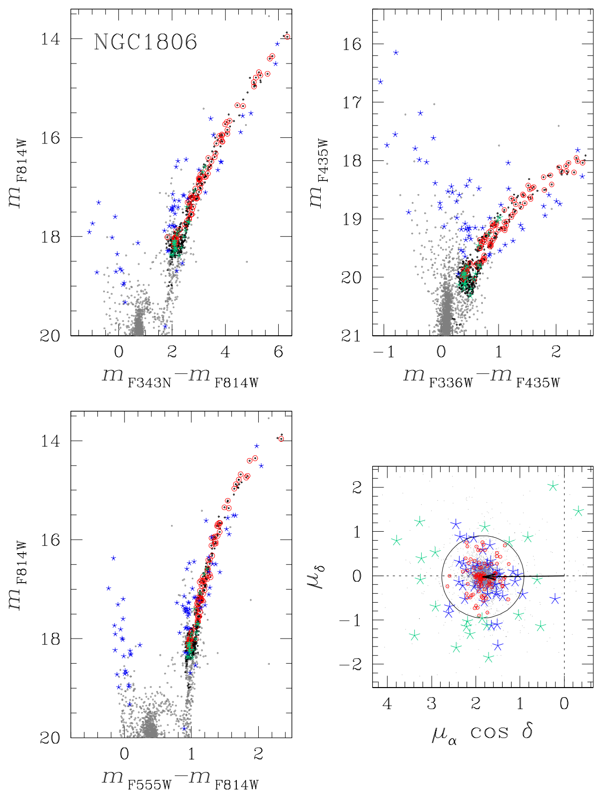

Fig. 8. Procedure for identifying stars that, based on the position in the CMDs from HST photometry and in the proper-motion diagram from *Gaia* eDR3, are probable members of NGC 1806. The probable members are represented with red circles in the CMDs plotted in the *top panels* and the *bottom-left panel* and in the proper-motion diagram shown in the *bottom-right panel*. Stars that are not located on the main evolutionary sequences in at least one CMD are represented with blue stars. The arrow plotted in the proper-motion diagram indicates the mean cluster motion, while the circle is used to select the stars that are not included in the sample of probable cluster members, due to their large proper motions (aqua stars). See the text for details.

cluster-like proper motions: the saturated stars, the faint stars, and the stars that do not lie on the main evolutionary sequences in the CMDs.

To transform relative proper motions into absolute ones we derived the difference between the relative proper motions derived from HST images and the absolute proper motions from *Gaia* eDR3 for an appropriate sample of stars. Specifically, this selected sample includes stars with high-quality relative proper motions (i.e., bright, unsaturated stars that pass the criteria of selection of Sect. 2.4). In addition, the selected sample includes stars that, based on the proper motion uncertainties and on the values of the renormalized unit weight error, the astrometric_gof_al (`As_gof_al`) parameters of the *Gaia* eDR3 catalog have accurate *Gaia* eDR3 absolute proper motions. We refer to papers by Cordoni et al. (2018, 2020b), for details on the procedure. The sample includes both cluster and field stars, with the exception of a few stars with parallaxes significantly larger than zero.

The 3σ-clipped mean differences of the proper motion along each direction ($\mu_\alpha \cos\delta$ and μ_δ) are considered as the best estimate of the zero points of the motions and are used to convert relative proper motions into absolute ones. As an example, panels d1 and d2 of Fig. 10 show the histogram distributions of the quantities $\Delta\mu_\alpha \cos\delta = \mu_\alpha \cos\delta - DX$ and $\Delta\mu_\delta = \mu_\delta - DY$ for stars in the field of view of NGC 1978.

The proper-motion diagrams for NGC 1978 stars are plotted in the left panels of Fig. 11 in four distinct magnitude bins. These diagrams can be used to separate the bulk of cluster members (black dots) from probable field stars (red crosses). Here, the red circles that enclose the NGC 1978 stars have radii equal to 2.5σ, where σ is the average between the σ-clipped dispersion values of $\mu_\alpha \cos\delta$ and μ_δ. For illustration purposes, we only mark in red the most-evident field stars with $\mu_\alpha \cos\delta > 1.6\,\mathrm{mas\,yr^{-1}}$ and a distance of more than $0.2\,\mathrm{mas\,yr^{-1}}$ from the average motion of NGC 1978, while the remaining stars are colored gray. The m_{F814W} versus $m_{F555W} - m_{F814W}$ CMD of probable cluster members and field stars is shown in the right panel of Fig. 11.

6. A saucerful of secrets

The photometry and astrometry of this work are exquisite tools to investigate various astrophysical topics. In this section we provide further examples of science outcomes that arise from visual inspections of the photometric diagrams and of the proper-motion diagrams. Specifically, in Sect. 6.1 we report the discovery of eMSTOs in the clusters KMHK 361 and NGC 265. Section 6.2 compares the CMDs of LMC clusters younger than ∼2.3 Gyr and investigates the color and magnitude distribution of eMSTO in clusters with different ages. Gaps and color discontinuities along the MS of NGC 1783 are investigated in Sect. 6.4 while Sect. 6.5 provides evidence of new features along the eMSTO and the upper MS of NGC 1783. Finally, Sect. 6.6 is focused on the proper motions of the star clusters and of Magellanic Cloud stellar populations in 11 fields.

6.1. Clusters without previous evidence of eMSTO

Figure 12 provides evidence that the CMDs of the star clusters KMHK 361 (age of 1.35 Gyr) and NGC 265 (age of 450 Myr) are not consistent with a single isochrone. In this figure, we compare the CMDs of stars in circular fields centered on the cluster (hereafter cluster fields) and in reference fields of the same area. We adopted radii of 20 and 24 arcsec for KMHK 361 and NGC 265, respectively, enclosing the bulk of cluster stars. To minimize the contamination from cluster stars, the reference fields are as far away from the cluster centers as possible, while still being within the field of view. By assuming a uniform distribution of field stars in the small HST field of view, the distribution of stars in the reference-field CMD is indicative of the contamination due to field stars.

Clearly, KMHK 361 exhibits an eMSTO, which cannot be explained by field-star contamination alone. Similarly, NGC 265 shows an intrinsic eMSTO. The upper MS is split in the $F435W$ magnitude interval between ∼21 and 22 mag, with the red MS hosting about two-thirds of MS stars. The two MSs merge around $m_{F435W} \sim 22.5$ mag. The comparison between the CMDs of stars in the field and reference fields reveals that the split MS and the eMSTO are not due to field-star contamination.

The visual inspection of the CMDs from our survey suggests that all clusters with ages between ∼0.1 and ∼2.3 Gyr exhibit the eMSTO (Cordoni et al., in prep.). These findings corroborate the evidence that eMSTOs are common features of clusters younger than ∼2.3 Gyr, while split MSs are widespread phenomena among clusters younger than ∼0.8 Gyr (e.g., Milone et al. 2009; Milone & Marino 2022; Niederhofer et al. 2015; Goudfrooij et al. 2011; Li et al. 2017; Correnti et al. 2017).

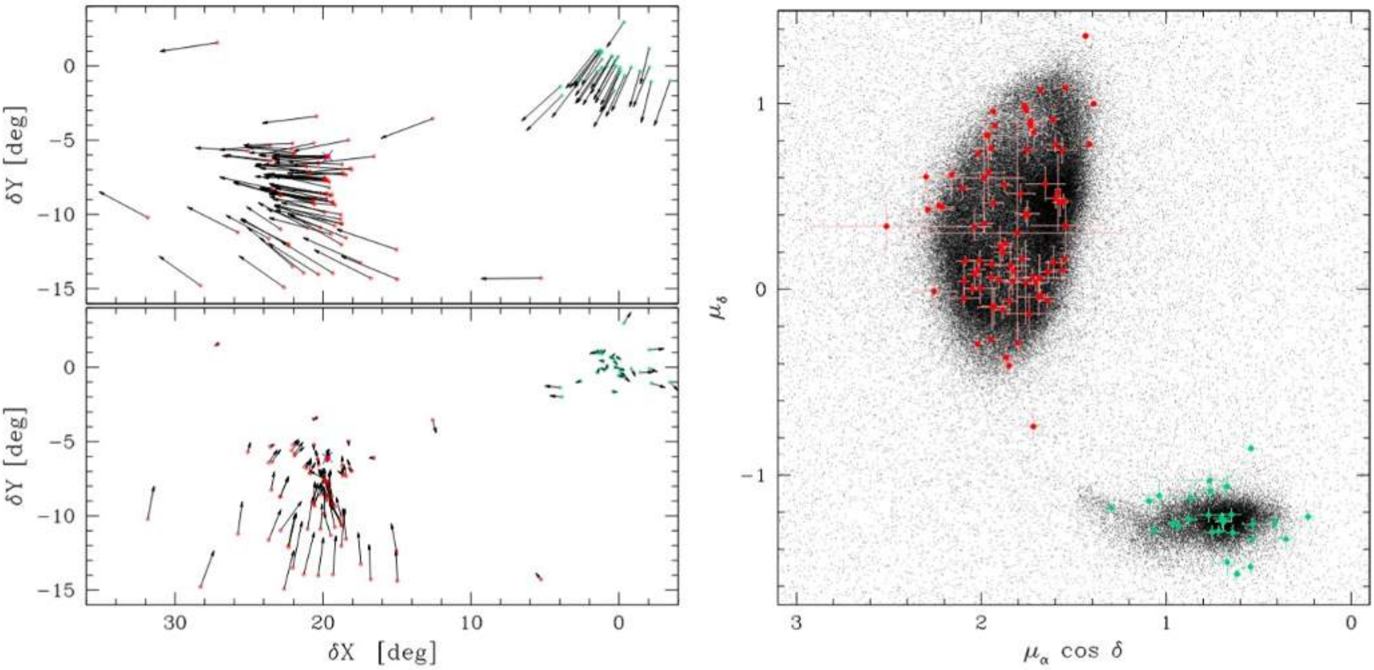

Fig. 9. Results on the absolute proper motions of LMC and SMC star clusters. *Left*: coordinates, in degrees, relative to the SMC center of the studied SMC and LMC clusters. The arrows in the top panel are indicative of the absolute proper motions of each cluster, while the bottom panel represents the proper motions of LMC and SMC clusters after subtracting the average motion of the corresponding galaxy. *Right*: proper motions of stars brighter than $G_{\rm BP}$ = 16.0 mag in the region around the LMC and the SMC (black points). The studied LMC and SMC clusters are plotted in all panels with red and aqua dots, respectively.

6.2. The eMSTO in clusters of different age

Our data set provides a unique opportunity for comparing CMDs of clusters with different ages derived with homogeneous methods. As an example, we take advantage of the collection of M_{F336W} vs. $M_{F336W} - M_{F814W}$ CMDs shown in Fig. 13 to investigate how the eMSTO phenomenon changes as a function of cluster age. In this figure, star clusters are sorted by age, from ~10 Myr (NGC 1818) to ~2.5 Gyr (NGC 1978). The observed magnitudes have been converted into absolute ones by adopting the values of distance modulus and reddening listed in Table B.2.

A visual inspection of this figure corroborates the previous conclusion that the split MS is visible in all LMC clusters younger than ~800 Myr (from NGC 1818 to NGC 1953) and seems to disappear at older ages (Milone et al. 2018). The color separation between the blue and red MSs approaches its maximum value around the MSTO and decreases toward faint luminosities (Milone et al. 2016). As pointed out by Wang et al. (2022), the gap between the blue and red MSs significantly narrows down around M_{F336W} = 1.0 mag, which is the luminosity level where the fraction of blue-MS stars approaches its minimum value (Milone et al. 2018). Noticeably, this magnitude value corresponds to an MS mass of ~2.5 $\mathcal{M}_\odot$, where the slowly rotating component of MS field stars disappears (Zorec & Royer 2012).

We also confirm that the eMSTO is a ubiquitous feature of LMC clusters younger than ~2.3 Gyr. It is visible in all clusters where the turn-off is brighter than the MS bending around M_{F336W} = 3.0 mag and disappears in NGC 1978 (e.g., Milone et al. 2009; Goudfrooij et al. 2014). Since the MS bending is due to a change in the stellar structure, the eMSTO is associated with stars with radiative envelopes alone. In addition, the split MS is visible among stars brighter than the MS bend.

Figure 13 reveals that the color and magnitude distributions of stars across the eMSTO significantly change from one cluster to another. As an example, the Hess diagrams plotted in the top panels a1–a3 of Fig. 14 suggest that most TO stars of NGC 1868 populate the bright and blue region of the eMSTO, whereas NGC 2173 shows higher stellar density on the bottom-red side of its eMSTO. NGC 1852 seems to show an intermediate distribution.

To parametrize the stellar distribution of eMSTO stars in the CMDs, we adopted the procedure illustrated in Fig. 14b for NGC 1852. We defined a new reference frame where the origin, O, is set by hand on the bright and blue side of the eMSTO, and the abscissa, X', envelopes the bright part of the eMSTO and points toward the red. We derived the red and blue fiducials of the eMSTO in the new reference frame and represented them as red and blue lines in the CMD of Fig. 14b. To derive the fiducials, we follow the recipe by Milone et al. (2017), which is based on the naive estimator (Silverman 1986). We first divided the eMSTO into a series of bins with fixed pseudo-magnitude, $\delta Y'$. The bins are defined over a grid of points separated by intervals of fixed pseudo-magnitude ($s = \delta Y/3$). For each interval, we calculate the 4th and the 96th percentile of the X' distribution and associated these values with the mean pseudo-magnitude Y' of stars in the bin. These values are then linearly interpolated to derive the red and blue boundaries of the eMSTO. These lines are used to calculate the quantity

$$\Delta_{X'} = \frac{X' - X'_{\rm blue\,fiducial}}{X'_{\rm red\,fiducial} - X'_{\rm blue\,fiducial}}, \tag{1}$$

which is defined in such a way that the stars on the blue and red fiducials have $\Delta_{X'} = 0$ and 1, respectively.

Figure 14 compares the kernel density (panel c) and the cumulative distributions of $\Delta_{X'}$ (panel d) for NGC 1852 (black), NGC 1868 (aqua), and NGC 2173 (orange). We confirm the visual impression of a predominance of blue eMSTO stars in

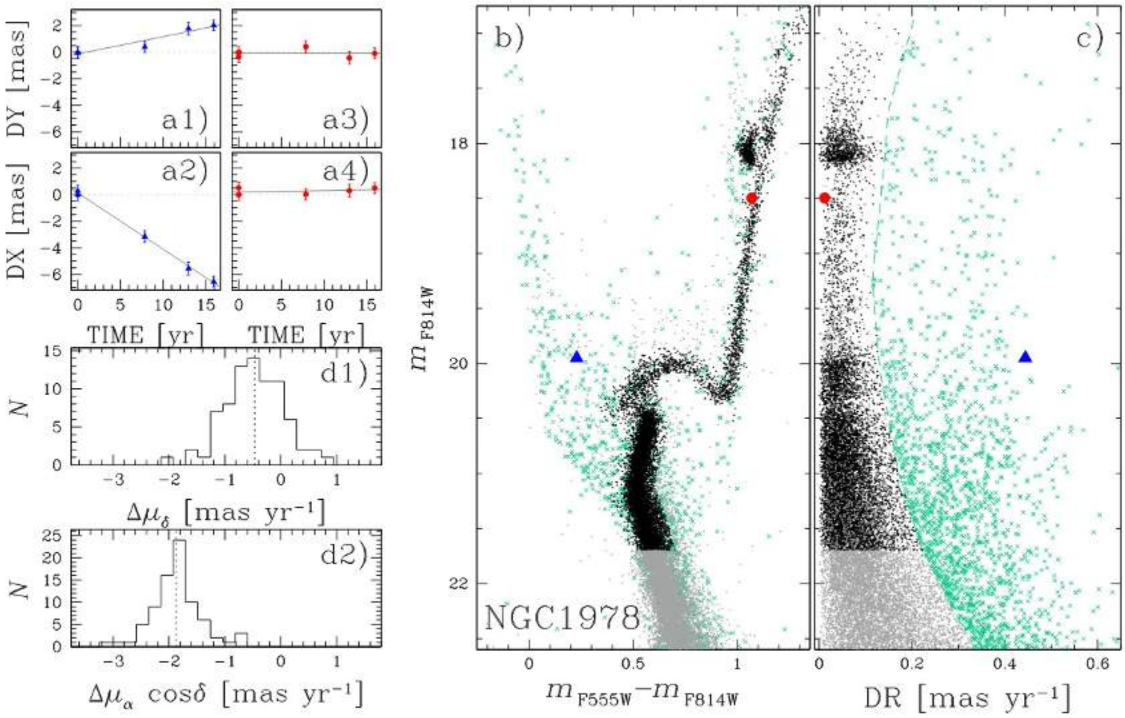

Fig. 10. Procedure for estimating absolute proper motions. *Panels a1 and a2* show the displacements along the *X* and *Y* directions in four epochs of a probable field star (blue triangles) relative to the mean motion of NGC 1978. Similarly, *panels a3 and a4* show the displacements of a candidate cluster member (red dots). The m_{F814W} vs. $m_{F555W} - m_{F814W}$ CMD of stars in the field of view of NGC 1978 is plotted in *panel b*, while *panel c* shows relative stellar proper motions against m_{F814W}. Aqua crosses are probable field stars selected on the basis of their proper motions. The stars used as references to calculate relative proper motions are colored black, while the remaining stars with cluster-like proper motions are gray. *Panels d1 and d2* show the histogram of the difference between our relative proper motions and the absolute proper motions from *Gaia* eDR3.

NGC 1868, whereas the $\Delta_{X'}$ distribution of NGC 2173 is peaked toward the red. NGC 1852 has an intermediate distribution.

To quantify the $\Delta_{X'}$ differences among the various clusters, we define two quantities: (i) the area, A, below the cumulative curve shown in Fig. 14 and (ii) the median value of $\Delta_{X'}$, $\langle\Delta_{X'}\rangle$. If the distribution is dominated by blue and bright MSTO stars we would expect large values of A and small values of $\langle\Delta_{X'}\rangle$, while a predominance of faint and red eMSTO stars corresponds to small A and large $\langle\Delta_{X'}\rangle$. Results are shown in Fig. 15, where we plot both quantities against cluster age. LMC clusters (red dots in Fig. 15) exhibit a strong anticorrelation between A and age and a correlation between $\langle\Delta_{X'}\rangle$ and age, as also indicated by the values of the Spearman's rank correlation coefficients of −0.91 and 0.92, respectively. Intriguingly, the ~2 Gyr old SMC clusters NGC 411 and NGC 416 exhibit larger values of A and smaller values of $\langle\Delta_{X'}\rangle$ than LMC clusters with similar ages, with NGC 411 having the largest differences. The small statistical sample of clusters prevents us from reaching a firm conclusion on whether NGC 411 is an outlier or SMC and LMC clusters exhibit different trends.

The multiple populations of young and intermediate-age star clusters share common features that have been instrumental to shed light on the origin of split MSs and eMSTOs (see Milone & Marino 2022, for a recent review). As an example, the eMSTO width depends on cluster age. Specifically, if the eMSTO is interpreted as an age spread, the resulting age range is proportional to cluster age (e.g., Niederhofer et al. 2015; Cordoni et al. 2018). Moreover, the fractions of stars along the blue and the red MS correlate with stellar mass. The fraction of blue-MS stars varies from ~40% among stars with masses of ~1.5 $\mathcal{M}_{\odot}$ to ~15% among ~2.5–3.0 $\mathcal{M}_{\odot}$ stars. It arises again in more massive stars, up to ~40% in ~5.0 $\mathcal{M}_{\odot}$-stars. The fractions of blue- and red-MS stars do not depend on other properties of the host cluster like the global cluster's mass (Milone et al. 2018). These results have been instrumental to demonstrate that rotation plays a major role in shaping the eMSTOs and the split MSs of Magellanic Cloud clusters.

The evidence that the $\Delta_{X'}$ distribution of stars along the eMSTO depends on cluster age provides a potential further constraint to the eMSTO phenomenon. To start investigating the physical reasons responsible for the relations shown in Fig. 15, we used stellar models from the Padova database (Marigo et al. 2017) to simulate a group of CMDs of nonrotating stellar populations with ages of 100, 200, 500, 1000, 1250, 1500, and 2000 Myr and internal age spreads. We assumed a flat distribution and maximum width corresponding to the average age variations inferred by Cordoni et al. (2018) for Magellanic Cloud clusters with the same age. We derived the A and $\langle\Delta_{X'}\rangle$ quantities for each simulated CMD by using the same procedure adopted for real stars and plotted the resulting values against the oldest age of the simulated stellar population (open triangles of Fig. 15).

Similarly, we simulated another group of CMDs for coeval stellar populations where 33% of stars have no rotation, whereas the remaining 67% of stars have rotation equal to 0.9 times the breakout value. The simulated diagrams have ages of 100, 150, 500, 800, and 1250 Myr and are derived by means of Geneva models (Ekström et al. 2012, 2013; Mowlavi et al. 2012; Wu et al. 2016). We assumed random viewing-angle distributions and adopted the gravity-darkening model by Espinosa & Rieutord (2011) and the limb-darkening effect (Claret 2000). Stellar magnitudes for the available HST filters have been derived using the model atmospheres by

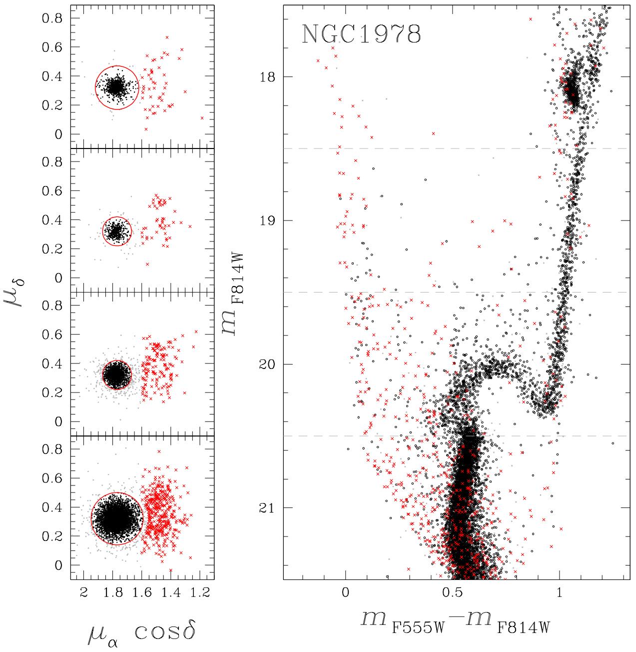

Fig. 11. Proper-motion diagrams of stars in the field of view of NGC 1978 in four $F814W$ magnitude intervals (*left*). The m_{F814W} vs. $m_{F555W} - m_{F814W}$ CMD of stars in the left panels is plotted on the right. Stars within the red circles plotted in the left panels are considered probable cluster members and are colored black, whereas the most-evident field stars are represented with red crosses. The remaining stars are colored gray. See the text for details.

Castelli & Kurucz (2003). The resulting A and $\langle\Delta_{X'}\rangle$ quantities are represented with filled diamonds in Fig. 15. For completeness, we used the Geneva models to simulate nonrotating stellar populations with internal age spreads, in close analogy with what we did with the Padova models. Results are represented with filled triangles.

Clearly, the A and $\langle\Delta_{X'}\rangle$ quantities inferred from both groups of simulated diagrams provide poor fits to the observations. This fact indicates that internal age variation alone is not responsible for the eMSTO when we assume a flat age distribution for all clusters. Similarly, rotation alone is not responsible for the eMSTO when we assume two populations for all clusters: one of nonrotating stars and one of fast rotators with $\omega = 0.9\omega_c$.

It is now widely accepted that the luminosity of eMSTO stars depends on gravity darkening and that its effect is strong for large values of the ratio between the rotational velocity and the critical velocity. Our results could indicate that this ratio increases when stars age on the MS as suggested by Hastings et al. (2020). To properly constrain the contribution of rotation and age variation on the eMSTO, it is mandatory to extend the analysis to simulated diagrams that account for different internal age distributions, for different rotation-rate distributions (e.g., Huang & Gies 2006; Huang et al. 2010; Goudfrooij et al. 2018), and for both age variations and stellar populations with different rotation rates.

The interpretation of the eMSTO phenomenon should also account for binary evolution effects (e.g., Wang et al. 2022). As an example, the stellar models by Wang et al. (2020) show that the fraction of evolutionary-driven mergers rises for smaller stellar masses, at the expense of the binaries that survive the mass transfer and produce spun-up accretors. An appropriate comparison between the observations illustrated in Figs. 14 and 15 and the predictions of stellar models that account for binary evolution is mandatory to shed light on the effect of binary evolution on the eMSTO.

6.3. A population of UV-dim stars along the eMSTO of NGC 1783

The stellar proper motions derived from our data set allow the partial separation of bright field stars from NGC 1783 cluster members, thus providing new insights on its stellar populations. The left panels of Fig. 16 show the proper-motion diagram for stars in the field of view of NGC 1783 in five magnitude bins. The black circles are centered on the absolute proper motion of NGC 1783, and are used to separate probable cluster members (black points) from field stars (aqua crosses).

The corresponding m_{F438W} versus $m_{F438W} - m_{F814W}$ CMD (middle panel) highlights several characteristics of NGC 1783 in unprecedented detail. These include the eMSTO (Mackey et al. 2008; Milone et al. 2009; Goudfrooij et al. 2014) together with a well-populated sequence of MS-MS binaries with large mass ratio (Milone et al. 2009). The SGB also exhibits intrinsic broadening in color and magnitude, with the majority of stars populating the upper SGB. Moreover, the CMD reveals a broad, possibly dual, sequence of stars brighter and bluer than the turn-off. This blue sequence, which will be investigated in detail in Sect. 6.5 was first identified by Li et al. (2016) who associated it with the young stellar populations within NGC 1783. Their result has been challenged by Cabrera-Ziri et al. (2016) who suggested that the blue sequence is composed of field stars.

Here, we focus on the m_{F438W} versus $m_{F275W} - m_{F438W}$ CMD of NGC 1783, which is illustrated in the right panel of Fig. 16. An unexpected feature of this CMD is the sparse cloud of stars on the red side of the eMSTO. These stars, which we dub UV-dim, are marked with red triangles in the left panel of Fig. 17 where we reproduce the m_{F438W} versus $m_{F275W} - m_{F438W}$ CMD zoomed around the eMSTO. UV-dim stars comprise a small fraction of ~7% of the total number of eMSTO stars with $20.4 < m_{F555W} < 21.5$ mag. We used the same colors to represent these stars in the other panels of Fig. 17 and showed that they define distinct sequences in both m_{F435W} versus $m_{F343N} - m_{F435W}$ and m_{F555W} versus $m_{F555W} - m_{F814W}$ CMDs. If the extreme position in the left-panel CMD is due to observational errors alone, the selected stars would have the same probability of having redder or bluer $m_{F343N} - m_{F435W}$ and $m_{F555W} - m_{F814W}$ colors than the bulk of MSTO stars. On the contrary, the presence of distinct sequences demonstrates that the extreme red $m_{F275W} - m_{F438W}$ colors of the selected stars are intrinsic. We note that the Be stars, which are commonly observed in Magellanic Cloud clusters younger than ~300 Myr (Keller et al. 2000; Bastian et al. 2017; Correnti et al. 2017; Milone et al. 2018), also exhibit redder colors than the bulk of eMSTO stars in CMDs composed of $F275W$ and $F336W$ filters.

In the following, we explore the possibility that the extreme $F275W$–$F438W$ colors of UV-dim stars are an effect connected to the stellar rotation. It is well known that stellar rotation diminishes the effective temperature and the luminosity of a star, with fast-rotating MSTO stars being redder and dimmer than slow rotators. The position of a star along the eMSTO depends on the effects of limb and gravity darkening and on the viewing angle of the stellar rotation axes with respect to the line of sight. In this context, UV-dim stars would comprise fast rotators that are seen equator-on since these stars appear colder and fainter than pole-on fast rotators.

To qualitatively explore this suggestion, we produced simulations based on the isochrones from the Geneva database

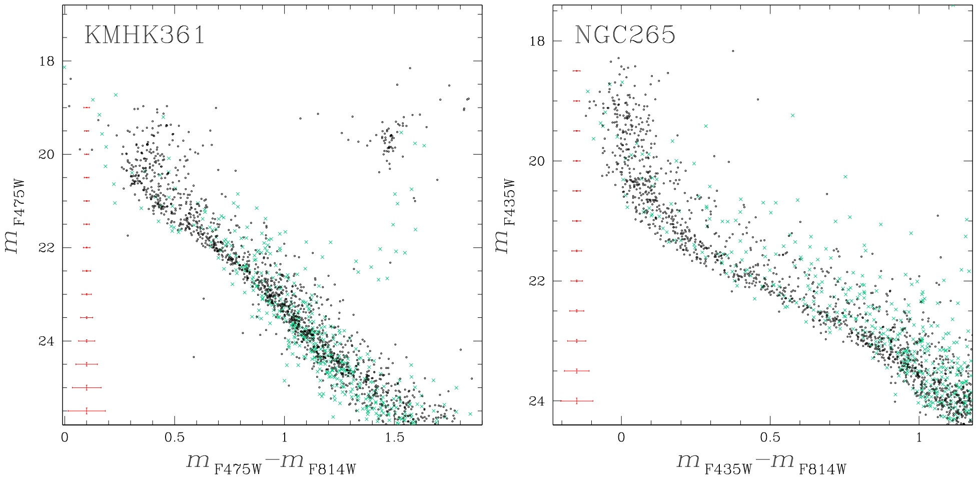

Fig. 12. CMDs of the clusters KMHK 361 and NGC 265 without previous evidence of eMSTOs. Stars in the cluster field and reference field of each cluster are represented with black points and aqua crosses, respectively. See text for details.

(Mowlavi et al. 2012; Ekström et al. 2012, 2013; Georgy et al. 2014) in close analogy with what we did in Sect. 6.2. In the top panels of Fig. 18 we simulated a population of nonrotating stars (aqua points), which includes the 33% of the total number of stars, and a population of fast rotators, where the stellar rotation corresponds to 0.9 times the breakout value ($\omega/\omega_c = 0.9$, black points). The simulated fraction of binaries is 0.3 and is similar to the observed binary fractions of intermediate-age LMC star clusters (Milone et al. 2009).

We note that nonrotating stars are located on the red and faint side of the eMSTO in the m_{F438W} versus $m_{F275W} - m_{F438W}$ and m_{F435W} versus $m_{F343N} - m_{F435W}$ CMDs, similarly to the clouds of UV-dim stars observed in the corresponding diagrams of NGC 1783. However, these stars define a narrow sequence that overlaps with the red portion of the eMSTO, in contrast with what is observed in the cloud of stars of NGC 1783 where we observe a broad color distribution that extends toward the red of the bulk of eMSTO stars. In addition, simulated stars exhibit fainter m_{F555W} magnitudes and redder $m_{F555W} - m_{F814W}$ colors than the bulk of eMSTO, in disagreement with what is observed in the m_{F555W} versus $m_{F555W} - m_{F814W}$ CMD. Hence, we conclude that the cloud of stars in NGC 1783 is not consistent with a population of nonrotating stars.

In the bottom panels of Fig. 18 we limit the analysis to fast-rotating stars only, where the position of a star in the eMSTO strongly depends on the limb and gravity darkening and on the viewing angle. We select by hand a sample of eMSTO stars with red $m_{F275W} - m_{F438W}$ colors and faint m_{F438W} magnitudes (red points in Fig. 18). Clearly, the hypothesis that stars with a certain range of viewing angle correspond to the cloud of NGC 1783 stars is challenged by the position of the selected stars in the optical CMD, where they define a narrow sequence in the middle of the eMSTO. Further, it seems unlikely that the spread of the turnoff can be entirely attributed to the viewing angle of stars rotating close to breakout value ~2 Gyr after their formation.

As an alternative, circumstellar disks could be responsible for absorbing the UV radiation and the consequent cloud of stars on the red side of the eMSTO. Debris disks, possibly associated with planet formation, are frequently observed around A-type stars (e.g., Eiroa et al. 2013, and references therein). A challenge is the location of UV-dim stars in the m_{F555W} versus $m_{F555W} - m_{F814W}$ CMD, which would imply that their disks poorly affect the emergent optical radiation. On the contrary, dust absorption is strongly dependent on the wavelength and is much more significant in the UV than in the optical. Hence, circumstellar dust in a disk could explain the location of these stars in the CMD (D'Antona et al., in prep.).

In this scenario, the disks are associated with stars that are currently nonrotating so that they can distribute along a narrow sequence in the optical CMD. If the disk formation is associated with rotation, these stars should have experienced fast rotation in their lifetime.

6.4. A zigzag across the MS of NGC 1783

A visual inspection of the CMD of Fig. 16 shows another intriguing detail of the CMD of NGC 1783. As highlighted by the Hess diagram in the inset, the upper MS runs in a zigzag, with two main discontinuities ($m_{F438W} \sim 22.0$ and 22.4) and various sudden changes of slope around $m_{F438W} = 21.9, 22.1, 22.3$ and 22.5.

We compare in Fig. 19 the observed upper MS of NGC 1783 with the isochrones from Padova (left, Marigo et al. 2017). The faint MS discontinuity corresponds to effective temperature $T_{\rm eff} = 6900$ K and mass $\mathcal{M} = 1.26\,M_{\odot}$, whereas stars on the bright MS discontinuity have $T_{\rm eff} = 7250$ K and $\mathcal{M} = 1.19\,M_{\odot}$.

We tentatively associate the hotter gap of the NGC 1783 MS with the original Böhm-Vitense gap. A gap along the MS at $T_{\rm eff} \sim 7500$ K has been first predicted by Böhm-Vitense (1970) and observed in the nearest Galactic open clusters (e.g., Bohm-Vitense & Canterna 1974; de Bruijne et al. 2000, 2001). The Böhm-Vitense gap is associated with sudden changes in the structure of convective atmospheres. It has been interpreted as a color effect, due to the fact that the temperature gradient in deep atmospheric layers becomes smaller than the radiative gradient. As an alternative, it is the effect of temperature inhomogeneities produced by photospheric granulation (e.g., Boehm-Vitense 1982).

The colder discontinuity of the NGC 1783 MSs could correspond to a distinct MS gap, which was earlier investigated by D'Antona et al. (2002). Indeed, fainter MS gaps have been observed around $T_{\rm eff} \sim 7000$ K (e.g., Rachford & Canterna 2000). At this temperature, convection begins in stellar envelopes, and an increasing amount of the stellar exterior becomes convective as the mass and effective temperature decrease. Also, the eMSTO disappears below ~7000 K, confirming that fast-rotating MS stars are only present at hotter temperatures. Indeed, the external turbulence brakes the envelope rotation. Clearly, the change of stellar structure results in a variation of the MS slope. Recent works provide evidence of an MS kink at similar temperatures in several Galactic and Magellanic

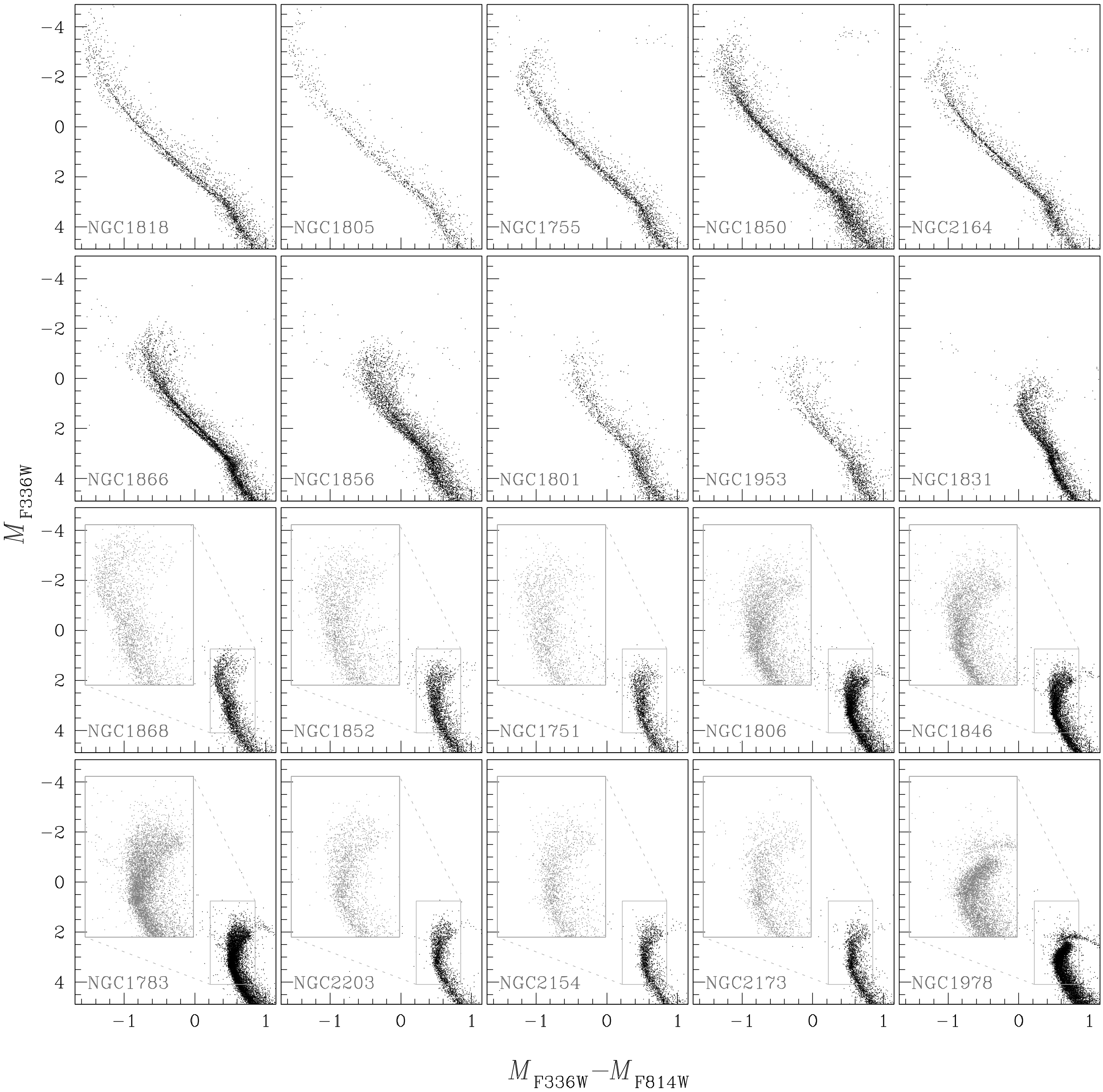

Fig. 13. Collection of M_{F336W} vs. $M_{F336W} - M_{F814W}$ CMDs of LMC clusters younger than 2.5 Gyr. All panels have the same scale and are zoomed around the MS, while the insets highlight the MSTO. Clusters are sorted by age.

Cloud clusters, where the split MS, which is associated with stellar populations with different rotation rates, merges into a single MS (e.g., D'Antona et al. 2017; Milone et al. 2018; Marino et al. 2018a; Goudfrooij et al. 2018).

The fainter MS gap has been investigated in the Hyades by D'Antona et al. (2002) based on the full spectrum of turbulence model by Canuto et al. (1996), which predicts that the depth of the convective envelope suddenly changes within a narrow range of stellar mass and around $T_{\rm eff} \sim 6800$ K. They concluded that the gap is an effective-temperature effect associated with the sharp effective-temperature difference between stars that are only convective in the surface layers and stars with well-developed convective interiors.

However, these results are based on poorly populated CMDs of open clusters, which often make it challenging to assess the statistical significance of the gaps. The high-precision HST photometry of populous star clusters may overcome this limitation and provides new insights on the MS region in the temperature range between ~6500 K and 7500 K.

As shown in Fig. 19, neither the isochrones from the Padova group nor those from the BaSTI (middle, Pietrinferni et al. 2004) and MESA (Choi et al. 2016; Dotter 2016; Paxton et al. 2011) databases reproduce the observed MS discontinuities. This fact corroborates the conclusion that these stellar models poorly reproduce the CMD region where the stellar atmosphere changes from radiative to convective.

6.5. Search for multiple generations in NGC 1783

In the past few years, astronomers have dedicated huge efforts to searching for young star clusters that are analogous to old GCs. Indeed, they may provide a snapshot of multiple

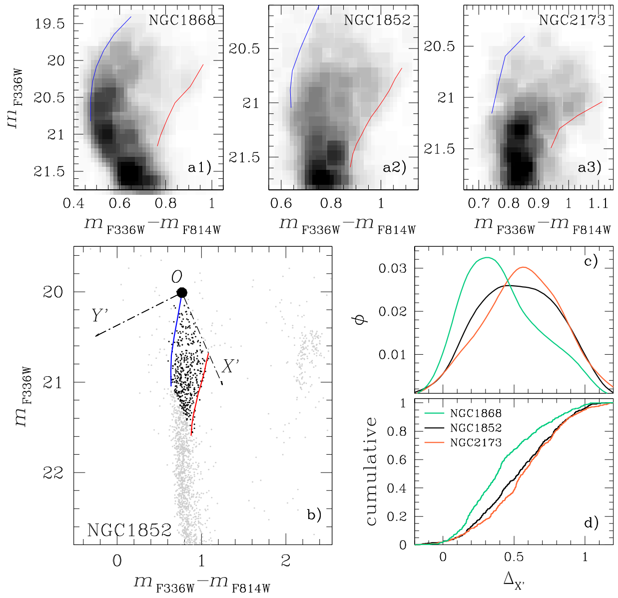

Fig. 14. m_{F336W} vs. $m_{F336W} - m_{F814W}$ Hess diagrams of NGC 1868 (*a1*), NGC 1852 (*a2*), and NGC 2173 (*a3*) zoomed around the eMSTO. The blue and red lines are the boundaries of the eMSTOs. *Panel b* illustrates the scheme to derive the $\Delta_{X'}$ quantity for eMSTO stars, while the corresponding kernel-density distributions and cumulative distributions are plotted in *panels c and d*, respectively, for NGC 1868 (aqua), NGC 1852 (black) and NGC 2173 (orange). See the text for details.

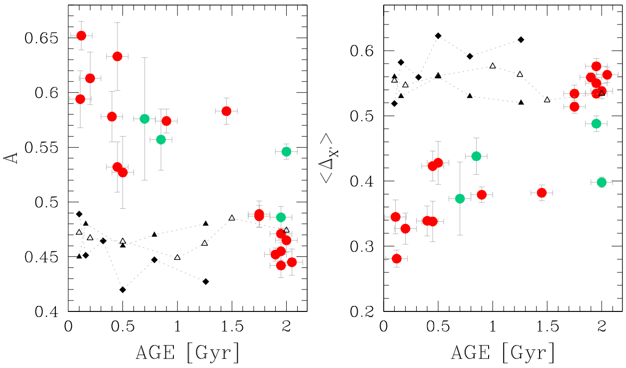

Fig. 15. Area below the $\Delta_{X'}$ cumulative curve, A, (*left*) and median $\Delta_{X'}$ value as a function of cluster age for LMC (red dots) and SMC (aqua dots) clusters with the eMSTO. Open and filled triangles are inferred from simulated CMDs of nonrotating stellar populations with different ages derived from the Padova and Geneva database, respectively. The diamonds correspond to coeval stellar populations with different rotation rates from the Geneva database. See text for details.

populations shortly after their formation. The two sequences of stars in the field of view of the ~1.5 Gyr old cluster NGC 1783 are a hotly debated case because they are consistent with younger stellar populations of ~440 and 520 Myr. After statistically subtracting the contribution of field stars from the CMD of stars around NGC 1783, Li et al. (2016) concluded that the blue MSs are cluster members. They suggested that these young stars are the signature of burst-like star formation and that NGC 1783 has experienced multiple bursts of star formation with an age difference of a few hundred million years. In this scenario, NGC 1783 is eventually the young counterpart of GCs with multiple populations.

This result has been challenged by Cabrera-Ziri et al. (2016), who suggested that the background subtraction method adopted by Li and collaborators may not remove contaminating field stars. Hence, they concluded that there is no evidence for multiple generations within NGC 1783 and that the young populations are field LMC stars along the same line of sight of NGC 1783.

As anticipated in Sect. 6.3, the m_{F438W} versus $m_{F438W} - m_{F814W}$ CMD plotted in Fig. 16 clearly reveals the stellar sequence first investigated by Li et al. (2016), whereas stellar proper motions allow the bulk of cluster members and field stars to be disentangled. To investigate whether NGC 1783 hosts a population of bright and hot MS stars, we combined information from photometry and stellar proper motions as illustrated in Fig. 20. We first used the dashed rectangle plotted in the top-left panel of Fig. 20 to select a sample of stars on the blue side of the cluster MSTO in the m_{F438W} versus $m_{F438W} - m_{F814W}$ CMD.

In the top-right panels, we compare the CMDs for stars in the dashed-line rectangle located within and outside a radius equal to 45 arcsec from the cluster's center. The external region has a ~four-time wider area than the internal one.

The proper-motion diagram plotted in the bottom-left panel of Fig. 20 shows that NGC 1783 stars are partially separated from LMC stars. We draw the red circle to separate the bulk of cluster members from field stars and represent these stars with black circles and aqua-starred symbols, respectively, in the bottom-left and in the top panels of Fig. 20.

We find that the sample of selected blue stars in the CMD comprises 18 field stars in the internal region, while 64 field stars belong to the external region. Their ratio of about four is comparable with the ratio of the corresponding field-of-view areas as expected if field stars have uniform spatial distribution. On the contrary, the number of stars with cluster-like proper motion in the internal and external field are 53 and 64 and are comparable with each other thus indicating that they unlikely belong to the LMC field population.

Noticeably, the distribution of stars in the proper-motion diagram (i.e., the stellar abscissas and ordinates and their density) is well reproduced by a function composed of the sum of two 3D Gaussian functions, which we derived by means of least squares minimization. For illustration purposes, we show in Fig. 20 the histogram distributions of $\mu_\alpha \cos\delta$ and μ_δ together with the corresponding 2D Gaussian functions.

Clearly, the stars with cluster-like proper motions selected in the bottom-left panel of Fig. 20 may also include field stars. To estimate the fraction of field stars that contaminate the sample of probable cluster members we used the best-fitting 3D Gaussian functions to simulate the proper motions plotted on the bottom-right panel of Fig. 20. Here, we show a subsample of 198 simulated stars, which is the same number of observed stars. Simulated field stars are represented with starred symbols and cluster stars with small dots. Clearly, a fraction of field stars (red starred symbols) have cluster-like proper motions while some cluster members (blue dots) lie outside the red circle. In particular, the fraction of field stars within the red circle, with respect to the number of cluster members is ~5%. These facts demonstrate that the majority (~95%) of stars with cluster-like proper motions selected in Fig. 20 are cluster members.

In summary, our proper-motion-based results confirm the conclusion of Li and collaborators that the blue sequences are composed of genuine members of NGC 1783. More sophisticated analysis is mandatory to understand whether the blue sequence is associated with young stellar populations as suggested by Li and collaborators or whether it is composed of blue stragglers. The cluster members on the bright and blue side of the red clump are consistent both with young red

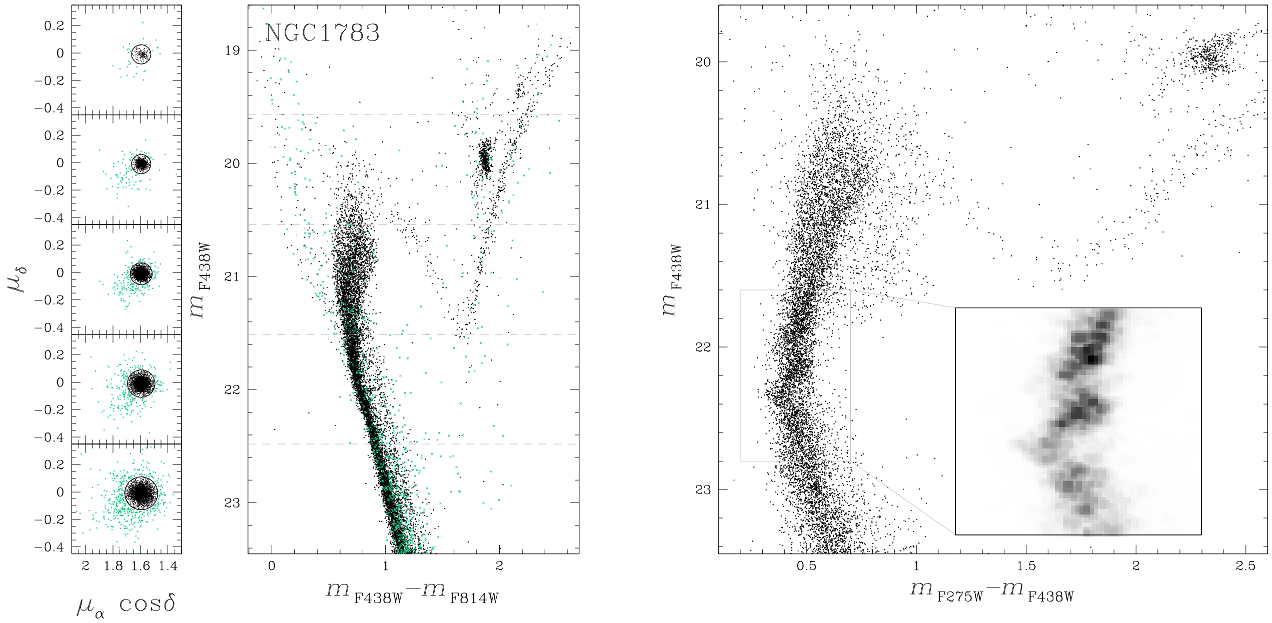

Fig. 16. Proper-motion diagrams of stars in the field of view of NGC 1783 in five $F438W$ magnitude intervals (*left*). The m_{F438W} vs. $m_{F438W}-m_{F814W}$ CMD for stars in the left panels is plotted on the *middle*. Stars within the black circles plotted in the proper-motion diagrams are considered probable cluster members and are colored black, whereas field stars are represented with aqua crosses. The *right panel* shows the m_{F438W} vs. $m_{F275W}-m_{F438W}$ CMD for probable cluster members, while the inset represents the Hess diagram of the CMD region around the upper MS.

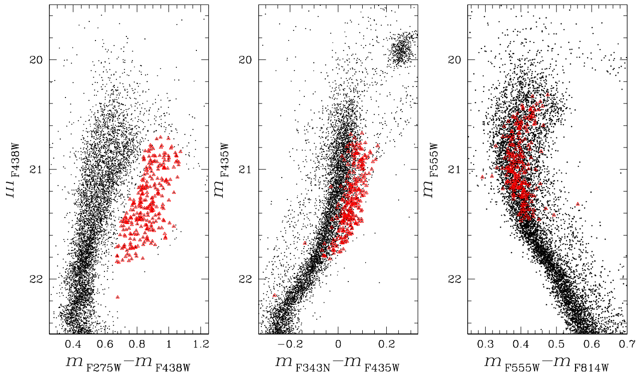

Fig. 17. m_{F438W} vs. $m_{F275W}-m_{F438W}$ (*left*), m_{F435W} vs. $m_{F343N}-m_{F435W}$ (*middle*), and m_{F555W} vs. $m_{F555W}-m_{F814W}$ (*right*) CMDs of proper-motion selected NGC 1783 stars. Stars in the red tail of the eMSTO, selected from the left-panel CMD, are colored red.

clump stars and with binary systems composed of red-clump stars.

6.6. Relative proper motions of stellar populations in the LMC and the SMC

Figures 21 and 22 show the CMDs and the proper-motion diagrams of stars in the fields of view of five SMC clusters, namely Kron 34, NGC 294, NGC 339, NGC 416, and NGC 419, and three LMC clusters, namely NGC 1755, NGC 1801, and NGC 1953. Since we focus on the internal kinematics of LMC and SMC stars, we restrict the analysis to the magnitude interval that provides the most precise proper-motion determinations. The stellar concentrations around the center of each diagram are composed of cluster members, and their broadening is mostly due to observational uncertainties. Indeed, the star-to-star scatter associated with the internal motions of cluster members is negligible with respect to proper motion errors at the distance of the Magellanic Clouds. On the contrary, field stars exhibit broad proper-motion distributions, which are significantly wider than what is expected from observational uncertainties alone.

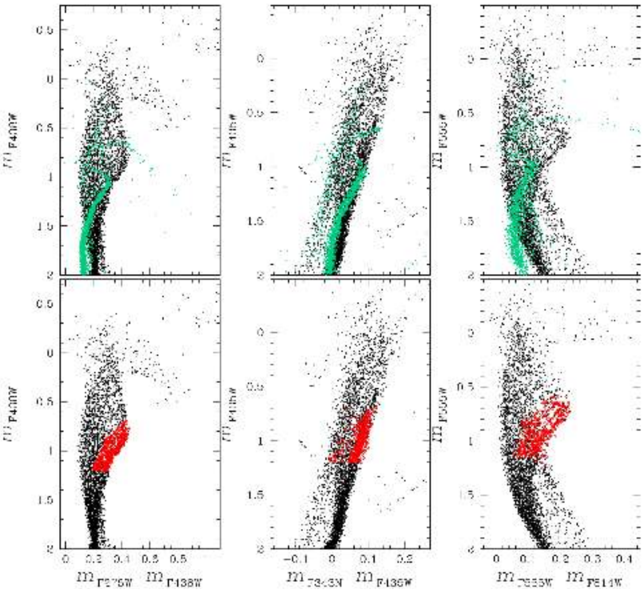

Fig. 18. Simulated CMDs of two stellar populations of fast-rotating stars ($\omega/\omega_{\rm c}$ = 0.9, black points) and nonrotating stars (aqua points). Red points in the *bottom-panel* diagrams mark the sample of fast rotating stars selected by hand and located on the red side of the eMSTO in the m_{F438W} vs. $m_{F275W}-m_{F438W}$ CMD. Simulations are derived from Geneva isochrones.

We identified in each CMD a group of stars with blue $m_{F336W}-m_{F814W}$ colors, which mostly comprise the young stellar populations of the host galaxy, and a group of old stars with red colors. Furthermore, we selected a sample of very-young

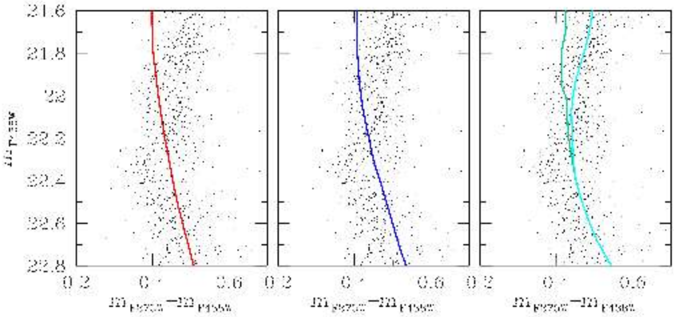

Fig. 19. Reproductions of the m_{F438W} vs. $m_{F275W} - m_{F438W}$ CMD of Fig. 16 zoomed around the upper MS. The red, blue, and green lines superimposed on each CMD are the best-fitting nonrotating isochrones from the Padova (*left*), BaSTI (*middle*), and MESA (*right*) databases. A rotating MESA isochrone with $\omega = 0.4\omega_c$, with ω_c being the breakout velocity, is plotted in the right panel in cyan.

LMC stars in NGC 1801 and NGC 1953 that define the bluest and brightest MS in their CMD (aqua triangles). The selected groups of old and young stars, identified in the CMDs, are highlighted with red and blue symbols, respectively, in the proper-motion diagrams plotted in the third and fourth columns of panels. A visual inspection of these figures suggests that the proper motions of young and old SMC stars typically show different ellipticities, whereas the differences are less pronounced for LMC stellar populations.

Results are illustrated in Fig. 23 and summarized in Table B.5, where we provide for each population the median proper motions relative to the main cluster in the field, the ellipticity of the best-fitting ellipse that encloses 90% of stars ($\epsilon = 1 - b/a$, where a and b are the minor and major axes of the ellipse), and the position angle θ. As shown in Fig. 21, young SMC stars exhibit flat proper-motion distributions, where the eccentricity of the best-fitting ellipses ranges from $\epsilon \sim 0.3$ in NGC 416 to $\epsilon \sim 0.6$ in NGC 339. The proper-motion distributions of the old stellar populations have smaller eccentricity values, between $\epsilon \sim 0.1$ in NGC 416 and NGC 339 and $\epsilon \sim 0.3$ in NGC 419. In all cases, the major axis of the best-fitting ellipses roughly follows the direction northwest-southeast, thus pointing toward the LMC. Similar conclusions are derived by Massari et al. (2021) based on high-precision proper motions and stellar photometry from HST of NGC 419. These authors demonstrated that it is possible to separate cluster members from SMC field stars by using stellar kinematics. Moreover, they identified a kinematic stellar component that they associated with the Magellanic Bridge. Although our results do not provide evidence for populations of field stars with distinct kinematics, the flattened proper-motion distributions would reflect the flow motion of stars from the SMC to the LMC. Further evidence of SMC star clusters showing a relative motion pointing toward the LMC is provided by Zivick et al. (2018), Piatti (2021), Dias et al. (2021), and Schmidt et al. (2022).

Young LMC stars exhibit flatter proper-motion distributions than old LMC stars, in close analogy with what is observed for the SMC. However, the ellipses that best fit the proper motions of LMC stars in the fields of NGC 1755, and NGC 1953 have different orientations than the corresponding ellipses inferred for stars in the direction of NGC 1801. Very young stars in the field of view of NGC 1953 have more clustered proper motions with respect to the remaining young stars. Interestingly, the selected young stars show some hints of split MS in the CMD. A spectroscopic investigation is mandatory to understand whether the split is due to stellar populations with different rotation rates, similar to what is observed in the star clusters with similar ages, or to differences in distance, age, and/or chemical composition. The proper-motion distributions of stars in the direction of the three analyzed LMC clusters are nearly circular, in contrast with what is observed for young stars in both Magellanic Cloud clusters and old SMC stars.

6.7. The massive star-forming region NGC 346

NGC 346 is a very young SMC star cluster (age ~ 3 Myr, Bouret et al. 2003; Sabbi et al. 2007) that is responsible for the excitation of the surrounding HII region N 66. A stacked $F814W$ image of NGC 346 and its neighborhoods is shown in the left panel of Fig. 24 where we mark with an azure circle the central part of the NGC 346 star-forming region.

The intermediate-age star cluster BS 90 is also visible to the north of NGC 346 and is highlighted by the red circle in the left panel of Fig. 24. The proper-motion diagram of all stars with m_{F814W} between 18.4 and 21.4 mag is plotted in the middle panel of Fig. 24 and comprises stars with the best proper-motion quality[5]. Stars within the regions centered on NGC 346 and BS 90 (azure and red points, respectively) define two distinct clumps in the proper-motion diagram, which are mostly composed of cluster members. We selected probable cluster members with proper motions smaller than four times the rms of the proper-motion distributions (stars within the circles) and calculated the median values of $\mu_\alpha \cos\delta$ and μ_δ. Results are listed in Table B.6. The fact that NGC 346 and BS 90 exhibit different proper motions demonstrates that they are distinct clusters projected onto the same field of view.

The probable members of NGC 346 and BS 90, selected from both stellar proper motions and positions, are marked with azure and red points in the CMD in the right panel of Fig. 24. The sample of selected NGC 346 stars defines a well-populated MS and upper pre-MS, whose large broadening is indicative of a significant amount of differential reddening. On the contrary, BS 90 exhibits narrow SGB and RGB sequences, and a well-defined red clump, thus confirming that this cluster is poorly affected by differential reddening (Sabbi et al. 2007). Specifically, the average reddening variation in the field of view within 36 arcsec from the center of BS 90 never exceeds $\Delta E(B-V) = 0.013$ mag, with ~68% of the stars having $\Delta E(B-V)$ values within 0.004 mag from the average reddening. This fact demonstrates that this cluster is in the foreground with respect to the region of NGC 346 and N 66.

The CMD of stars in the field of view of NGC 346 comprises stars in different evolutionary stages for which high-precision

---

[5] Specifically, the selected stars pass the criteria of selection based on the $RADXS$ and $qfit$ parameters discussed in Sect. 2.4 and that are not saturated in the long-exposure $F555W$ and $F814W$ images (see Table B.4 for details on the data set). Moreover, we only included stars with small proper-motion errors, when compared to the bulk of stars with similar magnitudes. To select them, we first plotted the proper-motion uncertainty against the $F814W$ magnitude. Then, we divided the magnitude interval into various 0.25 mag bins and calculated the median proper-motion uncertainty for each bin. We computed the absolute values of the difference between the uncertainty of each star and the median value and estimated the 68.27th percentile of the corresponding distribution (σ). We added three times σ to the median uncertainty of each bin and associated this value with the median magnitude of the stars in the bin. Finally, these points are linearly interpolated and the stars that are located below this line in the proper-motion uncertainty vs. magnitude plane are considered as well measured.

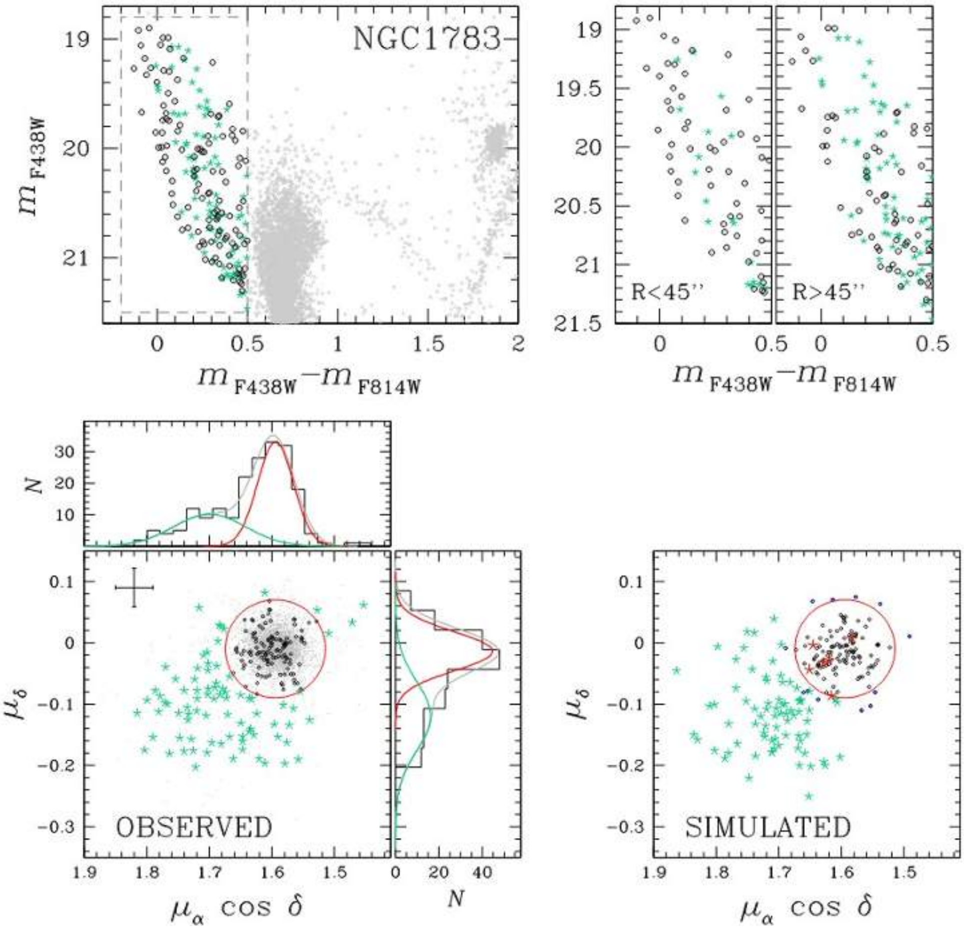

Fig. 20. Procedure to identify the probable stars of NGC 1783 on the blue, bright side of the MS. *Top*: reproductions of the CMDs of NGC 1783 of Fig. 16. Right panels are zoomed-in views of the CMD region on the bright-blue side of the MSTO (dashed rectangle in the top-left panel) for stars with radial distances from the cluster center smaller and larger than 45 arcsec. *Bottom*: proper-motion diagram of stars plotted in the top-left panel (left). The red circle separates stars with a cluster-like motion from the bulk of field stars. Black points and aqua-starred symbols mark the selected bright-blue stars. The corresponding histogram distributions for $\mu_\alpha \cos\delta$ and μ_δ are also represented on the top and right side of the panel. The best fit bi-Gaussian functions are represented with gray lines, and the two Gaussian components are colored aqua and red. The bottom-right panel shows the simulated proper motions for cluster members and field stars. Black and blue dots indicate NGC 1783 stars with cluster-like and field-like proper motions, respectively, while red color is used to distinguish field stars with cluster-like proper motions from the remaining field stars (aqua starred symbols).

proper motions are available, including pre-MS stars, MS stars, and evolved stars in the SGB, RGB, and red-clump phases. As widely discussed in literature works (e.g., Sabbi et al. 2007; Cignoni et al. 2010, 2011), this field hosts a conspicuous population of pre-MS stars, which are highlighted in the top-left panel of Fig. 25, namely two samples of pre-MS I and pre-MS II stars with high-precision proper motions, which lie respectively inside and outside the central region of NGC 346. As indicated in Table B.6, the proper-motion distributions of the two groups of pre-MS stars share the same mean motion as NGC 346, indicating that stars in both the central region and in the outskirts share the same mean motions (top-middle panel of Fig. 25), although the latter exhibits a wider proper-motion dispersion. The distribution of pre-MS stars across the field of view highlights the distinctive structure of the NGC 346 region described by Contursi et al. (2000), including the low-density filament oriented to the northeast direction (spur), and the fan-shaped structure (bar), which hosts the majority of pre-MS stars.

MS stars are investigated in the middle panels of Fig. 25, and comprise stars of the young population of the SMC. The proper-motion diagram reveals that the bulk of MS stars (hereafter MS I stars, aqua points) exhibit a proper-motion distribution similar to the NGC 346 pre-MS stars. In addition, we note a tail of stars in the proper-motion diagram that points toward the LMC and that we colored blue and name MS II. Both groups of selected MS stars seem diffused over the whole field, but the MS I stars define some stellar overdensities that trace the bar and possibly, some clumps of the Spur. We suggest that the MS II is mostly composed on SMC field stars that follow an elliptical proper-motion distribution, in close analogy with what is observed for the other analyzed SMC young stars. On the contrary, MS I stars comprise both field SMC stars and stars of the NGC 346 region.

Finally, the old SMC field stars are investigated in the bottom panels of Fig. 25. Although this stellar population hosts some stars up to ages of more than 10 Gyr, it is mostly associated with a major star-formation episode that occurred between ~3 and 5 Gyr ago. The RGB stars of the old populations with radial distance smaller than 36 arcsec from the center of BS 90 are marked with red points. These stars exhibit similar proper-motion distribution as young stars and pre-MS stars in the star-forming region of BS 90 (bottom-middle panel) and are uniformly distributed across the entire field of view (bottom-right panel of Fig. 25). We note that the motion of the bulk of old SMC field stars is significantly different from that of BS 90 despite this cluster having an age similar to most old field stars.

7. Summary and conclusions

We have used the HST archive to retrieve ACS/WFC, UVIS/WFC3, and NIR/WFC3 images of 101 fields in the direction of the LMC and the SMC. These images include 29 SMC clusters and 84 LMC clusters. We derived high-precision photometry and astrometry by using the methods and the computer programs developed by Jay Anderson and his collaborators and obtained high-resolution reddening maps in the direction of each cluster. We accurately determined cluster centers and estimated distance modulus, reddening, metallicity, and age by comparing the CMDs with Padova isochrones (Marigo et al. 2017). Moreover, we calculated proper motions for cluster and field stars in 12 stellar fields that have multi-epoch observations.

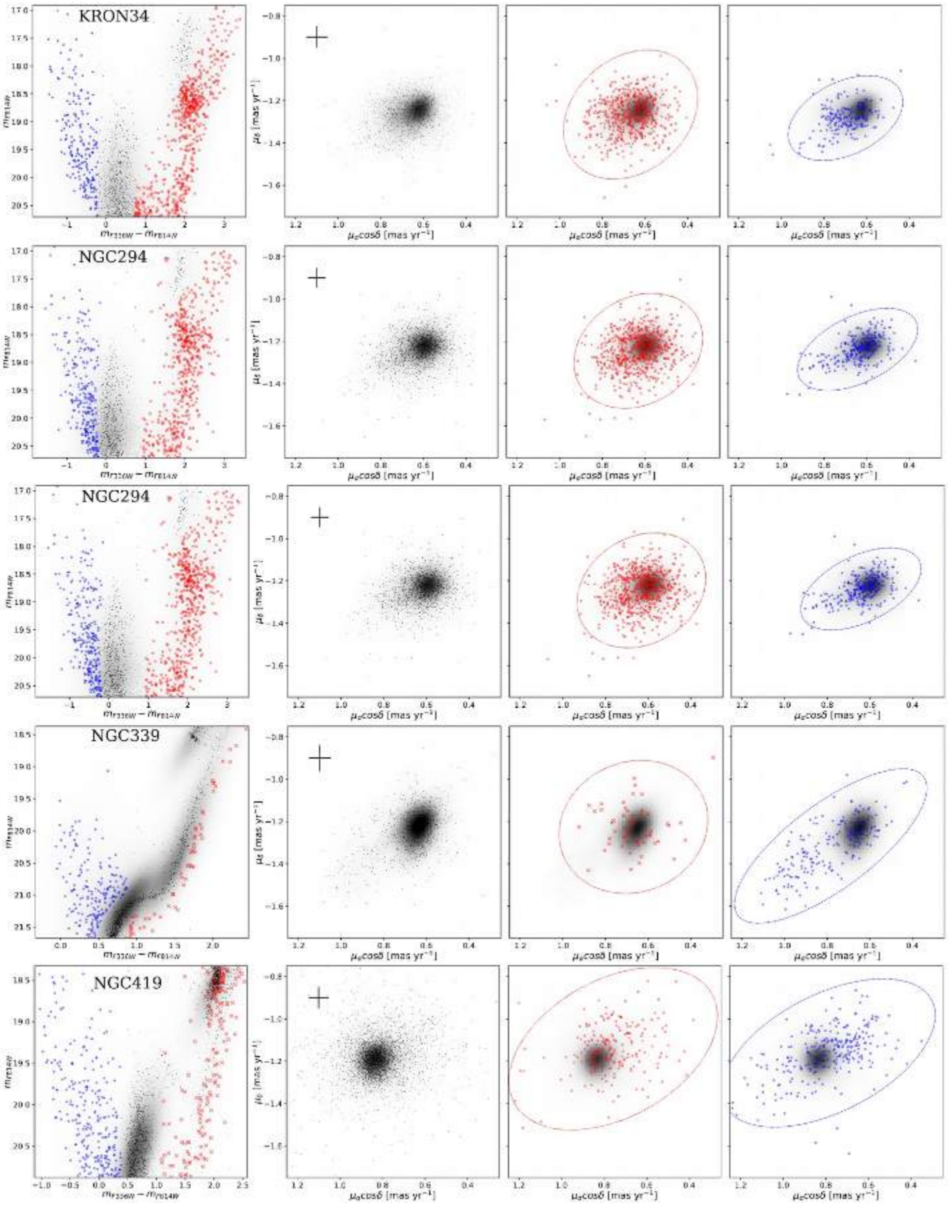

Fig. 21. Photometry and proper motions of stars in the field of view of five SMC clusters with available proper motions. The *first-column panels* show the CMDs while the corresponding proper-motion diagrams are plotted in the *second column*. The *third and fourth columns* represent the proper motions of candidate old and young field stars selected in the CMDs and colored red and blue, respectively. Red and blue ellipses provide the best-fitting of the distributions of candidate old and young field stars in the proper motion diagram. The Hess diagrams of the proper-motion distributions are shown in all proper-motion diagrams.

The exquisite photometry, astrometry, and proper motions presented in this paper have the potential to shed light on a variety of astrophysical phenomena. As an example, we present here some results that are evident from a visual inspection of the CMDs and the proper-motion diagrams.

- New insights into the eMSTO phenomenon. The photometric catalogs, derived from homogeneous data reduction, allow an accurate comparison of clusters with different ages. The analysis of the m_{F336W} versus $m_{F336W} - m_{F814W}$ CMDs of 19 LMC clusters in a wide range of ages, between ~20 Myr and 2 Gyr, reveals that the distribution of stars along the eMSTO significantly changes from one cluster to another and depends on GC age. While the eMSTOs of young clusters are dominated by blue and bright eMSTO stars, the fraction of stars in the red and faint eMSTO increases in older clusters. This property of eMSTO stars provides a new observational constraint that helps us understand the physical mechanism that is responsible for the eMSTO.
  We also provide the first evidence of eMSTO in the LMC intermediate-age cluster KMHK 361 and in the SMC young star cluster NGC 265, where we also detect a split MS, with the blue MS hosting about one-third of the MS stars. This finding corroborates the conclusions that the eMSTO is a universal feature of the CMD of clusters younger than ~2 Gyr and that the split MS is a common phenomenon that occurs in clusters younger than ~1 Gyr.
- A new feature along the eMSTO. We find that about 7% of eMSTO stars in NGC 1783 exhibit redder $m_{F275W} - m_{F438W}$ and $m_{F343N} - m_{F438}W$ colors than the remaining eMSTO stars. They show a wide color broadening up to ~0.2 mag in the m_{F438W} versus $m_{F275W} - m_{F438W}$ CMD, but the color spread decreases to less than 0.1 mag in the m_{F435W} versus $m_{F343N} - m_{F435W}$ diagram. On the contrary, when observed in optical CMDs, these stars define a narrow sequence and have intermediate colors relative to the remaining eMSTO stars.
- Hunting for multiple star-formation bursts in intermediate-age star clusters. It has been suggested that the bright and blue stars of the CMD of NGC 1783 are cluster members and correspond to young stellar generations (Li et al. 2016).

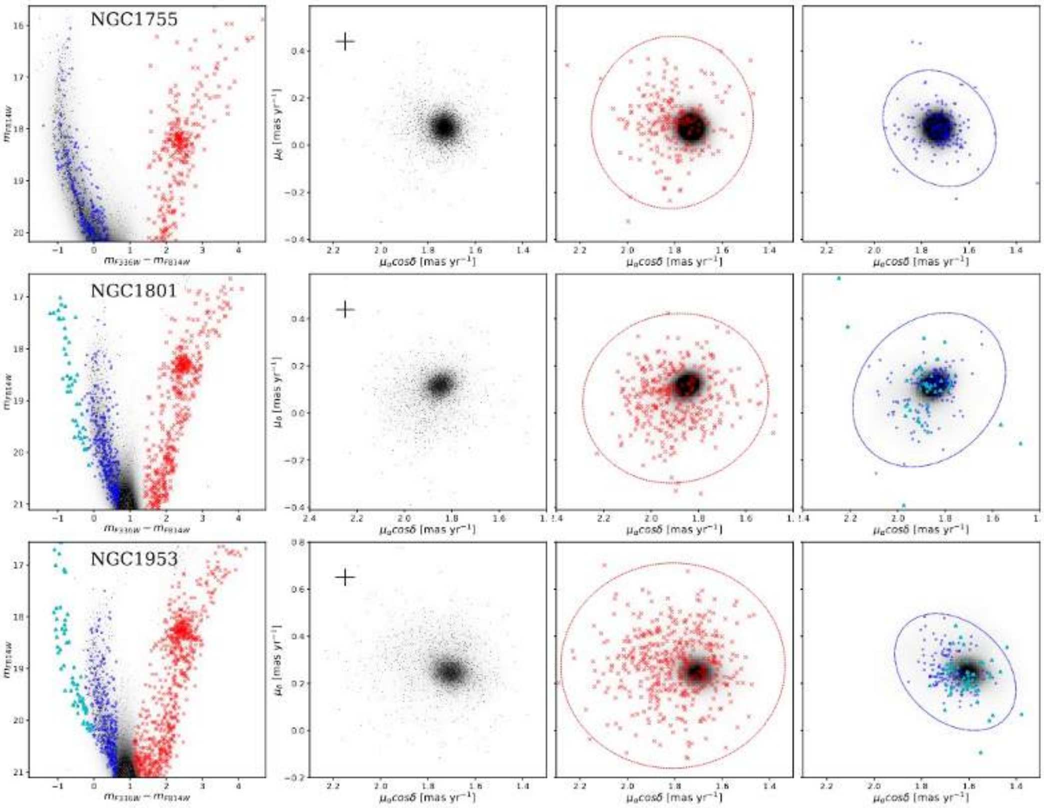

Fig. 22. Similar to Fig. 21 but for the LMC clusters NGC 1755, NGC 1801, and NGC 1953. Very young stars in the fields of view of NGC 1801 and NGC 1953 are represented with aqua triangles.

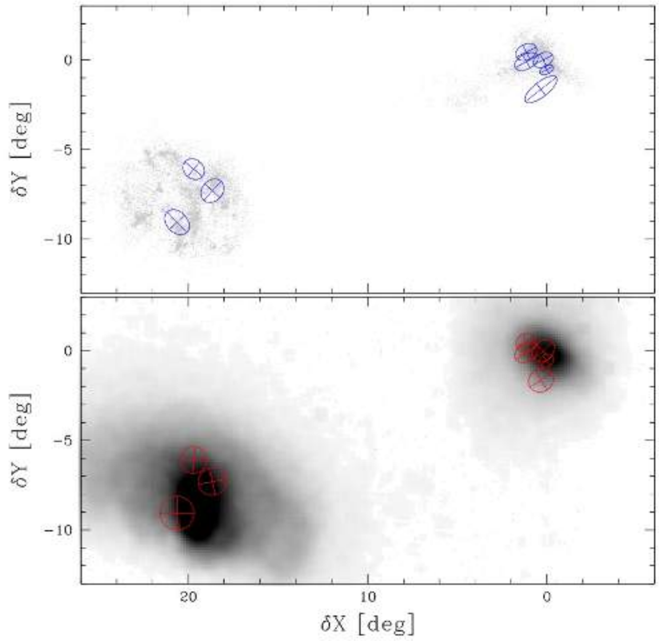

Fig. 23. Positions of candidate young LMC and SMC stars relative to the center of the SMC (*top*). The *bottom panel* shows the density distributions of candidate old LMC and SMC stars. The ellipses that provide the best fit of proper-motion distributions in young and old stars in the fields of eight clusters are colored blue and red, respectively.

This result, which would be a major step toward the understanding of multiple populations in GCs, has been challenged by Cabrera-Ziri et al. (2016), who suggested that the blue sequences are composed of field stars.

The catalogs of the present work include proper motions of stars in the field of view of NGC 1783, thus providing additional information on the origin of the blue sequences. In particular, we support the conclusion that most bright blue MS stars are consistent with being cluster members, thus excluding the possibility that the blue MSs are artifacts produced by a poor statistical subtraction of the field. Our results, based on proper motion analysis, do not allow us to infer whether the blue sequence is composed of MS stars of a young stellar generation or are the blue straggler sequences of NGC 1783.

In addition to disentangling cluster members and field stars, proper motions allow the investigation of the internal kinematics of stellar populations in the Magellanic Clouds. We have identified two groups of young and old Magellanic Cloud field stars in the fields of view of five SMC clusters, namely KRON 34, NGC 294, NGC 339, NGC 416, and NGC 419, and of three LMC clusters, NGC 1755, NGC 1801, and NGC 1953.

The proper motions of young SMC stars exhibit elliptical distributions with high ellipticity values and major axes that point toward the LMC. The flattened proper-motion distributions would be associated with the Magellanic bridge and represent the dynamic signature of the flow motion of stars from the SMC to the LMC. Our results corroborate the evidence that SMC stars are affected by the LMC (e.g., Piatti et al. 2015). Old and young SMC stars exhibit different kinematics. The proper motions of the old SMC stars are also oriented toward the LMC and have elliptical distributions but with lower values of ellipticity and, in most cases, different centers. The different proper-motion distributions of old and young stars could reflect, in part, the presence of different young and old bridges.

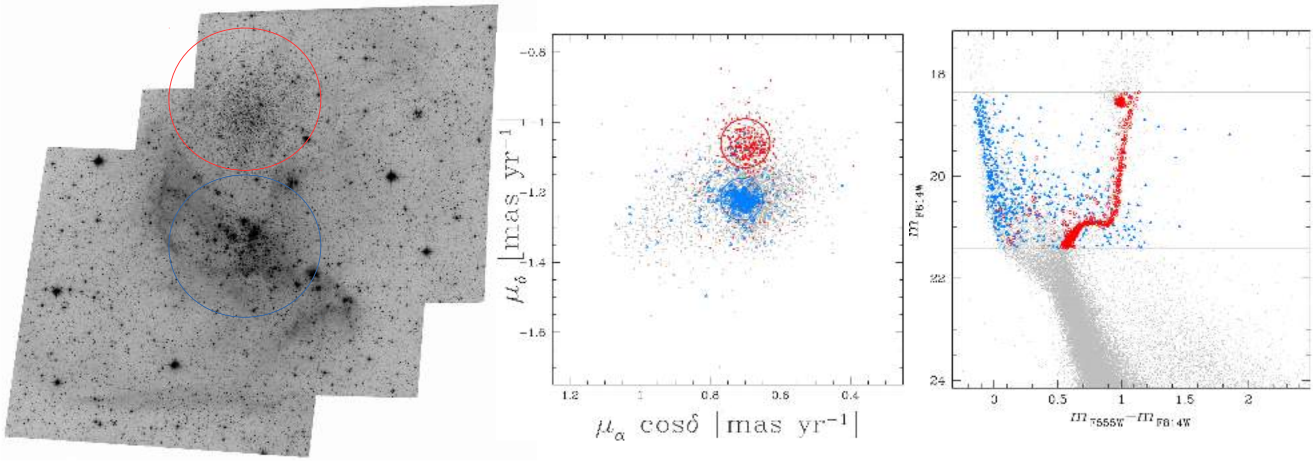

Fig. 24. Stacked $F814W$ WFC/ACS image of the SMC field that includes the clusters NGC 346 and BS 90, which are highlighted by the azure and red circle, respectively (*left*). The *middle panel* shows the proper-motion diagram, while the m_{F814W} vs. $m_{F555W} - m_{F814W}$ CMD is represented in the *right panel*. Only stars in the $F814W$ magnitude interval between the two horizontal lines in the CMD are plotted in the proper-motion diagram, where the stars in the NGC 346 and BS 90 regions defined in the left panel are colored blue and red, respectively. Blue and red symbols in the right-panel CMD mark proper-motion selected cluster members in the NGC 346 and BS 90 regions. See text for details.

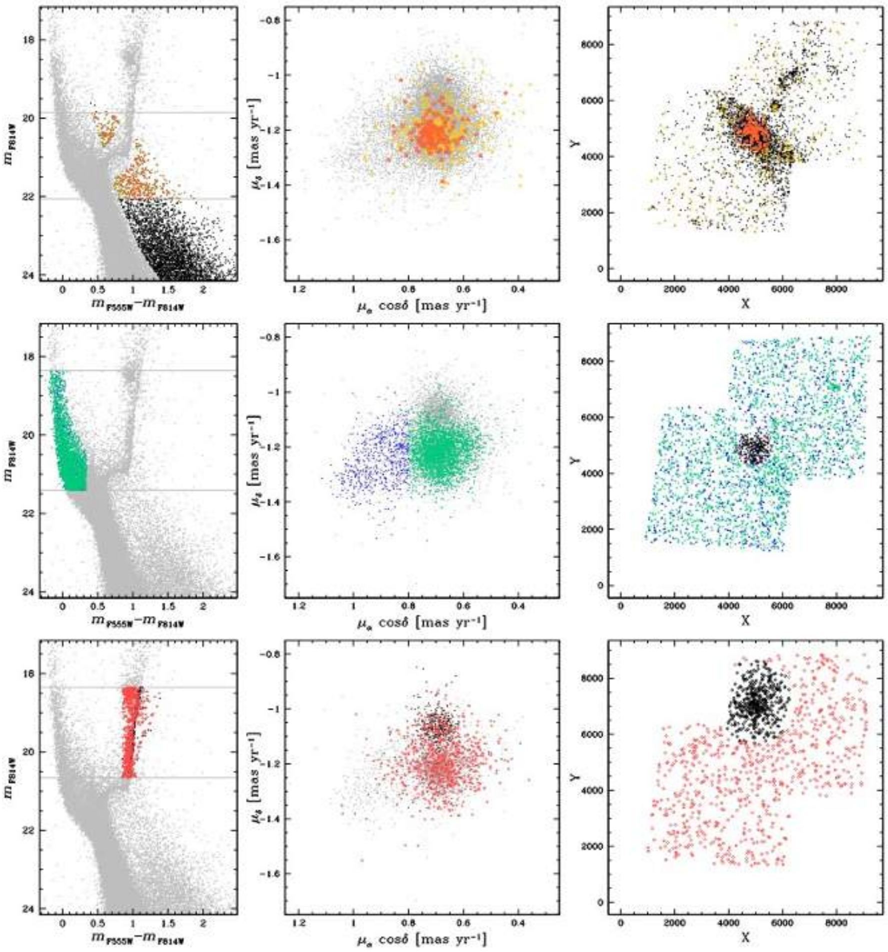

Fig. 25. Photometry, proper motions, and astrometry of the stellar populations in the field of view of NGC 346. The *three left panels* are reproductions of the m_{F814W} vs. $m_{F555W} - m_{F814W}$ CMDs for stars in the field of view of NGC 346 and are used to select various groups of stars that we represented with colored symbols. The *middle panels* show the proper motions for stars in the magnitude interval delimited by the horizontal lines in the corresponding CMDs, whereas the *right panels* show the coordinates of the selected stars. The *top panels* are focused on candidate pre-MS stars. Specifically, bright pre-MS within 28 arcsec from the center of NGC 346 (pre-MS I sample) are represented with orange symbols, the remaining bright pre-MS stars (pre-MS II sample) are colored yellow, while the black symbols in the top panels mark faint pre-MS stars. Bright MS stars are investigated in the middle panels. Blue and aqua colors mark MS I and MS II stars, which have radial distances larger than 28 arcsec from the center of NGC 346, but different proper-motion distributions. The remaining bright-MS stars are colored black. The *bottom panels* highlight the selected RGB stars with radial distances from the center of BS 90 larger (red) and smaller than 60 arcsec (black).

The young and the old LMC stars also exhibit different motions on the plane of the sky. While the proper motions of the old populations show nearly circular distributions, young LMC stars have more flattened proper-motion distributions, with different orientations of the best-fitting ellipses.

Acknowledgements. We thank the anonymous referee for various suggestions that improved the quality of the manuscript. This work has received funding from the European Research Council (ERC) under the European Union's Horizon 2020 research innovation programme (Grant Agreement ERC-StG 2016, No. 716082 'GALFOR', PI: Milone, `http://progetti.dfa.unipd.it/GALFOR`) and from the European Union's Horizon 2020 research and innovation programme under the Marie Sklodowska-Curie Grant Agreement No. 101034319 and from the European Union – NextGenerationEU, beneficiary: Ziliotto. A.P.M., M.T., and E.D. acknowledge support from MIUR through the FARE project R164RM93XW SEMPLICE (PI: Milone). A.P.M. and M.T. have been supported by MIUR under PRIN program 2017Z2HSMF (PI: Bedin). This research was supported in part by the Australian Research Council Centre of Excellence for All Sky Astrophysics in 3 Dimensions (ASTRO 3D) through project number CE170100013. This work is based on observations made with the NASA/ESA *Hubble* Space Telescope, obtained from the data archive at the Space Telescope Science Institute (STScI). STScI is operated by the Association of Universities for Research in Astronomy, Inc. under NASA contract NAS 5-26555.

References

Anderson, J., & Bedin, L. R. 2010, PASP, 122, 1035
Anderson, J., & King, I. R. 2000, PASP, 112, 1360
Anderson, J., & King, I. R. 2006, PSFs, Photometry, and Astronomy for the ACS/WFC, Instrument Science Report ACS 2006-01, 1
Anderson, J., Bedin, L. R., Piotto, G., Yadav, R. S., & Bellini, A. 2006, A&A, 454, 1029
Anderson, J., Sarajedini, A., Bedin, L. R., et al. 2008, AJ, 135, 2055
Bastian, N., & de Mink, S. E. 2009, MNRAS, 398, L11
Bastian, N., Cabrera-Ziri, I., Niederhofer, F., et al. 2017, MNRAS, 465, 4795
Bedin, L. R., King, I. R., Anderson, J., et al. 2008, ApJ, 678, 1279
Bellini, A., & Bedin, L. R. 2009, PASP, 121, 1419
Bellini, A., Anderson, J., & Bedin, L. R. 2011, PASP, 123, 622
Bellini, A., Piotto, G., Milone, A. P., et al. 2013, ApJ, 765, 32
Bellini, A., Anderson, J., Bedin, L. R., et al. 2017, ApJ, 842, 6
Bettinelli, M., Simioni, M., Aparicio, A., et al. 2016, MNRAS, 461, L67
Boehm-Vitense, E. 1982, ApJ, 255, 191
Bohlin, R. C. 2016, AJ, 152, 60
Böhm-Vitense, E. 1970, A&A, 8, 283
Bohm-Vitense, E., & Canterna, R. 1974, ApJ, 194, 629
Bouret, J. C., Lanz, T., Hillier, D. J., et al. 2003, ApJ, 595, 1182
Cabrera-Ziri, I., Niederhofer, F., Bastian, N., et al. 2016, MNRAS, 459, 4218
Caloi, V., & Cassatella, A. 1998, A&A, 330, 492
Canuto, V. M., Goldman, I., & Mazzitelli, I. 1996, ApJ, 473, 550
Castelli, F., & Kurucz, R. L. 2003, IAU Symp., 210, A20
Choi, J., Dotter, A., Conroy, C., et al. 2016, ApJ, 823, 102
Cignoni, M., Tosi, M., Sabbi, E., et al. 2010, ApJ, 712, L63
Cignoni, M., Tosi, M., Sabbi, E., Nota, A., & Gallagher, J. S. 2011, AJ, 141, 31
Claret, A. 2000, A&A, 363, 1081
Contursi, A., Lequeux, J., Cesarsky, D., et al. 2000, A&A, 362, 310
Cordoni, G., Milone, A. P., Marino, A. F., et al. 2018, ApJ, 869, 139
Cordoni, G., Milone, A. P., Marino, A. F., et al. 2020a, ApJ, 898, 147
Cordoni, G., Milone, A. P., Mastrobuono-Battisti, A., et al. 2020b, ApJ, 889, 18
Cordoni, G., Milone, A. P., Marino, A. F., et al. 2022, Nat. Commun., 13, 4325
Correnti, M., Goudfrooij, P., Bellini, A., Kalirai, J. S., & Puzia, T. H. 2017, MNRAS, 467, 3628
D'Antona, F., Montalbán, J., Kupka, F., & Heiter, U. 2002, ApJ, 564, L93
D'Antona, F., Di Criscienzo, M., Decressin, T., et al. 2015, MNRAS, 453, 2637
D'Antona, F., Milone, A. P., Tailo, M., et al. 2017, Nat. Astron., 1, 0186
de Bruijne, J. H. J., Hoogerwerf, R., & de Zeeuw, P. T. 2000, ApJ, 544, L65
de Bruijne, J. H. J., Hoogerwerf, R., & de Zeeuw, P. T. 2001, A&A, 367, 111
De Marchi, G., Panagia, N., & Milone, A. P. 2020, ApJ, 899, 114
Deustua, S. E., Bohlin, R. C., Mack, J., et al. 2017, WFC3 Chip Dependent Photometry with the UV Filters, Space Telescope WFC Instrument Science Report, 9
Dias, B., Angelo, M. S., Oliveira, R. A. P., et al. 2021, A&A, 647, L9
Dondoglio, E., Milone, A. P., Lagioia, E. P., et al. 2021, ApJ, 906, 76
Dotter, A. 2016, ApJS, 222, 8
Dotter, A., Sarajedini, A., Anderson, J., et al. 2010, ApJ, 708, 698
Dupree, A. K., Dotter, A., Johnson, C. I., et al. 2017, ApJ, 846, L1
Eiroa, C., Marshall, J. P., Mora, A., et al. 2013, A&A, 555, A11
Ekström, S., Georgy, C., Eggenberger, P., et al. 2012, A&A, 537, A146
Ekström, A., Baardsen, G., Forssén, C., et al. 2013, Phys. Rev. Lett., 110, 192502
Espinosa, Lara F., & Rieutord, M. 2011, A&A, 533, A43
Gaia Collaboration (Helmi, A., et al.) 2018, A&A, 616, A12
Gaia Collaboration (Brown, A. G. A., et al.) 2021, A&A, 649, A1
Gallart, C., Zoccali, M., Bertelli, G., et al. 2003, AJ, 125, 742
Georgy, C., Granada, A., Ekström, S., et al. 2014, A&A, 566, A21
Gilliland, R. L. 2004, ACS CCD Gains, Full Well Depths, and Linearity up to and Beyond Saturation, Instrument Science Report ACS 2004-01, 1
Gilliland, R. L., Rajan, A., & Deustua, S. 2010, WFC3 UVIS Full Well Depths, and Linearity Near and Beyond Saturation, Space Telescope WFC Instrument Science Report, 18
Goudfrooij, P., Puzia, T. H., Kozhurina-Platais, V., & Chandar, R. 2011, ApJ, 737, 3
Goudfrooij, P., Girardi, L., Kozhurina-Platais, V., et al. 2014, ApJ, 797, 35
Goudfrooij, P., Girardi, L., Bellini, A., et al. 2018, ApJ, 864, L3
Halir, R., & Flusser, J. 1998, Proceedings of the 6th International Conference in Central Europe on Computer Graphics and Visualization. WSCG '98, 125
Hastings, B., Wang, C., & Langer, N. 2020, A&A, 633, A165
Hastings, B., Langer, N., Wang, C., Schootemeijer, A., & Milone, A. P. 2021, A&A, 653, A144
Helmi, A., Babusiaux, C., Koppelman, H. H., et al. 2018, Nature, 563, 85
Huang, W., & Gies, D. R. 2006, ApJ, 648, 580
Huang, W., Gies, D. R., & McSwain, M. V. 2010, ApJ, 722, 605
Jang, S., Milone, A. P., Legnardi, M. V., et al. 2022, MNRAS, 517, 5687
Kamann, S., Bastian, N., Gossage, S., et al. 2020, MNRAS, 492, 2177
Keller, S. C., Bessell, M. S., & Da Costa, G. S. 2000, AJ, 119, 1748
Lagioia, E. P., Milone, A. P., Marino, A. F., Cordoni, G., & Tailo, M. 2019a, AJ, 158, 202
Lagioia, E. P., Milone, A. P., Marino, A. F., & Dotter, A. 2019b, ApJ, 871, 140
Li, C., de Grijs, R., Deng, L., et al. 2016, Nature, 529, 502
Li, C., de Grijs, R., Deng, L., & Milone, A. P. 2017, ApJ, 844, 119
Mackey, A. D., & Broby, Nielsen P. 2007, MNRAS, 379, 151
Mackey, A. D., Broby, Nielsen P., Ferguson, A. M. N., & Richardson, J. C. 2008, ApJ, 681, L17
Marigo, P., Girardi, L., Bressan, A., et al. 2017, ApJ, 835, 77
Marino, A. F., Villanova, S., Piotto, G., et al. 2008, A&A, 490, 625
Marino, A. F., Milone, A. P., Yong, D., et al. 2014, MNRAS, 442, 3044
Marino, A. F., Przybilla, N., Milone, A. P., et al. 2018a, AJ, 156, 116
Marino, A. F., Milone, A. P., Casagrande, L., et al. 2018b, ApJ, 863, L33
Massari, D., Raso, S., Libralato, M., & Bellini, A. 2021, MNRAS, 500, 2012
Meyssonnier, N., & Azzopardi, M. 1993, A&AS, 102, 451
Milone, A. P., & Marino, A. F. 2022, Universe, 8, 359
Milone, A. P., Bedin, L. R., Piotto, G., & Anderson, J. 2009, A&A, 497, 755
Milone, A. P., Piotto, G., Bedin, L. R., et al. 2012, A&A, 540, A16
Milone, A. P., Bedin, L. R., Cassisi, S., et al. 2013, A&A, 555, A143
Milone, A. P., Bedin, L. R., Piotto, G., et al. 2015, MNRAS, 450, 3750
Milone, A. P., Marino, A. F., D'Antona, F., et al. 2016, MNRAS, 458, 4368
Milone, A. P., Piotto, G., Renzini, A., et al. 2017, MNRAS, 464, 3636
Milone, A. P., Marino, A. F., Di Criscienzo, M., et al. 2018, MNRAS, 477, 2640
Milone, A. P., Marino, A. F., Da Costa, G. S., et al. 2020, MNRAS, 491, 515
Mowlavi, N., Eggenberger, P., Meynet, G., et al. 2012, A&A, 541, A41
Nardiello, D., Libralato, M., Piotto, G., et al. 2018, MNRAS, 481, 3382
Niederhofer, F., Georgy, C., Bastian, N., & Ekström, S. 2015, MNRAS, 453, 2070
Paxton, B., Bildsten, L., Dotter, A., et al. 2011, ApJS, 192, 3
Piatti, A. E. 2021, A&A, 650, A52
Piatti, A. E., de Grijs, R., Ripepi, V., et al. 2015, MNRAS, 454, 839
Pietrinferni, A., Cassisi, S., Salaris, M., & Castelli, F. 2004, ApJ, 612, 168
Piotto, G., Milone, A. P., Anderson, J., et al. 2012, ApJ, 760, 39
Rachford, B. L., & Canterna, R. 2000, AJ, 119, 1296
Sabbi, E., Sirianni, M., Nota, A., et al. 2007, AJ, 133, 44
Sabbi, E., Lennon, D. J., Anderson, J., et al. 2016, ApJS, 222, 11
Salinas, R., Pajkos, M. A., Vivas, A. K., Strader, J., & Contreras, Ramos R. 2018, AJ, 155, 183
Schmidt, T., Cioni, M.-R. L., Niederhofer, F., et al. 2022, A&A, 663, A107
Silverman, B. W. 1986, Density Estimation for Statistics and Data Analysis (London: Chapman and Hall)
Vasiliev, E. 2019, MNRAS, 489, 623
van der Marel, R. P., & Kallivayalil, N. 2014, ApJ, 781, 121
Wang, C., Langer, N., Schootemeijer, A., et al. 2020, ApJ, 888, L12
Wang, C., Langer, N., Schootemeijer, A., et al. 2022, Nat. Astron., 6, 480
Westerlund, B. E., & Smith, L. F. 1964, MNRAS, 128, 311
Wu, X., Li, C., de Grijs, R., & Deng, L. 2016, ApJ, 826, L14
Zivick, P., Kallivayalil, N., van der Marel, R. P., et al. 2018, ApJ, 864, 55
Zorec, J., & Royer, F. 2012, A&A, 537, A120

Appendix A: Serendipitous discoveries

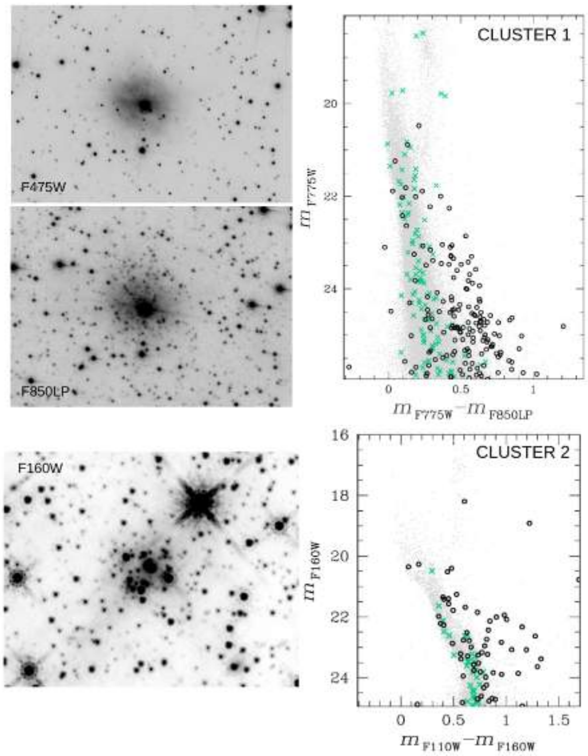

Fig. A.1. Images of the star clusters discovered in this paper. *Top panels*. Stacked images in F475W and F850LP centered on the cluster 1 discovered in this paper (left). The m_{F775W} vs. $m_{F775W} - m_{F850LP}$ diagram is plotted on the right for all stars in the ACS/WFC field (gray points), stars in the cluster 1 field (black circles) and in the reference field (aqua crosses). *Bottom panels*. Stacked image in F160W for the discovered cluster 2 (left) and m_{F160W} vs. $m_{F110W} - m_{F160W}$ CMD (right). Gray, black, and aqua symbols indicate stars in the WFC3/NIR field, stars in the cluster field, and in the reference field, respectively.

We report the serendipitous findings of two new star clusters, hereafter clusters 1 and 2. Two zoom-ins of the region around cluster 1 are provided in the top-left panels of Fig. A.1, where we provide the monochromatic images in the F475W and F850LP bands. The cluster, which is centered around RA=00:45:21.28, Dec.=−73:12:18.1, J2000 is clearly visible in the F850LP image, while the most prominent feature of the F475W image is a nebula that envelopes it. The top-right panel shows the m_{F775W} versus $m_{F775W} - m_{F850LP}$ CMD for all stars in the WFC/ACS field that includes cluster 1. The bright star close to the cluster center is classified as the Hα emission-line star MA93-99 by Meyssonnier & Azzopardi (1993). We defined a circle centered on the cluster with a 4 arcsec radius (hereafter cluster region) and represented with black circles all stars within this region. We also plot the stars in a randomly selected reference region with the same area as the cluster region with aqua crosses. Clearly, we note an overdensity of stars in the cluster region with red $m_{F775W} - m_{F850LP}$ colors and luminosity fainter than $m_{F775W} \sim 23$. These stars are qualitatively consistent with a population of pre-MS stars.

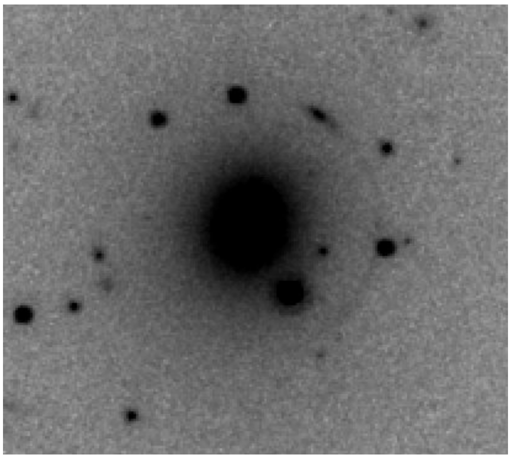

Fig. A.2. Stacked F814W WFC/ACS image of the field around the early-type galaxy centered at RA=00 48 57.01, Dec.=−69 51 30.4, J2000. Note the elongated arc-like structure due to gravitational lensing.

Cluster 2 is located around RA=05:03:55.87 Dec.=−66:24:36.9, J2000 and is shown in the F160W image plotted on the bottom-left of Fig. A.1. The m_{F160W} versus $m_{F110W} - m_{F160W}$ CMD plotted in the right panel reveals an overdensity of red stars in the cluster field, which suggests that cluster 2 hosts a conspicuous population of pre-MS stars.

As a further outcome of the survey, we report the serendipitous discovery of a gravitational lens in the field of view of the SMC star cluster Lindsay 38. The F814W stacked image shown in Fig. A.2 reveals an elongated arc-like structure around what appears to be a single early-type galaxy centered on the coordinates RA=00 48 57.01, Dec.=−69 51 30.4, J2000. Its spatial extension is such that fine structures of the source are detectable in the arc. This object may correspond to a strong lensing configuration that implies remarkable alignment between lens and source along the line of sight. Due to their intrinsic symmetry, such a peculiar configuration would permit the total enclosed mass within the projected Einstein radius to be constrained with great accuracy (e.g., Bettinelli et al. 2016, and references therein).

Appendix B: Tables

Table B.1. Description of the HST images used in the paper.

ESO121-03		
ACS/WFC	F435W	1170
ACS/WFC	F555W	330
ACS/WFC	F606W	710
ACS/WFC	F814W	908
Hodge 2		
ACS/WFC	F475W	1440
ACS/WFC	F814W	1430
Hodge 6		
WFC3/UVIS	F475W	1440
WFC3/UVIS	F814W	1430
Hodge 7		
ACS/WFC	F555W	330
ACS/WFC	F814W	200
Hodge 11		
WFC3/UVIS	F336W	10848
ACS/WFC	F606W	4390
ACS/WFC	F814W	6932
HW 57		
ACS/WFC	F475W	2490
ACS/WFC	F814W	2700
IC 1660		
ACS/WFC	F555W	73
ACS/WFC	F814W	58
IC 2146		
ACS/WFC	F555W	250
ACS/WFC	F814W	170
KMHK 240		
ACS/WFC	F475W	575
ACS/WFC	F814W	1330
KMHK 250		
ACS/WFC	F435W	720
ACS/WFC	F555W	700
ACS/WFC	F814W	700
KMHK 291		
ACS/WFC	F475W	575
ACS/WFC	F814W	1330
KMHK 316		
ACS/WFC	F475W	575
ACS/WFC	F814W	1330
KMHK 676		
ACS/WFC	F475W	575
ACS/WFC	F814W	3832
NGC 419		
WFC3/UVIS	F336W	9056
WFC3/UVIS	F343N	18563
WFC3/UVIS	F438W	4028
ACS/WFC	F555W	2024
ACS/WFC	F814W	4012
NGC 422		
ACS/WFC	F555W	73
ACS/WFC	F814W	58
NGC 602		
ACS/WFC	F555W	4338
ACS/WFC	F814W	4450
NGC 1466		
WFC3/UVIS	F336W	11668
ACS/WFC	F606W	4336
ACS/WFC	F814W	7082
NGC 1644		
ACS/WFC	F555W	250
ACS/WFC	F814W	170
NGC 1651		
WFC3/UVIS	F475W	1440
WFC3/UVIS	F814W	1430
NGC 1652		
ACS/WFC	F555W	300
ACS/WFC	F814W	200
NGC 1718		
WFC3/UVIS	F475W	1440
WFC3/UVIS	F814W	1430
NGC 1751		
WFC3/UVIS	F336W	3580
ACS/WFC	F435W	770
ACS/WFC	F555W	984
ACS/WFC	F814W	888
NGC 1755		
WFC3/UVIS	F336W	5688
WFC3/UVIS	F814W	3072
ACS/WFC	F555W	50
ACS/WFC	F814W	40
NGC 1756		
ACS/WFC	F555W	170
ACS/WFC	F814W	120
NGC 1868		
WFC3/UVIS	F336W	2492
WFC3/UVIS	F656N	1429
WFC3/UVIS	F814W	756
NGC 1872		
ACS/WFC	F555W	115
ACS/WFC	F814W	90
NGC 1898		
WFC3/UVIS	F336W	2070
WFC3/UVIS	F438W	400
WFC3/UVIS	F814W	100
ACS/WFC	F475W	1000
ACS/WFC	F814W	1000
NGC 1903		
ACS/WFC	F555W	40
ACS/WFC	F814W	50
NGC 1917		
ACS/WFC	F555W	300
ACS/WFC	F814W	200
NGC 1928		
ACS/WFC	F555W	330
ACS/WFC	F814W	200
NGC 1939		
ACS/WFC	F555W	330
ACS/WFC	F814W	200
NGC 1943		
ACS/WFC	F555W	50
ACS/WFC	F814W	40
NGC 1953		
WFC3/UVIS	F336W	2503
WFC3/UVIS	F656N	1440
WFC3/UVIS	F814W	756
ACS/WFC	F555W	115
ACS/WFC	F814W	90
NGC 1966		
ACS/WFC	F475W	2829
ACS/WFC	F814W	1403
NGC 1978		
WFC3/UVIS	F275W	17970
WFC3/UVIS	F336W	3720
WFC3/UVIS	F343N	3975
WFC3/UVIS	F438W	2475

Notes. For each cluster, we provide the camera(s), the filters, and the total exposure times in seconds.

Table B.1. continued.

CS/WFC	F814W	1330	**NGC 1783**			WFC3/UVIS	F555W	1040
KMHK 1231			WFC3/UVIS	F275W	9045	WFC3/UVIS	F814W	2334
ACS/WFC	F435W	130	WFC3/UVIS	F336W	3580	ACS/WFC	F555W	300
ACS/WFC	F555W	100	WFC3/UVIS	F343N	27651	ACS/WFC	F814W	200
ACS/WFC	F656N	600	WFC3/UVIS	F438W	5628	**NGC 1983**		
ACS/WFC	F814W	80	ACS/WFC	F435W	770	ACS/WFC	F555W	20
KMK 8827			ACS/WFC	F555W	870	ACS/WFC	F814W	20
ACS/WFC	F475W	601	ACS/WFC	F814W	858	**NGC 1987**		
ACS/WFC	F814W	1330	**NGC 1786**			ACS/WFC	F435W	770
Kron 1			WFC3/UVIS	F336W	2030	ACS/WFC	F555W	970
ACS/WFC	F555W	480	WFC3/UVIS	F438W	400	ACS/WFC	F814W	858
ACS/WFC	F814W	290	WFC3/UVIS	F814W	100	**NGC 2002**		
Kron 3			**NGC 1793**			ACS/WFC	F555W	20
ACS/WFC	F555W	2024	ACS/WFC	F475W	2829	ACS/WFC	F814W	20
ACS/WFC	F814W	1916	ACS/WFC	F814W	1403	**NGC 2005**		
Kron 21			**NGC 1795**			ACS/WFC	F475W	1440
ACS/WFC	F555W	480	ACS/WFC	F555W	300	ACS/WFC	F814W	1430
ACS/WFC	F814W	290	ACS/WFC	F814W	200	**NGC 2010**		
Kron 29			**NGC 1801**			ACS/WFC	F555W	20
ACS/WFC	F435W	440	WFC3/UVIS	F336W	2503	ACS/WFC	F814W	20
ACS/WFC	F555W	560	WFC3/UVIS	F656N	1440	**NGC 2031**		
ACS/WFC	F814W	560	WFC3/UVIS	F814W	756	ACS/WFC	F435W	130
Kron 34			ACS/WFC	F555W	115	ACS/WFC	F555W	100
WFC3/UVIS	F336W	2517	ACS/WFC	F814W	90	ACS/WFC	F658N	600
WFC3/UVIS	F656N	1440	**NGC 1805**			ACS/WFC	F814W	80
WFC3/UVIS	F814W	770	WFC3/UVIS	F225W	4800	**NGC 2056**		
ACS/WFC	F555W	165	WFC3/UVIS	F336W	3741	ACS/WFC	F555W	170
ACS/WFC	F814W	130	WFC3/UVIS	F656N	1440	ACS/WFC	F814W	120
Lindsay 1			WFC3/UVIS	F814W	756	**NGC 2107**		
WFC3/UVIS	F275W	27341	**NGC 1806**			ACS/WFC	F555W	170
WFC3/UVIS	F336W	2900	WFC3/UVIS	F336W	3580	ACS/WFC	F814W	120
WFC3/UVIS	F343N	4800	WFC3/UVIS	F343N	2945	**NGC 2108**		
WFC3/UVIS	F438W	1040	ACS/WFC	F435W	770	ACS/WFC	F435W	770
ACS/WFC	F555W	2504	ACS/WFC	F555W	1020	ACS/WFC	F555W	970
ACS/WFC	F814W	2206	ACS/WFC	F814W	888	ACS/WFC	F814W	858
Lindsay 38			**NGC 1810**			**NGC 2121**		
WFC3/UVIS	F336W	1688	ACS/WFC	F475W	1357	WFC3/UVIS	F275W	18239
WFC3/UVIS	F343N	3630	ACS/WFC	F814W	572	WFC3/UVIS	F336W	1700
WFC3/UVIS	F438W	1199	**NGC 1818**			WFC3/UVIS	F343N	2660
ACS/WFC	F555W	2460	WFC3/UVIS	F225W	4800	WFC3/UVIS	F438W	1120
ACS/WFC	F814W	2162	WFC3/UVIS	F275W	1962	WFC3/UVIS	F814W	2350
Lindsay 114			WFC3/UVIS	F336W	3741	**NGC 2154**		
ACS/WFC	F555W	480	WFC3/UVIS	F475W	100	WFC3/UVIS	F336W	2140
ACS/WFC	F814W	290	WFC3/UVIS	F606W	2268	WFC3/UVIS	F555W	1040
NGC 121			WFC3/UVIS	F814W	3156	ACS/WFC	F555W	300
WFC3/UVIS	F336W	4244	**NGC 1831**			ACS/WFC	F814W	200
WFC3/UVIS	F343N	2950	WFC3/UVIS	F336W	4180	**NGC 2155**		
WFC3/UVIS	F438W	800	WFC3/UVIS	F814W	1480	WFC3/UVIS	F336W	1160
WFC3/UVIS	F814W	200	**NGC 1841**			WFC3/UVIS	F343N	2650
ACS/WFC	F555W	2024	WFC3/UVIS	F336W	11668	WFC3/UVIS	F438W	1210
ACS/WFC	F814W	1916	ACS/WFC	F606W	4336	**NGC 2156**		

Table B.1. continued.

NGC 152			ACS/WFC	F814W	7082	ACS/WFC	F475W	1357
WFC3/UVIS	F438W	1500	**NGC 1844**			ACS/WFC	F814W	664
WFC3/UVIS	F814W	700	ACS/WFC	F475W	6300	**NGC 2164**		
NGC 265			ACS/WFC	F814W	1686	WFC3/UVIS	F225W	4800
ACS/WFC	F435W	440	**NGC 1846**			WFC3/UVIS	F336W	3741
ACS/WFC	F555W	589	WFC3/UVIS	F336W	9156	WFC3/UVIS	F656N	848
ACS/WFC	F814W	589	WFC3/UVIS	F343N	2945	WFC3/UVIS	F814W	1440
NGC 290			WFC3/NIR	F160W	2844	**NGC 2173**		
ACS/WFC	F435W	440	ACS/WFC	F435W	770	WFC3/UVIS	F336W	2200
ACS/WFC	F555W	560	ACS/WFC	F555W	1020	WFC3/UVIS	F475W	1520
ACS/WFC	F814W	560	ACS/WFC	F814W	888	WFC3/UVIS	F814W	1980
NGC 294			**NGC 1850**			**NGC 2203**		
WFC3/UVIS	F336W	2517	WFC3/UVIS	F275W	1720	WFC3/UVIS	F336W	2200
WFC3/UVIS	F656N	1440	WFC3/UVIS	F336W	2550	WFC3/UVIS	F475W	1520
WFC3/UVIS	F814W	770	WFC3/UVIS	F343N	4075	WFC3/UVIS	F814W	1980
ACS/WFC	F555W	165	WFC3/UVIS	F438W	1045	**NGC 2209**		
ACS/WFC	F814W	130	WFC3/UVIS	F467M	1980	WFC3/UVIS	F438W	1700
NGC 299			WFC3/UVIS	F475W	1070	WFC3/UVIS	F814W	1030
WFC3/UVIS	F656N	2394	WFC3/UVIS	F502N	2051	**NGC 2210**		
ACS/WFC	F555W	1858	WFC3/UVIS	F547M	782	WFC3/UVIS	F336W	10806
ACS/WFC	F814W	1966	WFC3/UVIS	F555W	1137	ACS/WFC	F606W	4306
NGC 330			WFC3/UVIS	F657N	2979	ACS/WFC	F814W	6950
WFC3/UVIS	F225W	4860	WFC3/UVIS	F656N	4225	**NGC 2213**		
WFC3/UVIS	F336W	3795	WFC3/UVIS	F673N	1982	WFC3/UVIS	F475W	1440
WFC3/UVIS	F656N	1440	WFC3/UVIS	F814W	1867	WFC3/UVIS	F814W	1430
WFC3/UVIS	F814W	770	WFC3/NIR	F160W	9445	**NGC 2249**		
NGC 339			WFC3/NIR	F164N	2012	WFC3/UVIS	F438W	1650
WFC3/UVIS	F336W	3060	**NGC 1852**			WFC3/UVIS	F814W	910
WFC3/UVIS	F343N	4220	WFC3/UVIS	F336W	2140	**NGC 2257**		
WFC3/UVIS	F438W	1520	WFC3/UVIS	F555W	1040	WFC3/UVIS	F336W	10619
ACS/WFC	F555W	2024	ACS/WFC	F555W	330	ACS/WFC	F606W	4360
ACS/WFC	F814W	1926	ACS/WFC	F814W	200	ACS/WFC	F814W	6788
NGC 346			**NGC 1854**			**Reticulum**		
WFC3/UVIS	F225W	2	ACS/WFC	F555W	50	WFC3/UVIS	F336W	10978
ACS/WFC	F555W	9110	ACS/WFC	F814W	40	WFC3/UVIS	F438W	400
ACS/WFC	F656N	1542	**NGC 1856**			WFC3/UVIS	F814W	100
ACS/WFC	F814W	8632	WFC3/UVIS	F336W	5688	ACS/WFC	F555W	330
NGC 376			WFC3/UVIS	F343N	2750	ACS/WFC	F606W	4327
WFC3/UVIS	F656N	2389	WFC3/UVIS	F438W	1045	ACS/WFC	F814W	6979
ACS/WFC	F555W	1806	WFC3/UVIS	F555W	700	**SL 862**		
ACS/WFC	F814W	1966	WFC3/UVIS	F656N	2615	ACS/WFC	F435W	735
NGC 411			WFC3/UVIS	F814W	4037	ACS/WFC	F555W	705
WFC3/UVIS	F336W	2200	**NGC 1858**			ACS/WFC	F814W	695
WFC3/UVIS	F475W	1520	ACS/WFC	F555W	20	**Cluster 1**		
WFC3/UVIS	F814W	1980	ACS/WFC	F814W	20	ACS/WFC	F475W	12695
NGC 416			**NGC 1866**			ACS/WFC	F775W	28900
WFC3/UVIS	F275W	27349	WFC3/UVIS	F336W	5688	ACS/WFC	F850LP	9190
WFC3/UVIS	F336W	3060	WFC3/UVIS	F343N	3900	**Cluster 2**		
WFC3/UVIS	F343N	4605	WFC3/UVIS	F438W	1195	WFC3/NIR	F110W	12592
WFC3/UVIS	F438W	1125	WFC3/UVIS	F555W	2520	WFC3/NIR	F160W	24784
ACS/WFC	F555W	2064	WFC3/UVIS	F814W	3072			

Table B.2. Cluster-center coordinates, average proper motions, distance modulus, reddening, metallicities, and ages for the studied clusters.

ID	RA h m s	error [arcsec]	Dec. d m s	error [arcsec]	$\mu_\alpha\cos\delta$ [mas yr^{-1}]	μ_δ [mas yr^{-1}]	(m−M)$_0$ [mag]	E(B−V) [mag]	[M/H] [dex]	age^a [Gyr]	age^b [Gyr]
BRHT 5b	05 08 52.65	—	−68 45 18.0	—	2.09±0.03	0.04±0.09	18.40	0.12	−0.4	0.015	—
BS 90	00 59 04.86	±0.4	−72 09 10.3	±4.7	0.67±0.05	−1.06±0.06	18.91	0.03	−0.7	4.2	—
BSDL 1650	05 25 50.01	—	−68 49 16.0	—	1.54±0.19	0.34±0.15	18.38	0.18	−0.4	0.30	—
ESO 121-03	06 02 02.40	±0.8	−60 31 26.0	±1.2	1.61±0.04	0.92±0.06	18.34	0.05	−0.8	6.9	—
Hodge 02	05 17 48.88	±0.1	−69 38 43.4	±0.3	2.29±0.13	0.43±0.15	18.32	0.12	−0.5	1.70	1.35
Hodge 06	05 42 17.65	±0.8	−71 35 28.2	±0.5	1.95±0.06	0.76±0.06	18.40	0.15	−0.5	2.30	—
Hodge 07	05 50 02.99	±0.4	−67 43 06.6	±1.0	1.77±0.05	0.75±0.07	18.33	0.06	−0.5	2.00	1.75
Hodge 11	06 14 22.89	±0.2	−69 50 50.6	±0.2	1.56±0.08	0.75±0.07	18.57	0.05	−1.7	13.4	—
HW 57	01 07 43.22	±0.7	−71 52 37.5	±0.8	0.77±0.14	−1.03±0.06	19.18	0.12	−1.3	5.3	—
IC 1641	01 09 38.82	±0.6	−71 46 04.4	±1.3	1.04±0.06	−1.11±0.09	18.93	0.02	−0.6	1.20	0.80
IC 1660	01 12 37.59	±0.3	−71 45 41.4	±0.3	1.07±0.05	−1.30±0.04	19.06	0.07	−0.2	0.11	—
IC 2146	05 37 47.37	±0.6	−74 47 01.3	±0.6	2.02±0.03	0.73±0.03	18.42	0.05	−0.4	2.20	2.00
KMHK 240	04 54 26.88	±0.9	−68 14 55.1	±0.6	2.26±0.12	−0.01±0.11	18.52	0.12	−0.5	2.10	1.90
KMHK 250	04 54 30.32	±0.2	−69 55 15.1	±0.4	2.01±0.09	0.01±0.08	18.51	0.11	−0.5	1.80	1.45
KMHK 291	04 55 45.26	±0.2	−68 16 56.2	±0.5	1.74±0.12	−0.13±0.11	18.55	0.12	−0.2	0.30	0.15
KMHK 361	04 56 37.46	±1.4	−68 09 55.8	±0.7	1.69±0.16	0.06±0.13	18.43	0.06	−0.3	1.35	1.00
KMHK 598	05 09 35.72	—	−67 48 31.2	—	1.76±0.12	0.04±0.22	18.50	0.06	−0.2	0.15	—
KMHK 676	05 14 44.37	±1.8	−65 20 08.5	±0.9	1.61±0.04	0.15±0.08	18.49	0.07	−0.2	0.14	—
KMHK 987	05 30 32.71	±0.8	−66 54 12.4	±0.4	1.55±0.03	0.47±0.04	18.52	0.07	−0.2	0.017	—
KMHK 1073	05 33 10.75	—	−71 01 21.0	—	2.10±0.07	0.54±0.06	18.34	0.11	−0.4	0.45	0.30
KMHK 1231	05 41 09.62	±3.1	−69 54 12.4	±0.4	1.96±0.09	0.63±0.15	18.47	0.13	−0.3	0.35	0.20
KMK 8827	05 08 54.14	—	−69 00 15.2	—	1.81±0.58	−0.30±0.61	18.40	0.11	−0.2	0.20	—
KMK 8849	05 21 10.76	—	−69 56 30.3	—	2.51±0.41	0.34±0.13	18.44	0.22	−0.4	0.50	0.25
Kron 1	00 21 25.78	±1.2	−73 44 55.7	±0.5	0.35±0.06	−1.35±0.06	18.90	0.03	−0.9	6.8	—
Kron 3	00 24 46.63	±0.8	−72 47 37.0	±0.2	0.53±0.02	−1.35±0.03	18.93	0.02	−0.9	5.6	—
Kron 21	00 41 24.39	±0.3	−72 53 23.8	±0.2	0.62±0.02	−1.53±0.03	18.84	0.06	−1.0	4.4	—
Kron 29	00 51 53.15	±0.2	−72 57 12.2	±0.3	0.65±0.05	−1.21±0.03	19.10	0.07	−0.4	0.25	0.12
Kron 34	00 55 33.44	±1.5	−72 49 57.6	±1.5	0.69±0.04	−1.25±0.04	18.90	0.12	−0.6	0.85	0.55
Lindsay 1	00 03 54.44	±2.0	−73 28 18.7	±1.3	0.54±0.03	−1.49±0.03	18.86	0.04	−1.2	7.2	—
Lindsay 38	00 48 49.80	±2.5	−69 52 12.6	±1.6	0.54±0.03	−0.86±0.03	19.22	0.01	−1.2	5.4	—
Lindsay 91	01 12 51.76	±0.2	−73 07 07.4	±0.5	0.76±0.07	−1.09±0.04	18.97	0.10	−0.8	4.2	—
Lindsay 113	01 49 29.69	±4.0	−73 43 40.2	±1.3	1.30±0.02	−1.18±0.03	18.76	0.03	−0.8	3.6	—
Lindsay 114	01 50 19.27	±0.3	−74 21 20.5	±0.4	1.09±0.03	−1.14±0.04	18.86	0.07	−0.4	0.04	—
NGC 121	00 26 48.94	±0.1	−71 32 09.4	±0.1	0.23±0.03	−1.23±0.03	19.05	0.04	−1.2	9.7	—
NGC 152	00 32 56.47	±1.2	−73 06 59.2	±2.2	0.41±0.03	−1.26±0.04	19.07	0.03	−0.6	1.90	1.45
NGC 265	00 47 11.82	±0.6	−73 28 38.2	±0.2	0.64±0.03	−1.31±0.04	19.03	0.06	−0.5	0.45	0.25

Notes. (a)The ages of clusters with the eMSTO are inferred by fitting the isochrone to the lower part of the eMSTO. See Sect. 2.5 for details. (b)The ages of clusters with the eMSTO are inferred by fitting the isochrone to the upper part of the eMSTO. See Sect. 2.5 for details. (c)NGC 1850A is a clump of stars located on the west side of NGC 1850 and is often considered a separate cluster (e.g., Caloi & Cassatella 1998). Based on the results of this table, NGC 1850 and NGC 1850A share similar proper motions, distance, metallicity, and age.

Table B.2. continued.

ID	RA h m s	error [arcsec]	Dec. d m s	error [arcsec]	$\mu_\alpha \cos\delta$ [mas yr^{-1}]	μ_δ [mas yr^{-1}]	(m−M)$_0$ [mag]	E(B−V) [mag]	[M/H] [dex]	age[a] [Gyr]	age[b] [Gyr]
NGC 290	00 51 14.24	—	−73 09 42.2	—	0.67±0.09	−1.47±0.07	18.95	0.05	−0.5	0.30	0.20
NGC 294	00 53 05.58	±1.4	−73 22 48.7	±3.2	0.53±0.05	−1.27±0.04	18.98	0.12	−0.7	0.70	0.45
NGC 299	00 53 24.51	±0.2	−72 11 50.6	±0.2	0.69±0.04	−1.25±0.02	18.99	0.06	−0.4	0.08	0.02
NGC 330	00 56 18.23	±0.1	−72 27 32.3	±0.1	0.75±0.03	−1.31±0.03	19.04	0.04	−0.4	0.09	0.04
NGC 339	00 57 46.56	±0.5	−74 28 13.2	±0.4	0.70±0.03	−1.25±0.04	18.96	0.07	−1.3	5.9	—
NGC 346	00 59 04.93	±0.6	−72 10 37.4	±0.4	0.70±0.04	−1.23±0.03	18.94	0.08	−0.4	0.005	—
NGC 376	01 03 52.75	±0.7	−72 49 32.0	±0.3	0.72±0.04	−1.31±0.03	18.98	0.07	−0.4	0.028	0.018
NGC 411	01 07 55.95	±0.4	−71 46 04.1	±0.4	0.87±0.08	−1.12±0.06	18.97	0.06	−0.7	1.95	1.55
NGC 416	01 07 59.17	±0.2	−72 21 19.7	±0.1	0.88±0.04	−1.24±0.03	18.96	0.11	−1.2	6.0	—
NGC 419	01 08 17.57	±0.7	−72 53 03.8	±1.0	0.77±0.06	−1.22±0.04	18.85	0.07	−0.7	2.00	1.55
NGC 422	01 09 24.48	±6.2	−71 45 59.3	±0.9	0.93±0.04	−1.27±0.03	18.88	0.04	−0.4	0.30	0.20
NGC 602	01 29 31.50	±0.8	−73 33 40.8	±0.4	0.96±0.02	−1.26±0.05	19.01	0.06	−0.2	0.005	0.002
NGC 1466	03 44 32.76	±1.3	−71 40 15.5	±0.3	1.72±0.06	−0.74±0.07	18.58	0.05	−1.5	13.2	—
NGC 1644	04 37 39.85	±0.3	−66 11 56.3	±0.5	1.80±0.02	−0.29±0.11	18.45	0.03	−0.6	1.80	1.45
NGC 1651	04 37 32.23	±0.6	−70 35 10.8	±0.3	2.02±0.04	−0.30±0.05	18.48	0.13	−0.6	2.20	2.05
NGC 1652	04 38 22.77	±0.3	−68 40 19.8	±0.2	1.87±0.06	−0.37±0.07	18.46	0.08	−0.6	2.25	—
NGC 1718	04 52 25.89	±0.2	−67 03 06.6	±0.4	1.85±0.03	−0.41±0.04	18.43	0.22	−0.5	2.05	1.85
NGC 1749	04 54 56.73	—	−68 11 19.1	—	1.94±0.08	−0.10±0.12	18.30	0.10	−0.4	0.13	0.07
NGC 1751	04 54 11.99	±1.1	−69 48 27.1	±0.6	1.93±0.07	−0.09±0.10	18.52	0.15	−0.5	1.75	1.45
NGC 1755	04 55 15.56	±0.2	−68 12 18.8	±0.6	1.88±0.04	−0.11±0.05	18.33	0.11	−0.2	0.11	0.07
NGC 1756	04 54 49.69	±0.7	−69 14 13.2	±0.3	1.83±0.04	0.10±0.03	18.55	0.22	−0.4	0.20	0.15
NGC 1783	04 59 08.97	±0.5	−65 59 13.8	±0.2	1.64±0.04	−0.06±0.04	18.51	0.03	−0.4	1.95	1.65
NGC 1786	04 59 07.99	±0.1	−67 44 43.9	±0.3	1.95±0.03	0.06±0.03	18.42	0.09	−1.5	12.9	—
NGC 1793	04 59 38.74	±0.1	−69 33 27.8	±0.1	2.09±0.08	−0.05±0.05	18.48	0.14	−0.2	0.15	0.06
NGC 1795	04 59 47.35	±1.1	−69 48 06.5	±0.3	1.90±0.05	0.23±0.11	18.45	0.09	−0.4	1.85	1.50
NGC 1801	05 00 35.41	±0.2	−69 36 49.9	±0.7	1.90±0.05	0.05±0.04	18.39	0.12	−0.3	0.45	0.30
NGC 1805	05 02 21.78	±0.1	−66 06 41.9	±0.1	1.56±0.04	0.10±0.06	18.32	0.05	−0.4	0.10	0.045
NGC 1806	05 02 11.72	±0.4	−67 59 08.0	±0.5	1.85±0.05	−0.06±0.07	18.52	0.04	−0.4	1.90	1.60
NGC 1810	05 03 23.06	±0.7	−66 22 56.7	±1.4	1.72±0.05	0.07±0.04	18.45	0.04	−0.2	0.08	0.045
NGC 1818	05 04 13.43	±0.4	−66 26 01.7	±1.2	1.64±0.04	0.09±0.06	18.44	0.07	−0.2	0.07	0.035
NGC 1831	05 06 16.38	±0.4	−64 55 06.1	±0.8	1.69±0.11	−0.04±0.10	18.41	0.05	−0.3	0.90	0.70
NGC 1841	04 45 22.75	±0.4	−83 59 55.6	±0.6	2.05±0.02	0.00±0.03	18.34	0.13	−1.3	12.4	—
NGC 1844	05 07 30.38	±0.9	−67 19 28.6	±1.9	1.68±0.02	−0.03±0.03	18.47	0.07	−0.2	0.17	0.09
NGC 1846	05 07 34.15	±0.4	−67 27 36.7	±0.2	1.71±0.04	0.03±0.04	18.52	0.05	−0.4	1.95	1.60
NGC 1850	05 08 45.19	±1.3	−68 45 42.0	±1.5	2.02±0.04	0.11±0.04	18.38	0.13	−0.4	0.12	0.07
NGC 1850A[c]	05 08 39.44	—	−68 45 44.2	—	1.95±0.04	0.13±0.01	18.36	0.11	−0.4	0.020	0.10

Table B.2. continued.

ID	RA h m s	error [arcsec]	Dec. d m s	error [arcsec]	$\mu_\alpha\cos\delta$ [mas yr^{-1}]	μ_δ [mas yr^{-1}]	(m−M)$_0$ [mag]	E(B−V) [mag]	[M/H] [dex]	age^a [Gyr]	age^b [Gyr]
NGC 1852	05 09 23.95	±0.3	−67 46 45.6	±0.2	1.78±0.04	0.16±0.06	18.52	0.07	−0.4	1.75	1.40
NGC 1854	05 09 19.83	±0.5	−68 50 52.0	±0.8	2.09±0.04	0.15±0.02	18.42	0.09	−0.2	0.15	0.09
NGC 1856	05 09 30.08	±0.1	−69 07 43.9	±0.3	1.88±0.05	0.20±0.05	18.32	0.17	−0.4	0.45	0.25
NGC 1858	05 10 00.07	—	−68 54 15.1	—	1.87±0.04	0.25±0.03	18.46	0.12	−0.2	0.017	0.004
NGC 1866	05 13 38.65	±0.3	−65 27 52.8	±0.4	1.55±0.03	0.16±0.03	18.30	0.06	−0.4	0.40	0.20
NGC 1868	05 14 35.91	±0.4	−63 57 15.1	±0.1	1.83±0.04	0.05±0.07	18.45	0.06	−0.4	1.45	1.15
NGC 1872	05 13 11.29	±0.8	−69 18 44.9	±0.3	1.79±0.08	0.52±0.05	18.31	0.18	−0.4	0.60	0.40
NGC 1898	05 16 41.57	±0.3	−69 39 24.1	±0.1	1.98±0.05	0.35±0.05	18.60	0.06	−1.5	11.7	—
NGC 1903	05 17 22.62	±0.3	−69 20 17.0	±0.5	2.01±0.07	0.16±0.05	18.40	0.06	−0.2	0.15	0.10
NGC 1917	05 19 01.94	±0.4	−69 00 05.5	±0.5	1.65±0.11	0.57±0.09	18.36	0.05	−0.3	1.70	1.40
NGC 1928	05 20 57.49	±1.4	−69 28 41.6	±2.1	1.84±0.10	0.13±0.12	18.43	0.06	−1.5	13.0	—
NGC 1938	05 21 25.00	—	−69 56 21.5	—	2.04±0.09	0.34±0.07	18.48	0.23	−0.3	0.15	—
NGC 1939	05 21 26.37	±0.3	−69 56 58.4	±1.3	2.21±0.07	0.44±0.03	18.42	0.06	−1.5	13.3	—
NGC 1943	05 22 29.36	±0.4	−70 09 18.5	±0.8	2.04±0.04	0.08±0.07	18.46	0.14	−0.3	0.20	0.15
NGC 1953	05 25 27.95	±0.2	−68 50 16.1	±0.1	1.75±0.06	0.41±0.07	18.41	0.11	−0.4	0.50	0.35
NGC 1966	05 26 45.53	—	−68 49 50.9	—	1.59±0.04	0.52±0.21	18.40	0.06	−0.2	0.005	0.003
NGC 1978	05 28 44.71	±1.2	−66 14 10.9	±1.1	1.76±0.03	0.40±0.04	18.53	0.07	−0.5	2.50	—
NGC 1983	05 27 44.95	±0.8	−68 59 06.5	±0.3	1.60±0.05	0.49±0.05	18.56	0.03	0.0	0.014	—
NGC 1987	05 27 17.03	±0.1	−70 44 11.4	±0.2	1.94±0.06	0.46±0.04	18.43	0.07	−0.7	1.35	1.00
NGC 2002	05 30 20.82	±0.4	−66 53 01.1	±0.3	1.57±0.04	0.47±0.07	18.52	0.07	−0.2	0.02	—
NGC 2005	05 30 10.13	±0.1	−69 45 10.6	±0.2	1.88±0.04	0.56±0.04	18.44	0.09	−1.6	13.1	—
NGC 2010	05 30 33.93	±0.8	−70 49 07.8	±1.3	2.23±0.04	0.45±0.04	18.54	0.09	−0.2	0.12	—
NGC 2031	05 33 40.27	±2.9	−70 59 12.6	±1.5	2.30±0.07	0.61±0.07	18.40	0.09	−0.4	0.30	0.15
NGC 2056	05 36 33.95	±0.2	−70 40 15.7	±0.2	2.16±0.07	0.62±0.08	18.38	0.08	−0.4	0.45	0.30
NGC 2107	05 43 12.39	±0.1	−70 38 24.4	±0.2	1.96±0.10	0.83±0.11	18.37	0.16	−0.3	0.50	0.30
NGC 2108	05 43 56.54	±0.1	−69 10 52.9	±0.3	1.72±0.06	0.84±0.08	18.48	0.14	−0.3	1.25	1.00
NGC 2121	05 48 13.22	±1.4	−71 28 46.9	±0.8	1.76±0.05	0.96±0.04	18.48	0.09	−0.5	2.9	—
NGC 2154	05 57 38.22	±0.3	−67 15 41.7	±0.9	1.42±0.04	0.78±0.05	18.37	0.04	−0.5	2.00	1.80
NGC 2155	05 58 32.24	±0.3	−65 28 39.7	±0.6	1.73±0.07	0.88±0.05	18.39	0.05	−0.4	2.8	—
NGC 2156	05 57 49.88	±1.0	−68 27 42.5	±1.4	1.73±0.09	0.91±0.08	18.44	0.06	−0.2	0.17	0.10
NGC 2164	05 58 55.83	±0.4	−68 30 57.6	±0.3	1.60±0.04	0.78±0.04	18.43	0.07	−0.3	0.20	0.10
NGC 2173	05 57 58.40	±0.2	−72 58 43.2	±0.2	1.97±0.04	0.83±0.05	18.37	0.06	−0.4	2.05	1.70
NGC 2203	06 04 42.62	±0.7	−75 26 16.1	±0.5	1.93±0.03	0.88±0.03	18.38	0.07	−0.3	1.95	1.65
NGC 2209	06 08 36.19	±0.9	−73 50 09.9	±0.7	1.94±0.04	0.96±0.05	18.39	0.10	−0.4	1.45	1.15
NGC 2210	06 11 31.63	±0.2	−69 07 18.7	±0.2	1.44±0.05	1.36±0.05	18.36	0.04	−1.4	12.0	—
NGC 2213	06 10 42.13	±0.2	−71 31 45.9	±0.8	1.77±0.02	0.99±0.04	18.36	0.09	−0.4	1.85	1.60
NGC 2249	06 25 49.65	±0.3	−68 55 14.2	±0.2	1.55±0.06	1.09±0.05	18.34	0.06	−0.4	1.20	0.95
NGC 2257	06 30 12.42	±0.3	−64 19 36.6	±0.5	1.39±0.05	1.00±0.04	18.37	0.04	−1.4	11.8	—
OGLEclLMC390	05 21 18.91	—	−69 28 33.8	—	1.99±0.21	0.60±0.29	18.44	0.10	−0.5	1.55	1.30
Reticulum	04 36 10.99	±0.3	−58 51 45.5	±0.5	1.95±0.05	−0.27±0.02	18.40	0.00	−1.2	11.5	—
SL 075	06 13 27.26	±0.9	−70 41 45.0	±0.4	1.68±0.04	1.07±0.04	18.49	0.06	−0.4	1.95	1.70

Table B.3. Typical errors on distance modulus, reddening, age, and metallicity.

ID	Δ(m−M)$_0$ [mag]	ΔE(B−V) [mag]	Δage [Myr]	Δ[M/H] [dex]
NGC 2005	0.10	0.010	500	0.10
NGC 1939	0.15	0.015	1000	0.15
Kron 3	0.10	0.010	200	0.10
Kron 1	0.10	0.020	350	0.15
NGC 1846	0.10	0.010	75	0.10
Hodge 7	0.15	0.020	150	0.15
NGC 1866	0.10	0.010	30	0.10
BSDL 1650	0.20	0.035	100	0.20

Notes. The quantities listed in this table are indicative of the precision of values inferred from isochrone fitting. The horizontal lines separate the couples of clusters with similar ages and different photometric qualities. See the text for details.

Table B.4. Description of the data set of the 13 GCs with HST proper-motion determinations.

ID	CAMERA	FILTER	DATE	N×EXPTIME	PROGRAM	PI
BS 90, NGC 346	ACS/WFC	F555W	Jul 13-18 2004	4×3s+380s+4×456s+4×483s	10248	A. Nota
	ACS/WFC	F658N	Jul 15 2004	3×514s	10248	A. Nota
	ACS/WFC	F814W	Jul 13-18 2004	4×2s+380s+4×450s+4×484s	10248	A. Nota
	ACS/WFC	F555W	Jul 15-22 2015	4×3s+11×450s	13680	E. Sabbi
	ACS/WFC	F814W	Jul 15-20 2015	4×2s+10×450s	13680	E. Sabbi
KRON 34	UVIS/WFC3	F336W	Jan 13 2017	3×839s	14710	A. P. Milone
	UVIS/WFC3	F656N	Jan 13 2017	2×720s	14710	A. P. Milone
	UVIS/WFC3	F814W	Jan 13 2017	90s+680s	14710	A. P. Milone
	ACS/WFC	F555W	Aug 12 2003	165s	9891	G. Gilmore
	ACS/WFC	F814W	Aug 12 2003	130s	9891	G. Gilmore
LINDSAY 1	ACS/WFC	F555W	Jul 11 2003	480s	9891	G. Gilmore
	ACS/WFC	F814W	Jul 11 2003	290s	9891	G. Gilmore
	ACS/WFC	F555W	Aug 21 2005	2×20s+4×496s	10396	J. Gallagher
	ACS/WFC	F814W	Aug 21 2005	2×10s+4×474s	10396	J. Gallagher
	UVIS/WFC3	F275W	Jun 12 2019	1500s+1501s+2×1523s+2×1525s	15630	N. Bastian
	UVIS/WFC3	F275W	Jun 24-25 2020	1500s+2×1512s+4×1523s+2×1524s+2×1525s+1530s	15630	N. Bastian
	UVIS/WFC3	F336W	Jun 19 2019	500s+2×1200s	14069	N. Bastian
	UVIS/WFC3	F343N	Jun 19 2019	500s+800s+1650s+1850s	14069	N. Bastian
	UVIS/WFC3	F438W	Jun 19 2019	120s+2×460s	14069	N. Bastian
NGC 294	UVIS/WFC3	F336W	Feb 17 2017	3×839s	14710	A. P. Milone
	UVIS/WFC3	F656N	Feb 17 2017	2×680s	14710	A. P. Milone
	UVIS/WFC3	F814W	Feb 17 2017	90s+666s	14710	A. P. Milone
	ACS/WFC	F555W	Oct 24 2003	165s	9891	G. Gilmore
	ACS/WFC	F814W	Oct 24 2003	130s	9891	G. Gilmore
NGC 339	UVIS/WFC3	F336W	Aug 8 2016	700s+1160s+1200s	14069	N. Bastian
	UVIS/WFC3	F343N	Aug 8 2016	520s+800s+1250s+1650s	14069	N. Bastian
	UVIS/WFC3	F438W	Aug 8 2016	120s+180s+560s+660s	14069	N. Bastian
	ACS/WFC	F555W	Nov 28 2005	2×10s+4×496s	10396	J. Gallagher
	ACS/WFC	F814W	Nov 28 2005	2×10s+4×474s	10396	J. Gallagher
NGC 416	UVIS/WFC3	F275W	Jul 31, Aug 16 2019	3×1500s+1512s+2×1515s +1523s+1530s+2×1533s+2×1534	15630	N. Bastian
	UVIS/WFC3	F336W	Jun 16 2016	700s+1160s+1200s	14069	N. Bastian
	UVIS/WFC3	F343N	Jun 16 2016	500s+800s+1650s+1655s	14069	N. Bastian
	UVIS/WFC3	F438W	Jun 16 2016	75s+150s+440s+460s	14069	N. Bastian
	ACS/WFC	F555W	Mar 03 2006	2×10s+4×496s	10396	J. Gallagher
	ACS/WFC	F814W	Nov 22 2005	2×10s+4×474s	10396	J. Gallagher
	ACS/WFC	F814W	Mar 03 2006	2×10s+4×474s	10396	J. Gallagher
NGC 419	UVIS/WFC3	F336W	Aug 25 2011	400s+690s+2×700s+740s	12257	L. Girardi
	UVIS/WFC3	F343N	Aug 03 2016	450s+2×1250s+1625s	14069	N. Bastian
	UVIS/WFC3	F438W	Aug 03 2016	70s+150s+350s+550s	14069	N. Bastian
	ACS/WFC	F555W	Jul 08 2006	2×20s+4×496s	10396	J. Gallagher
	ACS/WFC	F814W	Jan 01 2006	2×10s+4×474s	10396	J. Gallagher
	ACS/WFC	F814W	Jul 07 2006	2×10s+4×474s	10396	J. Gallagher

Notes. For completeness, we include information on F275W images, although they are not used for deriving proper motions.

Table B.4. continued.

ID	CAMERA	FILTER	DATE	N×EXPTIME	PROGRAM	PI
NGC 1755	UVIS/WFC3	F336W	Oct 05 2015	2×711s	14204	A. P. Milone
	UVIS/WFC3	F336W	Dec 28 2015	2×711s	14204	A. P. Milone
	UVIS/WFC3	F336W	Mar 26 2016	2×711s	14204	A. P. Milone
	UVIS/WFC3	F336W	Jun 10 2016	2×711s	14204	A. P. Milone
	UVIS/WFC3	F814W	Oct 05 2015	90s+678s	14204	A. P. Milone
	UVIS/WFC3	F814W	Dec 28 2015	90s+678s	14204	A. P. Milone
	UVIS/WFC3	F814W	Mar 26 2016	90s+678s	14204	A. P. Milone
	UVIS/WFC3	F814W	Jun 10 2016	90s+678s	14204	A. P. Milone
	ACS/WFC	F555W	Aug 08 2003	50s	9891	G. Gilmore
	ACS/WFC	F814W	Aug 08 2003	40s	9891	G. Gilmore
NGC 1783	UVIS/WFC3	F275W	Sep 16 2019	2×1500s+4×1512s	15630	N. Bastian
	UVIS/WFC3	F336W	Oct 12 2011	2×1190s+1200s	12257	L. Girardi
	UVIS/WFC3	F343N	Sep 14 2016	450s+845s+1650s	14069	N. Bastian
	ACS/WFC	F814W	Oct 07 2003	170s	9891	G. Gilmore
	ACS/WFC	F555W	Jan 14 2006	40s+2×340s	10595	P. Goudfrooij
	ACS/WFC	F555W	Oct 07 2003	250s	9891	G. Gilmore
	ACS/WFC	F814W	Jan 14 2006	8s+2×340s	10595	P. Goudfrooij
	ACS/WFC	F435W	Jan 14 2006	90s+2×340s	10595	P. Goudfrooij
NGC 1801	UVIS/WFC3	F336W	Feb 26 2017	2×834s+835s	14710	A. P. Milone
	UVIS/WFC3	F656N	Feb 26 2017	2×720s	14710	A. P. Milone
	UVIS/WFC3	F814W	Feb 26 2017	90s+666s	14710	A. P. Milone
	ACS/WFC	F555W	Oct 08 2003	115s	9891	G. Gilmore
	ACS/WFC	F814W	Oct 08 2003	90s	9891	G. Gilmore
NGC 1953	UVIS/WFC3	F336W	Jul 18-19 2017	2×834s+835s	14710	A. P. Milone
	UVIS/WFC3	F656N	Jul 18 2017	2×720s	14710	A. P. Milone
	UVIS/WFC3	F814W	Jul 18 2017	90s+666s	14710	A. P. Milone
	ACS/WFC	F555W	Oct 07 2003	115s	9891	G. Gilmore
	ACS/WFC	F814W	Oct 07 2003	90s	9891	G. Gilmore
NGC 1978	UVIS/WFC3	F275W	Sep 17 2019	1492s+2×1493s+1495s+2×1498s +2×1499s+2×1500s+1501s+1502s	15630	N. Bastian
	UVIS/WFC3	F336W	2011 Aug 15 2011	380s+460s	12257	L. Girardi
	UVIS/WFC3	F336W	2016 Sep 25 2016	660s+740s	14069	N. Bastian
	UVIS/WFC3	F343N	2016 Sep 25 2016	425s+450s+500s+2×800s+1000s	14069	N. Bastian
	UVIS/WFC3	F438W	2016 Sep 25 2016	75s+120s+420s+460s+650s+750s	14069	N. Bastian
	UVIS/WFC3	F814W	Sep 14 2019	3×200s+348s+2×349s+688s	15630	N. Bastian
	ACS/WFC	F555W	Oct 07 2003	300s	9891	G. Gilmore
	ACS/WFC	F555W	Aug 15 2011	60s+300s+680s	12257	L. Girardi
	ACS/WFC	F814W	Oct 07 2003	200s	9891	G. Gilmore

Table B.5. Proper motions, relative to the main cluster in the fields of view, of field stellar populations represented with red, blue, and aqua colors in Figs. 21 and 22.

ID	Population	N	$\delta\mu_\alpha \cos\delta$ [mas yr^{-1}]	$\delta\mu_\delta$ [mas yr^{-1}]	ϵ	θ [deg]
KRON 34	Red	539	0.001±0.004	0.003±0.004	0.23±0.05	43±9
	Blue	193	0.031±0.006	−0.013±0.004	0.34±0.06	28±5
NGC 294	Red	657	0.041±0.004	−0.026±0.003	0.19±0.06	37±6
	Blue	256	0.045±0.004	−0.024±0.004	0.42±0.07	28±6
NGC 339	Red	54	0.014±0.014	0.013±0.012	0.10±0.08	33±11
	Blue	192	0.110±0.011	−0.059±0.009	0.62±0.03	38±3
NGC 416	Red	330	0.017±0.005	0.047±0.004	0.08±0.07	19±13
	Blue	688	0.109±0.006	0.017±0.004	0.30±0.05	26±6
NGC 419	Red	211	−0.070±0.008	0.050±0.008	0.31±0.07	33±6
	Blue	267	−0.077±0.009	0.054±0.006	0.42±0.07	29±5
NGC 1755	Red	296	0.077±0.006	0.169±0.007	0.02±0.08	86±16
	Blue	183	−0.019±0.005	0.139±0.005	0.17±0.07	314±14
NGC 1801	Red	321	0.058±0.007	−0.036±0.007	0.05±0.06	12±12
	Blue	209	0.001±0.005	0.009±0.005	0.20±0.13	48±16
	Aqua	44	0.023±0.012	0.003±0.017	0.09±0.12	46±18
NGC 1953	Red	441	0.095±0.007	0.039±0.006	0.00±0.05	360±13
	Blue	186	−0.029±0.006	−0.007±0.006	0.28±0.06	317±16
	Aqua	53	−0.092±0.009	−0.022±0.008	0.17±0.11	323±17

Notes. For each population we provide the ID of the reference cluster, the number of stars, N, the median proper motions ($\delta\mu_\alpha \cos\delta$ and $\delta\mu_\delta$, the ellipticity, ϵ, and the position angle, θ, of the best-fitting ellipse.

Table B.6. Proper motions relative to NGC 346 and proper-motion dispersions for the clusters NGC 346 and BS 90 and for the selected populations of pre-MS, MS, and RGB field stars.

ID	$\delta\mu_\alpha \cos\delta$ [mas yr^{-1}]	$\delta\mu_\delta$ [mas yr^{-1}]	$\sigma\mu_\alpha \cos\delta$ [mas yr^{-1}]	$\sigma\mu_\delta$ [mas yr^{-1}]	N
NGC 346	0.000±0.001	0.000±0.001	0.028	0.025	945
BS 90	−0.016±0.001	0.153±0.001	0.036	0.036	2220
pre-MS I	−0.032±0.005	0.019±0.004	0.083	0.075	345
pre-MS II	0.004±0.004	0.007±0.004	0.045	0.044	162
MS I	−0.024±0.002	0.005±0.002	0.059	0.062	2136
MS II	0.188±0.003	−0.034±0.004	0.079	0.088	582
RGB	−0.031±0.003	0.024±0.008	0.084	0.089	713